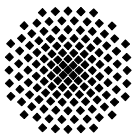

Universität Stuttgart

Diplomarbeit am ifp

Xiao Hu

Methods for quality control of large Cartosat-1 stereo blocks

Supervisors:
Dr. -Ing. Pablo d'Angelo (DLR)
Dr. -Ing. Michael Cramer

Examiner:
apl. Prof. Dr. -Ing. Norbert Haala

ifp

Student's statement

Herby it is confirmed, that this thesis entitled

Methods for quality control of large Cartosat-1 stereo blocks

was prepared independently, and that no sources and resources were used other than those explicitly listed in this thesis.

Place, Date: _____

Signature of thesis author: _____

(Xiao Hu)

Abstract

In the field of satellite remote sensing, the geometric accuracy of satellite imagery is strongly influenced by the quality of the satellite orientation. For example, rational polynomial coefficients (RPCs) are provided by the Indian agency as a universal sensor model for each scene of the Cartosat-1 stereo pairs. However, these RPCs derived from orbit and altitude information have the accuracy far worse than the pixel size of 2.5m (normally in the order of a few hundred meters). Hence, a new estimation of orientation parameters is necessary. This process requires well-distributed ground control points (GCPs) with sub-pixel accuracy. After adding accurate GCPs, improved orientation parameters can be obtained. By using GCPs, some institutes and universities such as ISRO, ETH Zurich, Erdas and University Hanover have made some important achievements for improving the satellite orientation. However, in many application fields, such as continent wide reconstruction or crisis support applications, acquiring the required GCPs is a time consuming task or might even be impossible, if a fast response is required.

In this diploma thesis, a new method of block adjustment, which helps to correct the orientation parameters, will be introduced and evaluated. The data resource is a block of 428 Cartosat-1 stereo pairs (region in north Italy).

In this thesis, a special attention will be put on the adjustment, which bases on the primary reference material which is digital surface model (DSM). This approach can be completely automated and does not require manual GCP collection. Another focal point is the independent quality control for the adjustment. Accurate check points derived from aerial images are chosen to realize the accuracy analysis. Finally, the results in this thesis are also compared with results of other research institute such as ISRO and ETH Zurich.

Keywords

- satellite remote sensing
- Cartosat-1 satellite
- digital surface model (DSM)
- universal sensor models (rational polynomial coefficients)
- bundle block adjustment
- accuracy analysis

Kurzbeschreibung

Verfahren zur Qualitätskontrolle von großen Cartosat-1 Stereoblöcken

Im Bereich der Satelliten-Fernerkundung ist die geometrische Genauigkeit von Satellitenbildern stark von der Qualität des Satelliten Orientierung beeinflusst. Zum Beispiel, rational Polynomkoeffizienten (RPCs) sind von der indischen Agentur als universeller Sensor Modell für jede Szene des Cartosat-1 Stereo-Paare zur Verfügung gestellt. Allerdings haben diese RPCs aus der Umlaufbahn und Höheninformationen abgeleitet die Genauigkeit deutlich schlechter als die Pixelgröße von 2,5 m (in der Regel in der Größenordnung von wenigen hundert Metern). Daher ist eine neue Schätzung der Orientierung notwendigen Parameter. Dieser Prozess erfordert gut verteilte Passpunkte (GCPs) mit Subpixel-Genauigkeit. Nach Zugabe von accutate GCPs kann eine verbesserte Orientierung Parameter erhalten werden. Durch die Verwendung von GCPs, einige Institute, Unternehmen und Universitäten wie ISRO, ETH Zürich, Universität Hannover und Erdas haben einige wichtige Errungenschaften für die Verbesserung der Orientierung Satelliten gemacht. Doch in vielen Anwendungsbereichen, wie z. B. Kontinent breit Wiederaufbau oder Krise Unterstützung von Anwendungen, den Erwerb der erforderlichen GCPs ist eine zeitraubende Aufgabe oder vielleicht sogar unmöglich sein, wenn eine schnelle Reaktion erforderlich ist.

In dieser Diplomarbeit wird eine neue Methode der Blockausgleichung, die der Orientierung hilft Parameter korrekt, eingeführt und bewertet werden. Die Daten-Ressource ist ein Block von 428 Cartosat-1 Stereo-Paare (Region in Nord-Italien).

In dieser Arbeit wird ein besonderes Augenmerk auf die Einstellung, die auf dem Primär-Referenzmaterial, das digitale Oberflächenmodell (DSM) ist Basen gebracht werden. Dieser Ansatz kann vollständig automatisiert werden und erfordert keine manuelle GCP-Sammlung. Ein weiterer Schwerpunkt ist die unabhängige Qualitätskontrolle für die Ausgleichung. Genaue Kontrollpunkte aus Luftbildern abgeleitet werden ausgewählt, um die Genauigkeit Analyse zu realisieren. Schließlich werden die Ergebnisse dieser Arbeit auch mit Ergebnissen anderer Forschungsinstitut wie ISRO und ETH Zürich verglichen.

Schlüsselwörter

- Satelliten Fernerkundung
- Cartosat-1 satellit
- Digitale Oberflächenmodelle (DOM)
- universeller Sensor Modell (rational Polynomkoeffizienten)
- bündel Blockausgleichung
- Genauigkeit Analysis

Contents

1 Introduction

1.1 Motivation

The geometric accuracy of satellite imagery is strongly influenced by the quality of the satellite orientation. For example, the ground accuracy of the Cartosat-1 images orthorectified using orbit and ephemeris data is in the order of hundred meters. Hence, a new estimation of orientation parameters is necessary. This process requires well-distributed ground control points (GCPs) with sub-pixel accuracy. After adding accurate GCPs, improved orientation parameters can be obtained. By using GCPs, some institutes, companies and universities such as ISRO, ETH Zurich, Erdas and University Hanover have made some important achievements for improving the satellite orientation. However, in many application fields, such as continent wide reconstruction or crisis support applications, acquiring the required GCPs is a time consuming task or might even be impossible, if a fast response is required.

1.2 Task

In this diploma thesis, a new method of block adjustment, which helps to correct the orientation parameters, will be introduced and evaluated. The data resource is a block of 428 Cartosat-1 stereo pairs (region in north Italy).

A special attention will be put on the adjustment, which bases on the primary reference material: the existing digital surface model (DSM). Another focal point is the independent quality control for the adjustment.

1.3 Outline

First of all, chapter 1 gives the general introduction about this topic. Next, in chapter 2 Cartosat-1 satellite and work environment of this thesis is introduced. Then some typical algorithms of photogrammetry are explained in chapter 3. Chapter 4 provides various methods of adjustment against Cartosat-1 stereo imagery and especially a new block adjustment model without using high accurate GCPs. In chapter 5 some tests against this new model are handled and the results are evaluated. Finally, conclusions and prospects are given.

2 Cartosat-1 satellite and work environment

2.1 Cartosat-1 satellite

Cartosat-1 satellite was launched on May 05, 2005 by India (see Figure 2.1).

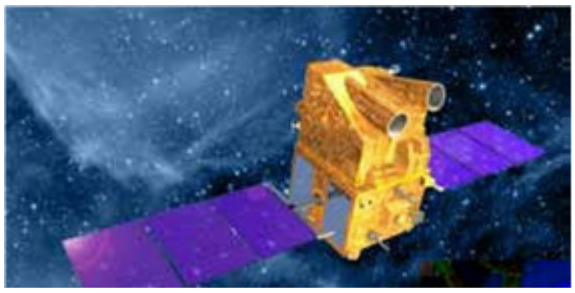

Figure 2.1: Cartosat-1 satellite (Figure from [Crespi 2006])

Cartosat-1 is a dedicated stereo platform which offers a ground resolution of approximately 2.5m. It is equipped with two panchromatic pushbroom cameras that are known as “Fore” and “Aft” camera. With an ideal stereo angle of 31° these two cameras are able to provide high resolution stereo image pairs, which are very suitable for DEM generation, 3D features extraction and orthophoto production (see Figure 2.2).

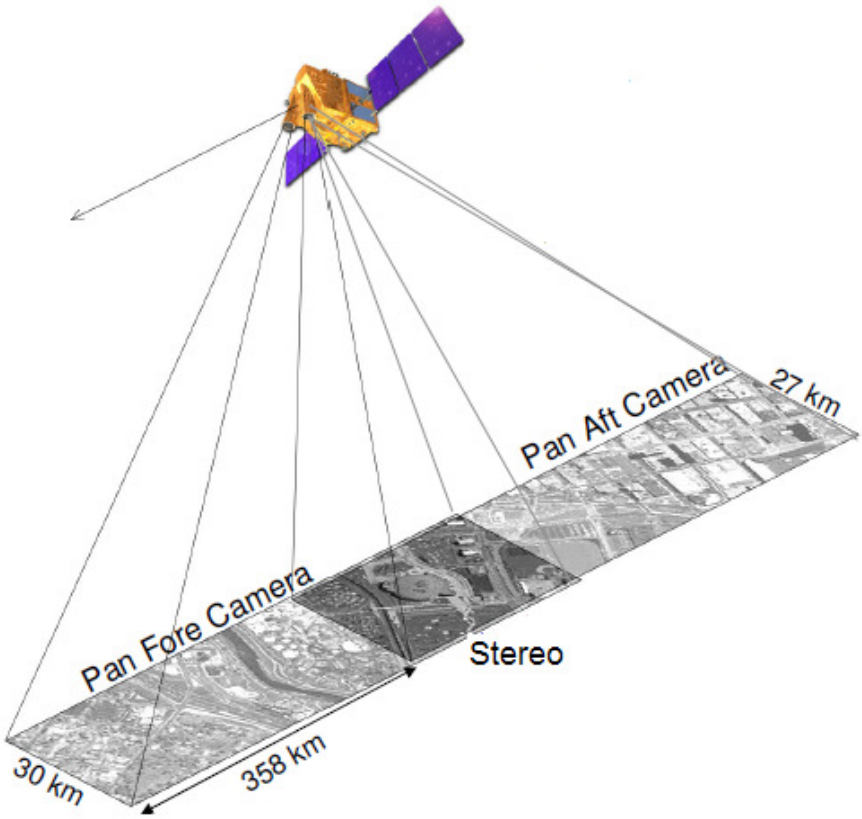

Figure 2.2: Stereo collection mode (Figure from [Puckorius 2008])

Table 2.1 describes some key characteristics of the Cartosat-1 sensors.

Sensor	PAN Fore	PAN Aft
Tilt Along Track	+26 deg	-5 deg
Spatial Resolution	2.5 m	2.5 m
Swath-width	30 km	27 km
Quantisation	10 bit	10 bit
Spectral coverage	500-850 nm	500-850 nm
Number of pixels pro line	12000	12000
Detector size	7×7 μm	7×7 μm
Camera FOV (Field Of View)	2.4 deg	2.4 deg
Focal length	1945 mm	1945 mm
Integration time	0.336 ms	0.336 ms

Table 2.1: Cartosat-1 sensor specifications (Table from [Lutes 2006] and [Puckorius 2008])

Cartosat-1 satellite flies along a near-polar, circular sun-synchronous orbit at an average altitude of 618 km. Some key orbit characteristics are presented in Table 2.2

Nominal Altitude	618 km
Orbits / day	14
Orbit Repetition	126 days
Revisit Time	5 days
Equatorial Crossing	10:30 AM local time
Orbit inclination	98.87°
Orbital Eccentricity	0.001
B/H	0.62

Table 2.2: Cartosat-1 orbit characteristics (Table from [Lutes 2006])

According to the orbit characteristics and sensor geometry given above, time interval between collection of the forward and aft scenes at the equator is about 53 seconds. Due to Earth rotation, however, the satellite ground track will have moved by 26 kilometers to the west in that time, which will lead to a different ground track for two cameras. In order to keep the same ground track, a yaw steering have to be installed onboard the satellite [Lutes, J. 2006].

Type	Examples	Typical resolution	Overlapping Images	Application area
Aerial cameras	UltraCam, DMC, 3K, HRSC,...	5-50cm	4-16	Local (city, province, country)
VHR satellites (1 camera)	IKONOS, WorldView 1 & 2, GeoEye	50cm-1m	2	Local (city)
Stereo satellites (more cameras)	Cartosat-1, ALOS/PRISM, SPOT-5	2.5-10m	2-3	Global (country & continent)

Table 2.3: Various camera platforms

Compared to other types of camera platforms (like aerial cameras, VHR satellites etc), Cartosat-1 platform has a relatively lower spatial resolution and is applied mainly for the global area such as country or continent (see Table 2.3).

Cartosat-1 imagery is available in a variety of data formats. Available products are in two formats: LGSOWG (Landsat Ground Station Operators Working Group) and Orthokit. The LGSOWG format provides the information of attitude and ephemeris, which makes it possible for people to develop or use their own sensor model; while the Orthokit product contains high resolution stereo image pairs and **Rational Polynomial Coefficients** (RPCs). The LGSOWG format is however not available for public use, and thus cannot be used in this thesis.

In this thesis, the Orthokit product will be chosen as the input data of block adjustment. Sample image pair with high quality is shown in Figure 2.3, with afterward channel (BANDA) shown on the left and forward channel (BANDF) on the right. Along with high quality images, the important item for the Orthokit product is RPCs files of image pairs. RPCs files describe the geometry relationship between object-space und image-space. How to correct for RPCs files is the main objective of this thesis and will be further introduced in chapter 4.

Figure 2.3: Typical Cartosat-1 urban scene (Figure from [Lutes 2006])

2.2 Work environment

In chapter 2.1 some basic knowledge about Cartosat-1 satellite and its products has been introduced; this section will present the work environment of this thesis. All in this diploma thesis used and developed programs are carried out in a Linux-system. This system contains a 64bit processor (Intel Core 2 Duo) with 1.86 GHz and 2 GB main work storage.

2.2.1 XDibias image processing system

XDibias is an image processing system developed by DLR (here X stands for X-Windows environment of Unix; while dibias is the abbreviation of German words "**D**igitales **I**nteraktives **B**ilda**u**swerte**s**ystem"). XDibias is used at DLR/MF for handling image processing work of large aerial images and satellite images. Until now, Xdibias has already had a history of over 30 years.

XDibias system consists of two main components: Image supervisor and image visualizer.

The image supervisor (see Figure 2.4) is a program control panel of XDibias. There are already more than 300 modules (see Figure 2.5) in the image supervisor. After loading the images, by using these modules, not only some simple operations such as zoom out (in) and rotate, but also complicated operations such as image matching, 3D feature extraction and orthorectification are able to be made. XDibias is continuously improved and the bundle block adjustment capabilities developed during this master thesis will be included in XDibias.

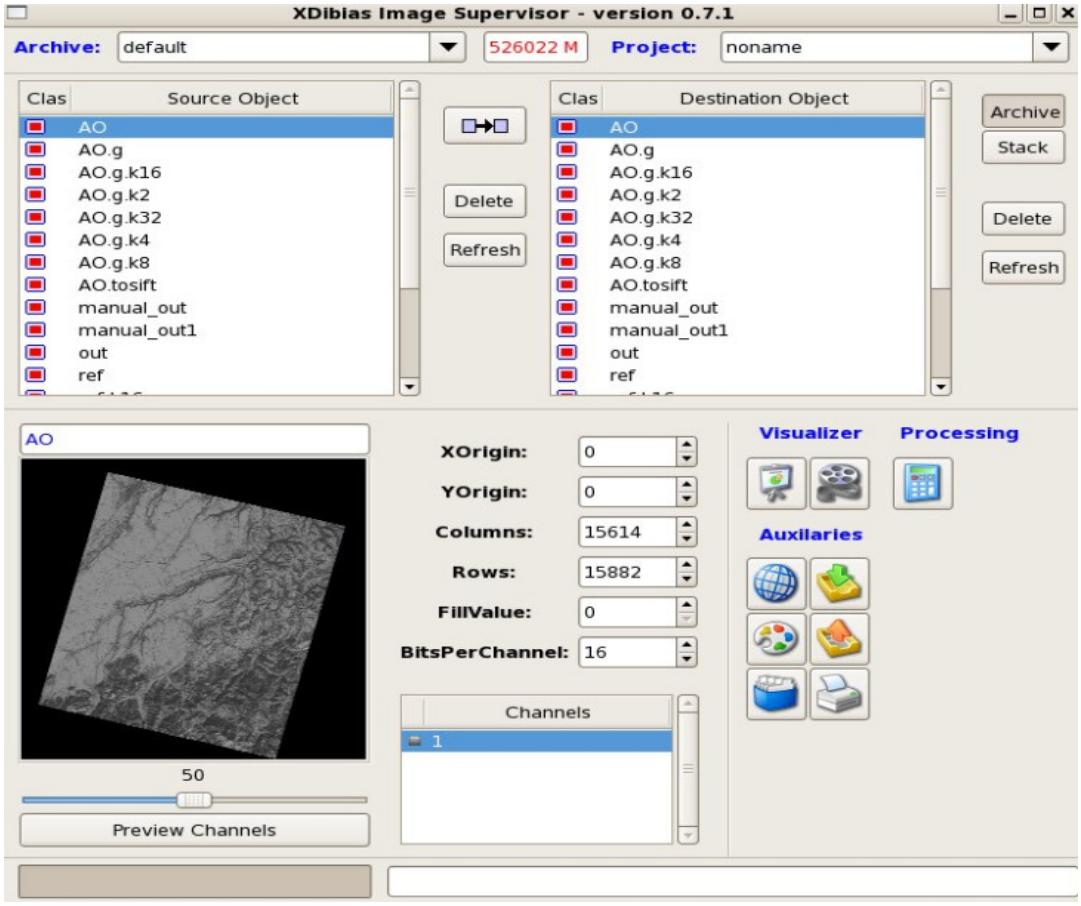

Figure 2.4: Image supervisor

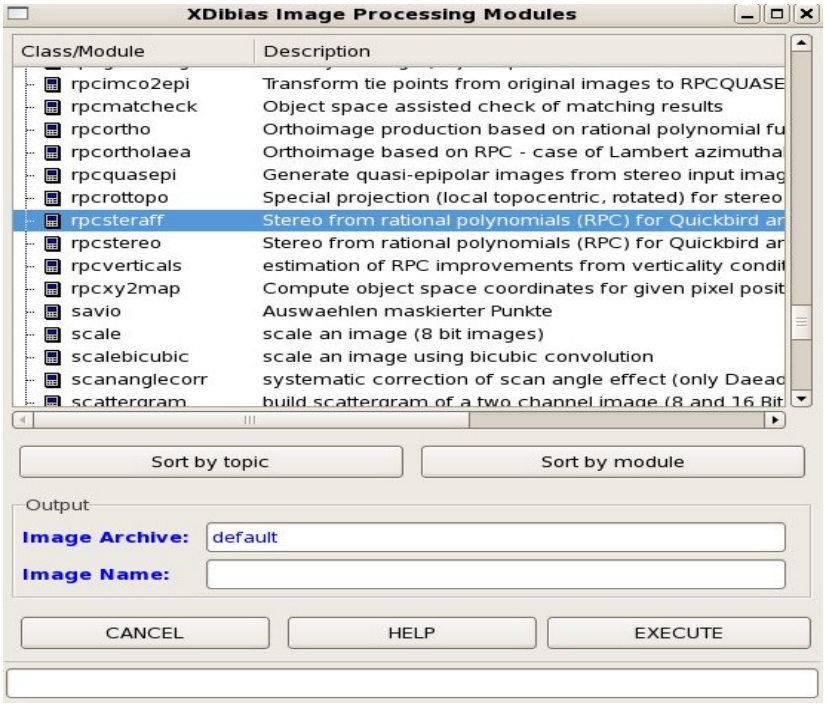

Figure 2.5: XDibias module

With the image visualizer IDibias, image pairs can be observed in side-by-side mode (see Figure 2.6). This mode makes it possible to measure homologous points from image pairs. What's more, if the images have been georeferenced, not only simple operations like distance and area measurement, but also complicated operations like vector processing and statistic evaluation are able to be processed.

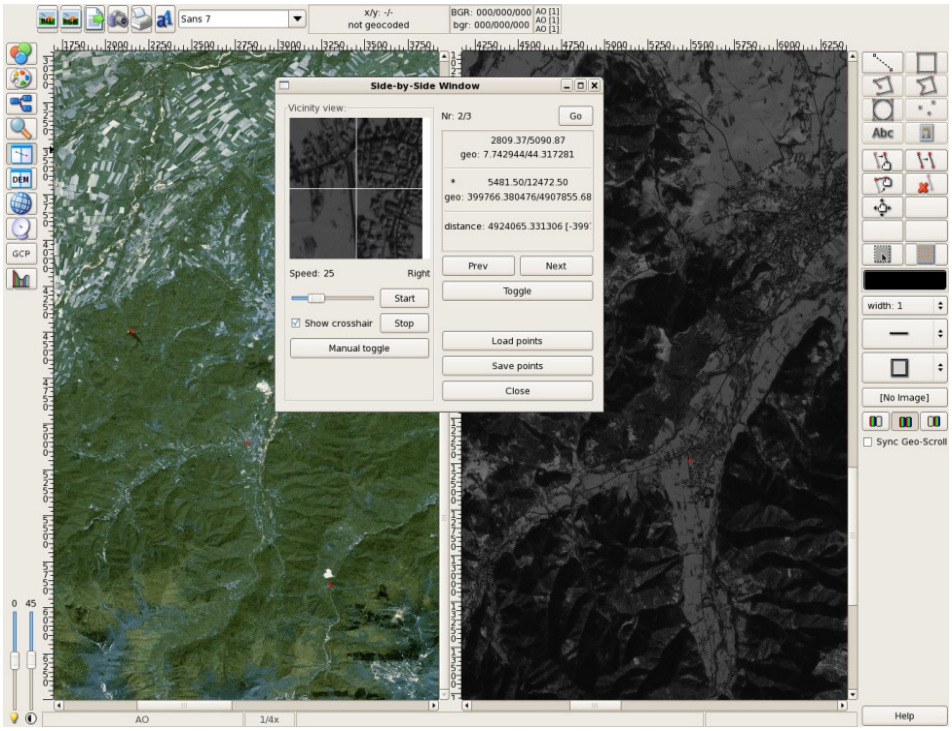

Figure 2.6: IDibias window

In this diploma thesis, the module rpcsteraff has been used in order to process the forward intersection from a stereo image pair.

2.2.2 Python and Kate text editor

The in this thesis developed programs are written in Python. Python is a high-level object-oriented programming language. This programming language already has many mature libraries to support its wide use. Three most important libraries are Numpy, Scipy and Matplotlib. Numpy adds support for numerical mathematics such as large, multi-dimensional arrays and matrices; Scipy allows complicated operations such as FFT, interpolation, signal and image processing; Matplotlib provides the possibility to plot like matlab.

Python is often used as a scripting language and can be processed both in Windows system and Unix system. For this diploma thesis, the Kate text editor is used for editing and running the python programs (see Figure 2.7). There are still a few programs that until now are not installed into XDibias as modes. The most important one is trafo, which is always used to handle the coordinate transformation (transform from geographic coordinates into UTM coordinates).

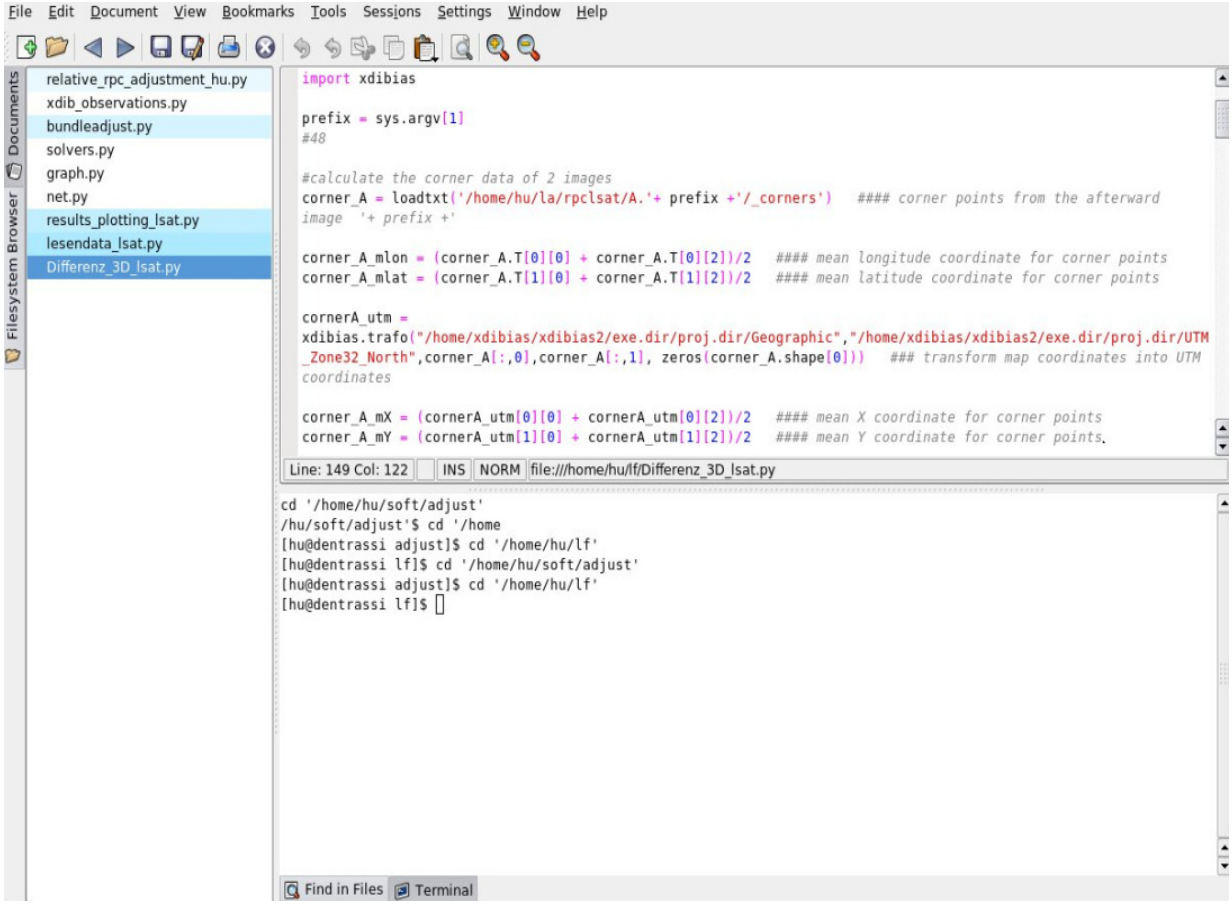

Figure 2.7: Kate text editor with python code and interactive shell

3 Algorithm

3.1 Ground control points (GCPs)

Ground control points (GCPs) are the points on the surface of the earth whose precise coordinates within an established system are known. GCPs identifiable on the images are always used for geo-referencing aerial and satellite images. [Srivastava 2007]

The GCP field survey is typically performed using DGPS receivers using FastStatic method or GPS RTK method. As a general rule, locations of GCPs are often selected where roads or paths crossed, while in some places only fence corners are reliable. In order to get an accurate result of geo-reference, GCPs should be well and evenly distributed over the images (see Figure 3.1: GCPs = triangles, CPs (check points) = circles). [Dabrowski 2008]

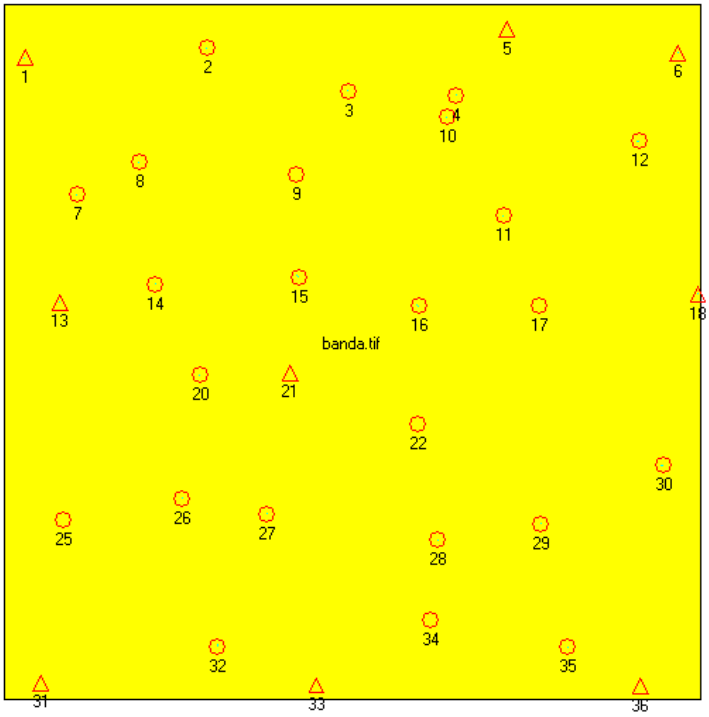

Figure 3.1: An example of GCP distribution (Figure from [Dabrowski 2008])

3.2 General camera model

3.2.1 Collinearity condition equations

The general camera model is given by the collinearity condition equations. As shown in equation (3.1) and equation (3.2), these equations are modified to transform 3D object coordinates to 2D image coordinates for an aerial image (see Figure 3.2). [Liang-Chien 2008]

$$x' = x_0' - c \cdot \frac{r_{11} \cdot (X - X_0) + r_{12} \cdot (Y - Y_0) + r_{13} \cdot (Z - Z_0)}{r_{31} \cdot (X - X_0) + r_{32} \cdot (Y - Y_0) + r_{33} \cdot (Z - Z_0)}$$
$$y' = y_0' - c \cdot \frac{r_{21} \cdot (X - X_0) + r_{22} \cdot (Y - Y_0) + r_{23} \cdot (Z - Z_0)}{r_{31} \cdot (X - X_0) + r_{32} \cdot (Y - Y_0) + r_{33} \cdot (Z - Z_0)} \quad (3.1)$$

R is the rotation matrix from object coordinate system to image coordinate system.

$$R = \begin{pmatrix} r_{11} & r_{12} & r_{13} \\ r_{21} & r_{22} & r_{23} \\ r_{31} & r_{32} & r_{33} \end{pmatrix} = R_3(\kappa) R_2(\varphi) R_1(\omega) \quad (3.2)$$

Here x', y' are the image coordinates, x_0', y_0', c are 3 interior orientation parameters, $X_0, Y_0, Z_0, \omega, \kappa, \varphi$ are 6 exterior orientation parameters, and X, Y, Z are the object coordinates.

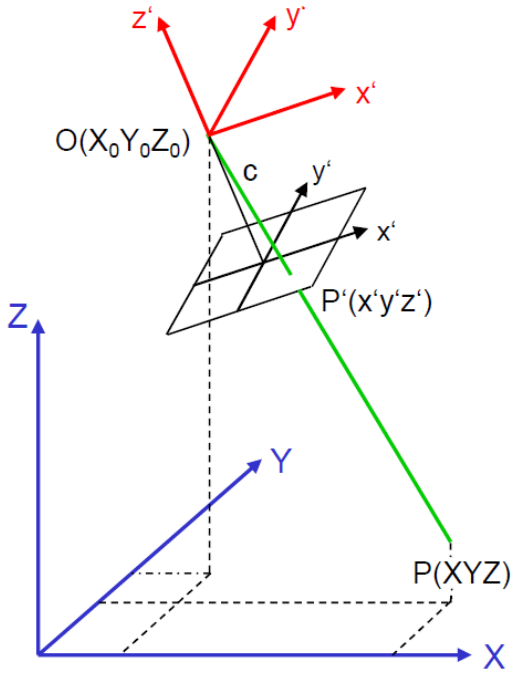

Figure 3.2: Standard geometry used in indirect georeferecing (Figure from [Cramer 2010])

Interior orientation parameters are usually already known, so that only 6 exterior orientation parameters as the unknowns exist. The exterior orientation parameters can be computed given at least 3 precise GCPs (both image coordinates and object coordinates are available). If more unknowns such as unknown 3D object coordinates have to be calculated, more GCPs are required for processing the bundle block adjustment.

3.2.2 Direct linear transformation (DLT)

With the purpose of calculating exterior orientation parameters, well-known **D**irect **L**inear **T**ransformation (DLT) method is often applied. This method is derived from collinearity condition equations. The transformation between image- and object space is shown in equations (3.3). (Equations from [Böhm 2007])

$$x = \frac{L_1 X + L_2 Y + L_3 Z + L_4}{L_9 X + L_{10} Y + L_{11} Z + 1}$$
$$y = \frac{L_5 X + L_6 Y + L_7 Z + L_8}{L_9 X + L_{10} Y + L_{11} Z + 1} \quad (3.3)$$

Where X, Y, Z are object coordinates, x, y are image coordinates, $L_i (i = 1, ...11)$ are unknown parameters. Clearly, there are 11 unknown parameters (6 exterior orientation parameters + 3 interior orientation parameters + 1 shear parameter + 1 scale difference parameter). Therefore, at least 6 GCPs, which are not on the same plane, are necessary for parameters calculation. [Böhm 2007] Again, if more unknowns such as unknown 3D object-coordinates have to be calculated, more GCPs are required for processing the bundle block adjustment.

It is important to point out that collinearity equations are non-linear. For parameter estimation and error evaluation, collinearity equations need approximated value for Taylor series expansion at first and then should be linearized. But for DLT, equations (3.3) already express a linear relationship and the linear observation equations for block adjustment can be easily obtained (see equation (3.4)). In addition, for DLT, no a priori information about interior orientation is necessary and affine distortion is already taken into consideration.

$$L_1 X + L_2 Y + L_3 Z + L_4 - x L_9 X - x L_{10} Y - x L_{11} Z = x$$
$$L_5 X + L_6 Y + L_7 Z + L_8 - y L_9 X - y L_{10} Y - y L_{11} Z = y \quad (3.4)$$

3.3 General satellite camera model

3.3.1 Introduction of linear array scanner

Because of the dynamic nature of satellite image collection, photogrammetric processing of satellite imagery is complex. An airborne frame camera usually captures the whole image instantaneously from a single, stable position and orientation. High-resolution pushbroom satellites like IKONOS and Cartosat-1 which use linear array scanners work in another way. Their CCD lines capture only a single image line at once (see Figure 3.3). Since the resulting imagery consists of both parallel and perspective projection, each line of a pushbroom satellite image has a different orientation from one to another, which leads to an expensive, time consuming and complicated model. ([Grodecki and Dial 2003], [Singh S.K. 2008]) In this chapter, some important methods help to establish such a complicated model will be introduced. Among them, the main attention is focused on rational polynomial camera model.

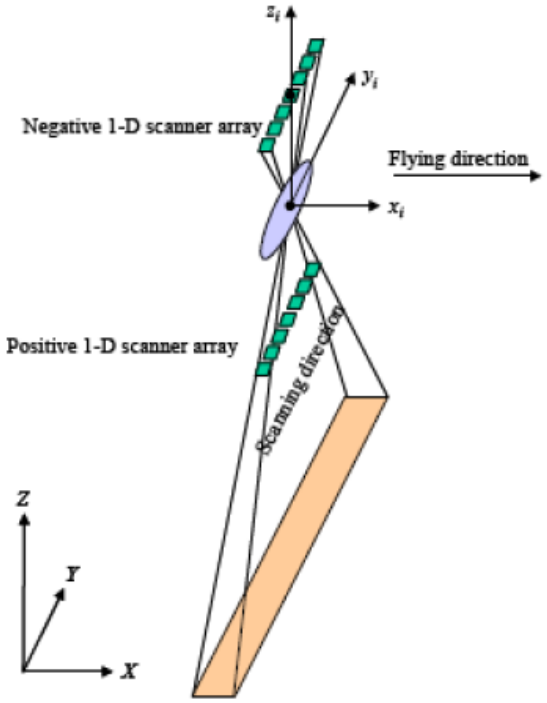

Figure 3.3: Linear array scanner (Figure from [Singh. G 2008])

3.3.2 Three main methods of establishing model

Especially for photogrammetric processing of pushbroom satellite imagery, three main methods are available. 1) rigorous approach, which represents not only physical model of satellite position and attitude but also internal sensor geometry. Atmosphere refraction effect and a possible final cartographic transformation will also be considered. In earlier satellites like SPOT and IRS 1C/1D such a rigorous model were used. However, this method is not suitable for Cartosat-1 images due to the fact that the necessary data is not included in Cartosat-1 imagery products. 2) “parametric” approach. It means that the model bases on formulae that contain different kinds of parameters. All required parameters are derived from GCPs. The DLT described in section 3.2.2 is a classic example of a parametric model. 3) the rational polynomial camera model, which is a so–called replacement model of rigorous model and is based on Rational Polynomial Coefficients (RPCs). This method is able to be applied to Cartosat-1 Orthokit imagery products so that among the three it is the most preferable one for Cartosat-1 imagery processing. This model will be introduced with more details in the following chapters.([Titarov 2007], [Ahmed 2007], [Giannone 2007])

3.3.3 Adjustment parameters

With the purpose of getting accurate result of georeferencing, a block adjustment along with GCPs is usually necessary. The traditional adjustment of exterior and interior orientation parameters, which has been present in chapter 3.2.1 and chapter 3.2.2, is preferable for aerial imagery. However, as described in chapter 3.3.1, the model for satellite imagery is more complicated.

The main adjustment parameters involve interior orientation and exterior orientation.

Interior orientation includes parameters for detector positions, image principal point, focal length and optical image distortion, so generally the calibration of aerial camera must be

processed at first. For high-resolution satellite like IKONOS, every pixel is already at a fixed, calibrated position on the focal plane. Moreover, the elements of interior orientation have been determined with well-controlled test imagery and already reach a very high level of accuracy. However, given interior orientation parameters of Cartosat-1 imagery is not accurate. Consequently, interior orientation parameters still have to be considered in the block adjustment process for Cartosat-1 imagery.

Exterior orientation contains position and attitude. The satellite ephemeris, which expresses the position of satellite with respect to a function of time, is determined by on-board GPS receivers. Star trackers and gyros give the data of the camera attitude as a function of time. As it is shown in equation (3.2), rotation matrix of collinearity condition equations contains 3 attitude angles, which consist of roll (rotation about the in-track direction), pitch (rotation about the cross-track direction) and yaw (rotation about the line-of-sight). For high-resolution satellite, the yaw error effect can be expressed by a function of swath width and results in a negligible ground displacement. Therefore, it is only necessary to estimate roll and pitch, effect of which is proportional to the slant range. Position errors are generally composed of in-track, cross-track and radial components. Since small horizontal displacements are equivalent to small angular rotations and indistinguishable, for narrow FOV (field-of-view) camera like IKONOS (ca. 1 degree) and Cartosat-1 (2.4 degrees), roll errors are highly correlated with cross-track errors, while pitch errors are correlated with in-track errors. As a result, for the reason of numerical stability, these correlated parameters should be combined into single parameters. Moreover, radial ephemeris errors are always not considered for Cartosat-1 because they only lead to negligible scale errors and can be corrected easily. For example, for Cartosat-1 satellite, which has a nominal altitude, if a 1m radial error occurs, it will lead to a 1.6ppm scale factor error and further result in a 47mm positioning error for Fore camera (with respect to 30km swath width) and a 42mm positioning error for Aft camera (with respect to 27km swath width). What's more, since position and attitude errors are large biases, drift errors as a function of time are also possible to occur. However, these errors are not large to influence the result of block adjustment if the image strips are not very long.

According to the analysis above, a large number of errors don't need to be considered and some of them are correlated with each other. Therefore, only a few errors are necessary to be modeled: A line offset parameter will be estimated to absorb effects of orbit, attitude and residual interior orientation errors in the line direction; while a sample offset parameter is also be chosen to absorb the same effects in the sample direction. For Cartosat-1 imagery, which has inaccurate interior orientation, only offset parameters are not enough. Generally, an affine transformation should be used for eliminate this negative effect and rest scale errors. [Grodecki and Dial 2003]

3.4 Rational polynomial camera model

3.4.1 Introduction

As demonstrated in chapter 3.3.2, instead of rigorous model, rational polynomial camera model basing on RPCs is a good replacement model. This concept of RPCs began with IKONOS, but was also being followed in other high-resolution satellite such as Cartosat-1. [Ahmed 2007]

The Rational polynomial camera model is widely applied, as it eases processing of imagery in standard software, and software vendors do not need to integrate complicated, satellite specific sensor models in their software.

Generally, the object coordinates are given in the form of (ϕ,λ,h), where ϕ is geodetic latitude, λ is geodetic longitude and h is height. In order to improve the numerical precision, 6 parameters including the latitude, longitude and height offsets and scale factors (LAT_OFF, LONG_OFF, HEIGHT_OFF, LAT_SCALE, LONG_SCALE, HEIGH_SCALE) will be given in order to normalize the object coordinates into a range from $\langle -1,+1\rangle$, as it is shown in following equations [Grodecki and Dial 2003]:

$$P=\frac{\phi-LAT\_OFF}{LAT\_SCALE} \tag{3.5}$$

$$L=\frac{\lambda-LONG\_OFF}{LONG\_SCALE} \tag{3.6}$$

$$H=\frac{h-HEIGHT\_OFF}{HEIGHT\_SCALE} \tag{3.7}$$

The RPC model then uses the form of a ratio of two cubic polynomials to describe the relationship between normalized object-space coordinates (ϕ,λ,h) and image coordinates $g(\phi,\lambda,h)$ and $h(\phi,\lambda,h)$ (relate to line and sample, respectively). One of them is used to express the object-to-line relationship, while the other is for object-to-sample relationship. 78 rational polynomial coefficients $(c_1\ldots c_{20},d_2\ldots d_{20},e_1\ldots e_{20},f_2\ldots f_{20})$ are determined to form these two polynomial functions, as follows:

$$g(\phi,\lambda,h)=\frac{Num_L(P,L,H)}{Den_L(P,L,H)}=\frac{c^Tu}{d^Tu} \tag{3.8}$$

where

$$\begin{aligned}Num_L(P,L,H)&=c_1+c_2L+c_3P+c_4H+c_5LP+c_6LH\\&+c_7PH+c_8L^2+c_9P^2+c_{10}H^2+c_{11}PLH+c_{12}L^3\\&+c_{13}LP^2+c_{14}LH^2+c_{15}L^2P+c_{16}P^3+c_{17}PH^2\\&+c_{18}L^2H+c_{19}P^2H+c_{20}H^3=c^Tu\end{aligned} \tag{3.9}$$

$$\begin{aligned}Den_L(P,L,H)&=1+d_2L+d_3P+d_4H+d_5LP+d_6LH\\&+d_7PH+d_8L^2+d_9P^2+d_{10}H^2+d_{11}PLH+d_{12}L^3\\&+d_{13}LP^2+d_{14}LH^2+d_{15}L^2P+d_{16}P^3+d_{17}PH^2\\&+d_{18}L^2H+d_{19}P^2H+d_{20}H^3=d^Tu\end{aligned} \tag{3.10}$$

with

$$\begin{aligned}u&=[1\ L\ P\ H\ LP\ LH\ PH\ L^2\ P^2\ H^2\ PLH\ L^3\ LP^2\\&\quad LH^2\ L^2P\ P^3\ PH^2\ L^2H\ P^2H\ H^3]^T\\c&=[c_1\ c_2\ldots c_{20}]^T\\d&=[1\ d_2\ldots d_{20}]^T\end{aligned}$$

and

$$h(\phi,\lambda,h)=\frac{Num_S(P,L,H)}{Den_S(P,L,H)}=\frac{e^T u}{f^T u} \tag{3.11}$$

where

$$\begin{aligned} Num_S(P,L,H) &= e_1+e_2L+e_3P+e_4H+e_5LP+e_6LH \\ &+e_7PH+e_8L^2+e_9P^2+e_{10}H^2+e_{11}PLH+e_{12}L^3 \\ &+e_{13}LP^2+e_{14}LH^2+e_{15}L^2P+e_{16}P^3+e_{17}PH^2 \\ &+e_{18}L^2H+e_{19}P^2H+e_{20}H^3=e^T u \end{aligned} \tag{3.12}$$

$$\begin{aligned} Den_S(P,L,H) &= 1+f_2L+f_3P+f_4H+f_5LP+f_6LH \\ &+f_7PH+f_8L^2+f_9P^2+f_{10}H^2+f_{11}PLH+f_{12}L^3 \\ &+f_{13}LP^2+f_{14}LH^2+f_{15}L^2P+f_{16}P^3+f_{17}PH^2 \\ &+f_{18}L^2H+f_{19}P^2H+f_{20}H^3=f^T u \end{aligned} \tag{3.13}$$

with

$$e=[e_1\ e_2\ldots e_{20}]^T$$

$$f=[1\,f_2\ldots f_{20}]^T$$

With the help of 4 additional parameters, such as line and sample offset and scale factors (LINE_OFF, SAMP_OFF, LINE_SCALE and SAMP_SCALE), normalized image-space coordinates $(g(\phi,\lambda,h),h(\phi,\lambda,h))$ in the range $\langle -1,+1\rangle$ will be finally transformed into de-normalized coordinates $(\overline{Line},\overline{Sample})$, as follows (Here $(\overline{Line},\overline{Sample})$ stand for image line number and image sample number, which are expressed in pixel):

$$\overline{Line}=g(\phi,\lambda,h)\cdot LINE\_SCALE+LINE\_OFF \tag{3.14}$$

$$\overline{Sample}=h(\phi,\lambda,h)\cdot SAMP\_SCALE+SAMP\_OFF \tag{3.15}$$

3.4.2 Determination of RPC coefficients

As demonstrated above, with the purpose of making an accurate transformation from image-space into object-space, 78 rational polynomial coefficients (RPCs) should be estimated. This is typically done by the satellite imagery provider using a least squared adjustment.

There are two main methods for the RPCs determination. If physical rigorous cameral model is available, a 3-D grid of object points, each of which is derived from its corresponding image points using physical rigorous camera model, can be generated. Then with an input of both object grid points (X,Y,Z) and image grid points $(Line,Sample)$, RPCs are fitted to the 3D object coordinates grid using a direct least-squares solution (See Figure 3.4). Tests have revealed that this method can reach very high fitting accuracy and can be chosen as a good replacement of physical camera model. On the other hand, without physical rigorous camera model, what also means a 3-D grid of object points is unavailable, a large number of

GCPs on the terrain surface are necessary to estimate RPCs. The accuracy of this method is highly dependent on the distribution of GCPs and has no links to the physical camera model. ([Grodecki and Dial 2003], [Hu and Tao 2001])

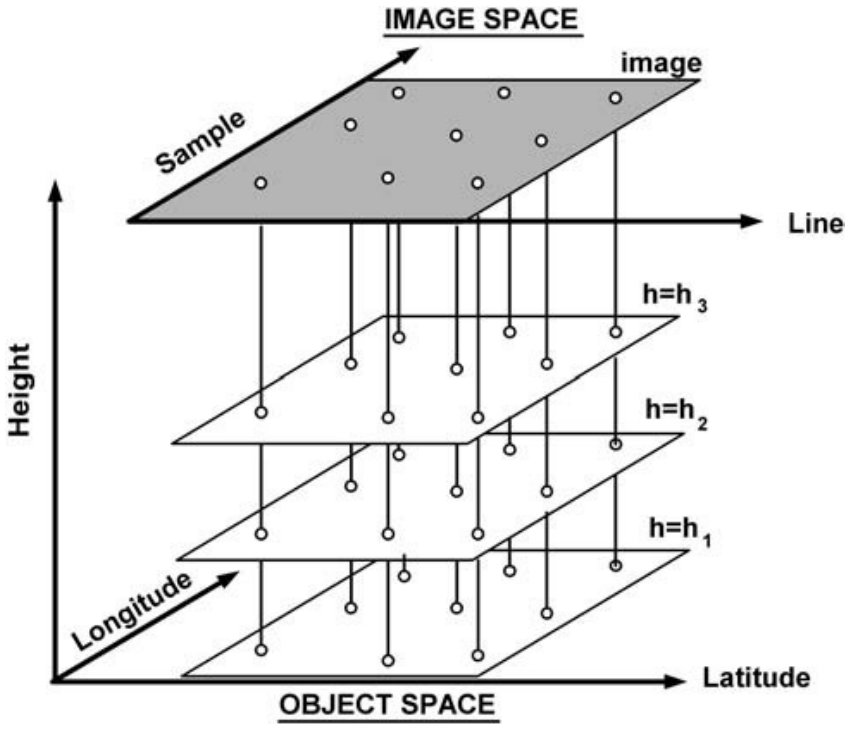

Figure 3.4: An example of RPCs determination (Figure from [Grodecki and Dial 2003])

3.5 Motivation of RPC block adjustment

In this diploma thesis, RPCs of Cartosat-1 satellite image is given by image vendors as _rpc files, an example form of which is shown in Figure 3.5. It is obvious to see that, _rpc file not only includes 6 offsets and scale factors for the latitude, longitude and height, 4 line and sample offsets and scale factors (first 10 rows), but also involves 80 rational polynomial coefficients (row 11 – row 90, 78 RPCs + 2 unit coefficients). For every single image, there is a corresponding _rpc file which helps establish an accurate relationship between image-space and object-space. What's more, combining _rpc files of stereo images or even more overlapping images enables to calculate the space coordinates of corresponding image points through forward intersection. As it is described in Figure 3.6, it is essential for constructing a stereo model (i.e. generation of DEM).

```
_rpc
 1 LINE_OFF: +6000.01
 2 SAMP_OFF: +6000.00
 3 LAT_OFF: +44.63094346
 4 LONG_OFF: +9.04276632
 5 HEIGHT_OFF: +799.999
 6 LINE_SCALE: +6100.00
 7 SAMP_SCALE: +6100.00
 8 LAT_SCALE: +0.16570845
 9 LONG_SCALE: +0.21631237
10 HEIGHT_SCALE: +899.999
11 LINE_NUM_COEFF_1: +2.861781428260770E-04
12 LINE_NUM_COEFF_2: -2.635435920749720E-01
13 LINE_NUM_COEFF_3: -1.154042758795580E+00
14 LINE_NUM_COEFF_4: -5.491582542745370E-03
15 LINE_NUM_COEFF_5: +2.516072120642093E-02
16 LINE_NUM_COEFF_6: -3.259846684795074E-03
17 LINE_NUM_COEFF_7: -1.413212393606212E-02
18 LINE_NUM_COEFF_8: +7.180816396822542E-04
19 LINE_NUM_COEFF_9: +6.861006878190164E-02
20 LINE_NUM_COEFF_10: -6.804986529729595E-05
21 LINE_NUM_COEFF_11: -6.624248309834832E-05
22 LINE_NUM_COEFF_12: -1.447161018482033E-04
23 LINE_NUM_COEFF_13: +2.300462392249794E-04
24 LINE_NUM_COEFF_14: -6.874553732343342E-06
25 LINE_NUM_COEFF_15: -5.185043713993946E-04
26 LINE_NUM_COEFF_16: -4.638907841678454E-04
27 LINE_NUM_COEFF_17: -3.127003112287289E-05
28 LINE_NUM_COEFF_18: -2.193969434322225E-05
29 LINE_NUM_COEFF_19: -2.896066794877234E-04
30 LINE_NUM_COEFF_20: -1.324768915907761E-07
31 LINE_DEN_COEFF_1: +1.000000000000000E+00
32 LINE_DEN_COEFF_2: -7.399348758631494E-03
33 LINE_DEN_COEFF_3: -5.952724593408121E-02
34 LINE_DEN_COEFF_4: +1.252908754302359E-02
```

Figure 3.5: Overview of _rpc file (only show a small part)

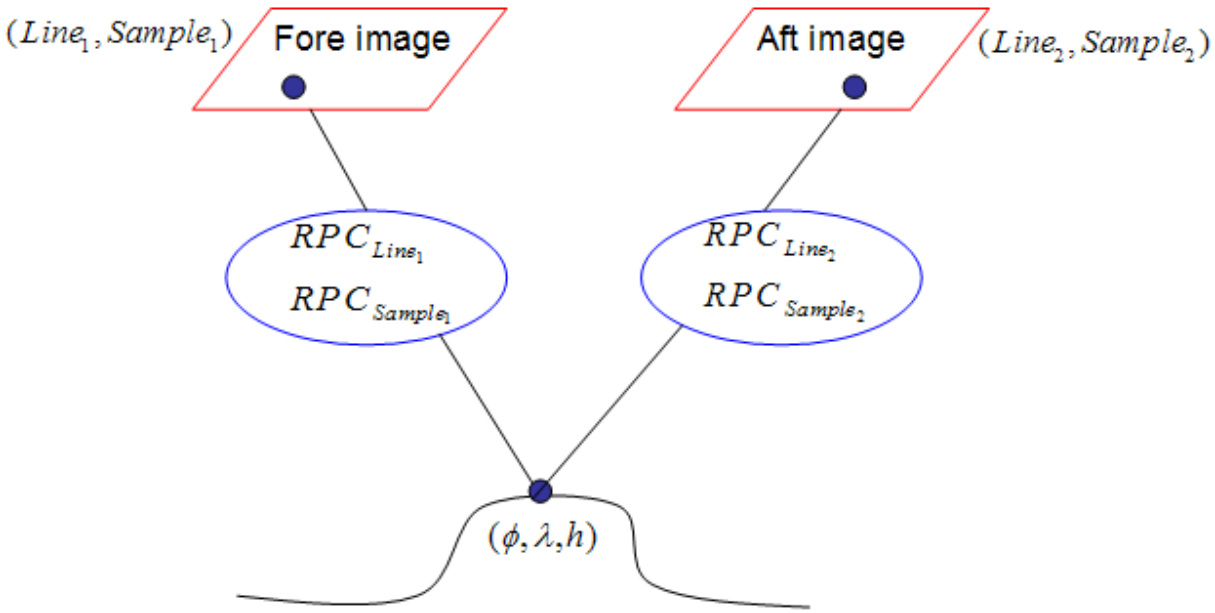

Figure 3.6: Stereo forward intersection basing on RPCs of a stereo pair

As mentioned in chapter 3.4.2, RPCs generated based on a physical camera model can achieve high accuracy. However, the RPCs provided by imagery vendors not always approximate the real image-object relationship very well. Generally, the provided Cartosat-1 RPCs is calculated by using satellite ephemeris, attitude coefficients and existed physical camera model, but without GCPs. If users want to get high accuracy products, a much higher price is required. As a result, the accuracy of Cartosat-1 RPCs is limited by the accuracy of the ephemeris and attitude data. These inaccurate RPCs may result in a very low absolute accuracy (even reaches hundreds of meters), which is much worse than the 2.5m spatial resolution of Cartosat-1 imagery. In order to reach the expected ground accuracy, a RPC block adjustment with additional ground control is necessary. ([Yilmaz 2008], [Liping 2008], [Lehner 2006])

As demonstrated before in chapter 3.3.3, instead of traditional adjustment method by using interior and exterior orientation parameters, the RPC block adjustment method by applying a line offset parameter, a sample offset parameter and a possible drift parameter with respect to the physical camera model, can get more stable numerical results. What's more, this method is suitable for any photogrammetric cameras with a narrow field of view and well known interior orientation (such as Cartosat-1 and IKONOS).

By using de-normalized RPCs (See equation (3.14) and (3.15)), there are two different kinds of models: a model defined in image space or a model defined in object space. For strips which are shorter than 20km, these two models give nearly the same results of block adjustment. But for longer strips, model defined in object space has low accuracy because of its non-linearity and poor links to image geometry of the physical camera model. [Grodecki and Dial 2003] As a result, for Cartosat-1 scenes, each of which has a size of 30km*30km, only the model defined in image space is available and it will be described further in chapter 4.4 in detail.

3.6 Other researches on Cartosat-1 images

The data processing about Cartosat-1 is handled by other Institutes such as ISRO (Indian Space Research Organisation)，Erdas, ETH Zurich, University Hanover and GeoEye, too. It should be noted that these research results always use a few high accurate GCPs in order to obtain better RPC corrections and 3D tie points coordinates. However, in this thesis, a new block adjustment model is introduced for the purpose of avoiding the use of high accurate GCPs. This new model will be discussed further in the next chapter.

4 RPC adjustment models

As introduced in chapter 3.3 and 3.4, a RPCs model is able to replace the rigorous physical camera model, if some improvements are made by ground control information (usually via GCPs). [Niemeier 2008] Therefore, a block adjustment for RPCs and 3D object coordinates is required. Available datasets are introduced in this chapter. Then different kinds of RPC adjustment models are given. Among them, the focus is put on the 1-step large block adjustment model.

4.1 Available datasets

Along with 428 Cartosat-1 stereo pairs, _rpc files that contain raw RPCs for each image as important Orthokit products are also provided (see Figure 3.5). For RPC correction, global and easily available low resolution datasets such as the OnEarth Landsat ETM+ Geocover mosaic and the SRTM digital surface model (DSM) are widely used (see Figure 4.1):

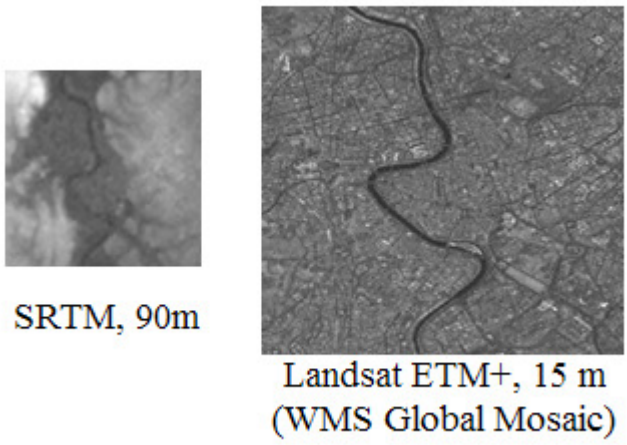

Figure 4.1: SRTM DSM and Landsat ETM+ geocover mosaic

These two main datasets have a much lower accuracy compared to Cartosat-1 images with a spatial resolution of 2.5m. The absolute horizontal error of Landsat ETM+ Geocover is about 50m, while the absolute horizontal error of SRTM is between 7.2m and 12.6m together with an absolute height error of 4.7m to 9.8m.

4.2 General RPC adjustment model (with GCPs)

4.2.1 Image matching

As described before, a general RPC adjustment model for a satellite stereo pair or multiple overlapping images requires a number of precise GCPs and tie points. High accurate GCPs of sub-pixel accuracy are often derived from DGPS measurements and high-resolution orthoimages. The GCPs are identified in the Cartosat-1 Aft images because of its better radiometric quality and then transferred to the fore images via local least squares matching (LSM). [Lehner 2007] For the purpose of generating dense high accurate tie points, a process of precise image matching is also demanded.

This hierarchical intensity based matching is used for matching a satellite stereo pair and the reference image.

The matching process uses a resolution pyramid to cope with large stereo image distortions stemming from carrier movement and terrain. Here, based on Förstner interest operator, a suitable pattern window will be chosen for one of stereo partners (chosen according to the best radiometric properties – in case of Cartosat-1 this is the Aft image). For the determination of search area in the other stereo partner, based on already available tie points derived from a coarser level of the image pyramid, a local affine transformation is made. Tie points with the accuracy of one pixel are looked for by sliding the pattern windows over the search area. Via the maximum of the normalized correlation coefficients these tie points are able to be located. Furthermore, these estimated tie points coordinates are refined to sub-pixel accuracy by using LSM. Finally, this step generates a rather sparse set of tie points which are very suitable for bundle block adjustment. ([Lehner 2006], [Lehner 2007], [Lehner 2008], [D'Angelo 2008])

4.2.2 RPC correction via affine transformation

Along with high accurate GCPs and tie points derived from image matching, RPC correction parameters can be estimated for a stereo pair. For IKONOS and QuickBird stereo pairs, the absolute positional accuracy of their images is already very high (IKONOS: below 10m) so that only a RPC correction via a bias adjustment is necessary. However, for the Cartosat-1 images, the absolute positional accuracy of which is only hundreds of meters, a relative RPC correction is not able to lead to nice stereo models. Thus, an absolute RPC correction via affine transformation is required. [Lehner 2007]

The output data derived from block adjustment via affine transformation are the 6 affine corrections to RPCs $(\Delta a_0, \Delta a_1, \Delta a_2, \Delta b_0, \Delta b_1, \Delta b_2)$ and $3i$ ($i =$ number of tie points) corrections to 3D coordinates of tie points $(\Delta\phi_i, \Delta\lambda_i, \Delta h_i)$. With corrected RPCs and known 2D image coordinates of GCPs and check points (CPs), a further forward intersection for the purpose of calculating corrected 3D coordinates of GCPs and CPs is made. Furthermore, not only the differences between measured (latitudes and longitudes are given by the reference image, heights are given by SRTM DSM) and corrected 3D coordinates of GCPs and CPs but also the rest residuals in image space are able to be calculated in order to estimate the accuracy of RPC block adjustment.

The module "rpcsteraff" in the image processing system XDibias realizes the process of forward intersection. The input data for a stereo pair are an imco file, 2 rpc.dat files, 2 affine RPC correction files and 2 corner files. Among them, imco file contains the image coordinates of the homologous GCPs and CPs in the following form: (row(1), column(1), row(2), column(2)); 2 rpc.dat files give 78 original RPCs; 2 affine RPC correction files contain 6 corrected affine transformation parameters for RPCs in the form of $(a_1, a_2, a_0; b_1, b_2, b_0)$; and 2 corner files include latitude and longitude information for 4 edges. The output data is an obko file, which contains in case of convergence of the iterative least squares adjustment the resulting object coordinates in the form: (point-number, longitude, latitude, height, number of iterations, number of rays). In addition, residuals in image space are directly calculated.

4.3 RPC adjustment model for a stereo pair (2 steps)

In this chapter a two-step RPC adjustment model for a stereo pair without high accurate GCPs is introduced, developed in [D'Angelo 2008].

4.3.1 Motivation

As demonstrated in chapter 4.2, with the help of well-distributed high accurate GCPs, a procedure of absolute RPC correction is handled against low accurate Cartosat-1 RPCs. However, such GCPs with subpixel accuracy are not always available. In fact, the collection of precise GCPs is very difficult or might even be impossible when lacking time and accessibility. Thus, in many application fields such as large scale reconstruction or crisis support applications, a new way without high accurate GCPs to correct RPCs of a stereo pair is required. ([Lehner 2004], [D'Angelo 2009])

Generally, Landsat ETM+ Geocover as a reference image is applied for collecting horizontal positions. The height data are acquired by interpolating the corresponding height from the SRTM DSM. However, the horizontal accuracy is limited by the lower precision of reference image.

The new method considers the obviously higher horizontal accuracy of the SRTM dataset. A RPC correction based on DSM alignment is applied, which leads to improved geolocation of both generated DEM and ortho images. ([D'Angelo 2008], [D'Angelo 2009], [D'Angelo 2010])

4.3.2 The working process

4.3.2.1 Stereo image matching

Similar to chapter 4.2.1, hierarchical intensity based matching is used for matching Cartosat-1 stereo pairs and reference Landsat ETM+ Geocover before RPC correction. It contains two main steps: hierarchical matching to derive high accurate tie points and dense, epipolar based stereo matching.

The matching procedure starts by matching the Cartosat-1 Aft and Fore images using hierarchical matching, as described in chapter 4.2.1. For the further RPC correction, high accurate tie points both in Aft and Fore images are found by giving strict thresholds on correlation coefficient (0.8) and bidirectional matching differences (0.1 pixel).

The second step bases on an epipolar pair with epipoles relating to the image columns. Dense stereo matching using the semi-global matching (SGM) algorithm is then performed on the epipolar images. ([D'Angelo 2008], [D'Angelo 2009], [D'Angelo 2010])

4.3.2.2 RPC correction (step 1) and GCP collection

After stereo matching, high quality tie points between the stereo pair have been found. Then they are transferred to the lower resolution Landsat ETM+ reference also by using LSM. It is important to point out that unlike stereo pair matching, the time difference between Landsat ETM+ and Cartosat-1 stereo images is more than 8 years (Landsat data has been acquired in 1999), which also means there are strong radiometric differences between them. Thus, only a small part of tie points can be matched among these three images. After this matching procedure, geographic positions of the stereo tie points and GCPs are already determined. Then, 3D GCPs for both Aft and Fore images are able to be collected by bilinear interpolation of the SRTM DSM (for the purpose of extracting the corresponding height data from SRTM).

Preliminary affine RPC corrections for the Aft and Fore images are estimated using these GCPs.

4.3.2.3 RPC correction (step 2)

After the preliminary alignment, forward intersection residuals are greatly reduced. In order to improve the horizontal and vertical accuracy further, a secondary RPC correction by DSM alignment is performed.

By forward intersection of the tie points, a 3D point cloud is calculated. This point cloud is aligned to SRTM DSM which has the higher horizontal accuracy. Under the assumption that a point P_i locates at the position (x_i, y_i, z_i) has the height z_i, which just equals to the reference DSM height $h_D(x_i, y_i)$ at the corresponding position (x_i, y_i):

$$h_D(x_i, y_i) = z_i \tag{4.1}$$

A 3D affine transformation matrix is used to align the initial stereo point cloud to the SRTM DSM:

$$p_{ti} = Ap_i \tag{4.2}$$

Where $p_i = (x_i, y_i, z_i, 1)$ is the original point, A is a 3×4 matrix, and $p_{ti} = (x_{ti}, y_{ti}, z_{ti})$ is the transformed point.

The affine transformation matrix A is estimated using an iterative least mean squares algorithm. Using equation (4.1) and (4.2), the observation equation is obtained as follows:

$$v_i = h_D(x_{ti}, y_{ti}) - z_i \tag{4.3}$$

The model is non-linear so that the solution has to be obtained iteratively. Points with a residual larger than 3 times the deviation are removed and a new transformation is estimated. This process is repeated until less than 0.3% outliers are detected and the squared sum of the outlier residuals accounts for less than 5% of the squared sum of all residuals. By this step local terrain changes and holes in reference DSM can be handled. A subset of the aligned point cloud is used as GCPs for the estimation of the final affine RPC correction parameters. ([D'Angelo 2008], [D'Angelo 2009], [D'Angelo 2010])

According to the demonstration all above, the whole working process of the 2-step RPC correction for a stereo pair is given by following flow chart:

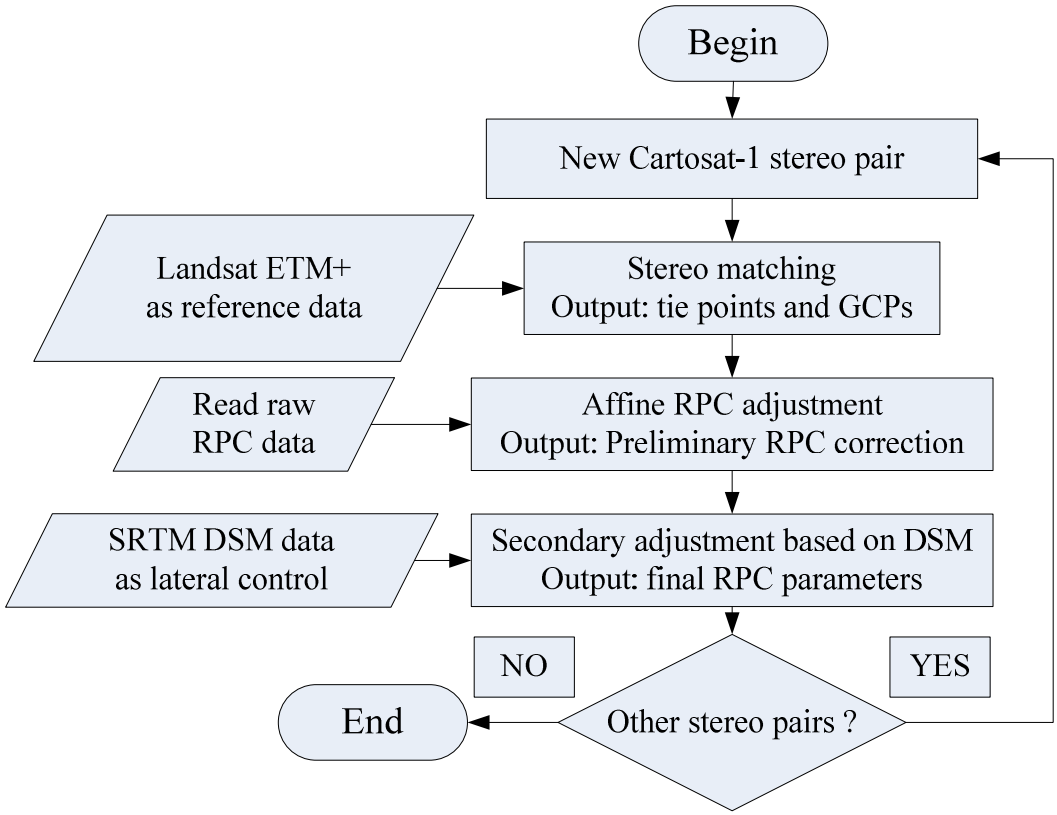

Figure 4.2: Working process of 2-step RPC correction

4.4 RPC adjustment model for more images (1 step)

In this chapter a new one-step RPC adjustment model for more overlapping images will be introduced.

4.4.1 Motivation

Although the 2-step RPC correction model can handle the situation without high accurate GCPs, there are still some disadvantages. First, for completely flat stereo scenes, the RPC correction is not very accurate. The reason is: A flat or homogenous area may cause an inaccurate transformation from image-space to object-space, which means possible shifts along horizontal directions (see Figure 4.3). Second, until now the process of RPC block adjustment is still for a stereo pair only.

Considering the drawbacks mentioned above, a new RPC adjustment model for more overlapping images has to be designed. Similar to 2-step RPC adjustment model, for the purpose of getting a fast response, high accurate GCPs are not available for the new adjustment model, either. A classical block adjustment [Grodecki and Dial 2003] thus can not be used in this context. For the new model, SRTM DSM of higher precision is selected as the only ground control. Further more, SRTM data are directly inserted into the observation equations as terms of observations. After one step RPC block adjustment process, accurate corrections to the tie points and RPCs for all overlapping images are successfully obtained. Details will be given by following chapters.

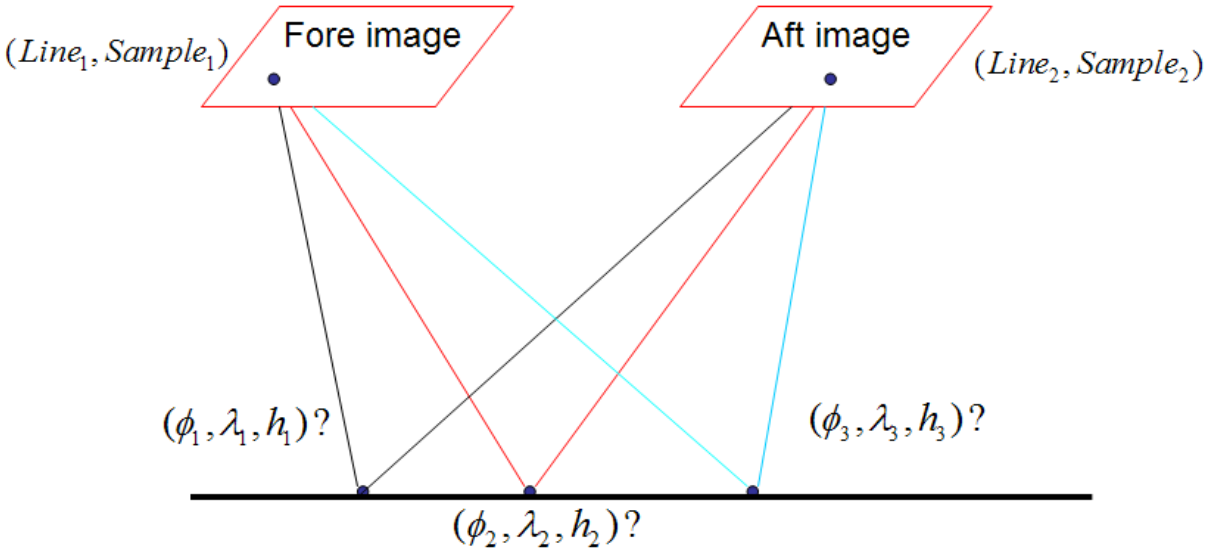

Figure 4.3: Horizontal shift caused by flat area (here $h_1 = h_2 = h_3$)

4.4.2 The working process

4.4.2.1 Image matching

Similar to the 2-step RPC adjustment model, a strict stereo image matching has to be processed at first, in order that accurate tie points are able to be generated. The difference is, image matching for the 1-step RPC adjustment model should be handled not only between single stereo pair but also among more overlapping stereo pairs. This is done by using SIFT image matching. As a result, different numbers of well-distributed tie points are generated for n stereo pairs (n can be 1, 2, 3,…) and stored in corresponding tie points files (*.str).

The files of tie points provide primary input data for 1-step RPC adjustment and have a form described in Figure 4.4. The first three columns give 3D object coordinates of each tie points in order of $(Longitude, Latitude, Height)$. It is also important to know how many images a single tie point stays in. The 4th column provides this number for each tie point. The columns left give the pixel coordinates of each tie point in all corresponding stereo images. The order is $(image\ number_1, row_1, column_1; image\ number_2, row_2, column_2 \cdots)$.

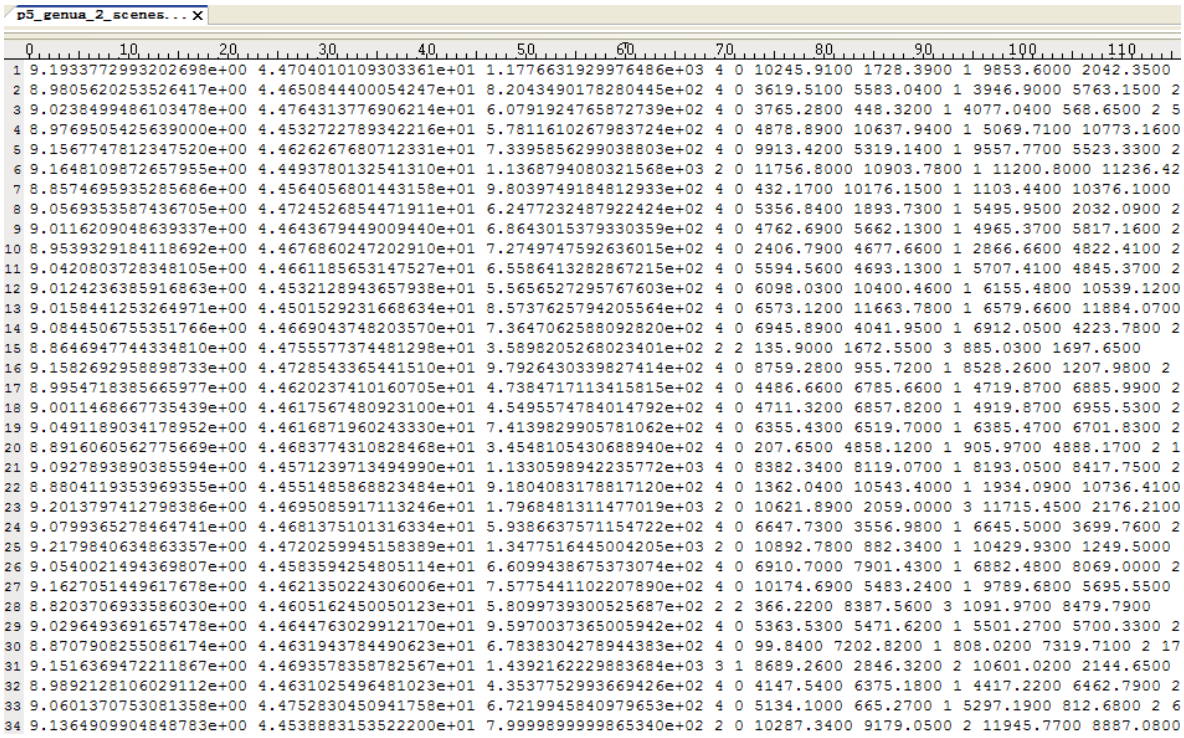

p5_genua_2_scenes. . .

```
 1 9.1933772993202698e+00 4.4704010109303361e+01 1.1776631929976486e+03 4 0 10245.9100 1728.3900 1 9853.6000 2042.3500
 2 8.9805620253526417e+00 4.4650844400054247e+01 8.2043490178280445e+02 4 0 3619.5100 5583.0400 1 3946.9000 5763.1500 2
 3 9.0238499486103478e+00 4.4764313776906214e+01 6.0791924765872739e+02 4 0 3765.2800 448.3200 1 4077.0400 568.6500 2 5
 4 8.9769505425639000e+00 4.4532722789342216e+01 5.7811610267983724e+02 4 0 4878.8900 10637.9400 1 5069.7100 10773.1600
 5 9.1567747812347520e+00 4.4626267680712331e+01 7.3395856299038803e+02 4 0 9913.4200 5319.1400 1 9557.7700 5523.3300 2
 6 9.1648109872657955e+00 4.4493780132541310e+01 1.1368794080321568e+03 2 0 11756.8000 10903.7800 1 11200.8000 11236.42
 7 8.8574695935285686e+00 4.4564056801443158e+01 9.8039749184812933e+02 4 0 432.1700 10176.1500 1 1103.4400 10376.1000
 8 9.0569353587436705e+00 4.4724526854471911e+01 6.2477232487922424e+02 4 0 5356.8400 1893.7300 1 5495.9500 2032.0900 2
 9 9.0116209048639337e+00 4.4643679449009440e+01 6.8643015379330359e+02 4 0 4762.6900 5662.1300 1 4965.3700 5817.1600 2
10 8.9539329184118692e+00 4.4676860247202910e+01 7.2749747592636015e+02 4 0 2406.7900 4677.6600 1 2866.6600 4822.4100 2
11 9.0420803728348105e+00 4.4661185653147527e+01 6.5586413282867215e+02 4 0 5594.5600 4693.1300 1 5707.4100 4845.3700 2
12 9.0124236385916863e+00 4.4532128943657938e+01 5.5656527295767603e+02 4 0 6098.0300 10400.4600 1 6155.4800 10539.1200
13 9.0158441253264971e+00 4.4501529231668634e+01 8.5737625794205564e+02 4 0 6573.1200 11663.7800 1 6579.6600 11884.0700
14 9.0844506755351766e+00 4.4669043748203570e+01 7.3647062588092820e+02 4 0 6945.8900 4041.9500 1 6912.0500 4223.7800 2
15 8.8646947744334810e+00 4.4755577374481298e+01 3.5898205268023401e+02 2 2 135.9000 1672.5500 3 885.0300 1697.6500
16 9.1582692958898733e+00 4.4728543365441510e+01 9.7926430339827414e+02 4 0 8759.2800 955.7200 1 8528.2600 1207.9800 2
17 8.9954718385665977e+00 4.4620237410160705e+01 4.7384717113415815e+02 4 0 4486.6600 6785.6600 1 4719.8700 6885.9900 2
18 9.0011468667735439e+00 4.4617567480923100e+01 4.5495574784014792e+02 4 0 4711.3200 6857.8200 1 4919.8700 6955.5300 2
19 9.0491189034178952e+00 4.4616871960243330e+01 7.4139829905781062e+02 4 0 6355.4300 6519.7000 1 6385.4700 6701.8300 2
20 8.8916060562775669e+00 4.4683774310828468e+01 3.4548105430688940e+02 4 0 207.6500 4858.1200 1 905.9700 4888.1700 2 1
21 9.0927893890385594e+00 4.4571239713494990e+01 1.1330598942235772e+03 4 0 8382.3400 8119.0700 1 8193.0500 8417.7500 2
22 8.8804119353969355e+00 4.4551485868823484e+01 9.1804083178817120e+02 4 0 1362.0400 10543.4000 1 1934.0900 10736.4100
23 9.2013797412798386e+00 4.4695085917113246e+01 1.7968481311477019e+03 2 0 10621.8900 2059.0000 3 11715.4500 2176.2100
24 9.0799365278464741e+00 4.4681375101316334e+01 5.9386637571154722e+02 4 0 6647.7300 3556.9800 1 6645.5000 3699.7600 2
25 9.2179840634863357e+00 4.4720259945158389e+01 1.3477516445004205e+03 2 0 10892.7800 882.3400 1 10429.9300 1249.5000
26 9.0540021494369807e+00 4.4583594254805114e+01 6.6099438675373074e+02 4 0 6910.7000 7901.4300 1 6882.4800 8069.0000 2
27 9.1627051449617678e+00 4.4621350224306006e+01 7.5775441102207890e+02 4 0 10174.6900 5483.2400 1 9789.6800 5695.5500
28 8.8203706933586030e+00 4.4605162450050123e+01 5.8099739300525687e+02 2 2 366.2200 8387.5600 3 1091.9700 8479.7900
29 9.0296493691657478e+00 4.4644763029912170e+01 9.5970037365005942e+02 4 0 5363.5300 5471.6200 1 5501.2700 5700.3300 2
30 8.8707908255086174e+00 4.4631943784490623e+01 6.7838304278944383e+02 4 0 99.8400 7202.8200 1 808.0200 7319.7100 2 17
31 9.1516369472211867e+00 4.4693578358782567e+01 1.4392162229883684e+03 3 1 8689.2600 2846.3200 2 10601.0200 2144.6500
32 8.9892128106029112e+00 4.4631025496481023e+01 4.3537752993669426e+02 4 0 4147.5400 6375.1800 1 4417.2200 6462.7900 2
33 9.0601370753081358e+00 4.4752830450941758e+01 6.7219945840979653e+02 4 0 5134.1000 665.2700 1 5297.1900 812.6800 2 6
34 9.1364909904848783e+00 4.4538883153522200e+01 7.9998999999865340e+02 2 0 10287.3400 9179.0500 2 11945.7700 8887.0800
```

Figure 4.4: An example of tie point files

4.4.2.2 1-step RPC correction

After all the data has been prepared, the new adjustment model can be established.

For each tie point i on image j, the RPC block adjustment model defined in image space can be expressed by following equations:

$$row_i^{(j)} = p^{(j)}(\phi_k, \lambda_k, h_k) + \varepsilon_{r_i} \tag{4.4}$$

$$column_i^{(j)} = r^{(j)}(\phi_k, \lambda_k, h_k) + \varepsilon_{c_i} \tag{4.5}$$

where $row_i^{(j)}$ and $column_i^{(j)}$ are measured row and column coordinates of the i th image point on image j, corresponding to the k th tie point with object space coordinates (ϕ, λ, h); ε_{r_i} and ε_{c_i} are random unobservable errors; $p^{(j)}(\phi_k, \lambda_k, h_k)$ and $r^{(j)}(\phi_k, \lambda_k, h_k)$ are adjustable functions for the purpose of expressing the relationship between measured image coordinates $(row, column)$ and de-normalized image coordinates $(\overline{row}, \overline{column})$ derived from inaccurate RPCs (equal to $(\overline{Line}, \overline{Sample})$ in equation (3.14) and (3.15)). An affine transformation is applied directly for transformation between $(row, column)$ and $(\overline{row}, \overline{column})$ instead of using the differences between them, as follows:

$$p^{(j)}(\phi_k, \lambda_k, h_k) = a_0 + a_c \cdot \overline{column} + a_r \cdot \overline{row} \tag{4.6}$$

$$r^{(j)}(\phi_k, \lambda_k, h_k) = b_0 + b_c \cdot \overline{column} + b_r \cdot \overline{row} \tag{4.7}$$

According to the equations above, the RPC block adjustment observation equations are as follows:

$$\begin{aligned} F_{ri} &= -row_i^{(j)} + p^{(j)}(\phi_k, \lambda_k, h_k) + \varepsilon_{r_i} \\ &= -row_i^{(j)} + a_0^{(j)} + a_c^{(j)} \cdot \overline{column}_i^{(j)} + a_r^{(j)} \cdot \overline{row}_i^{(j)} + \varepsilon_{r_i} \\ &= 0 \end{aligned} \tag{4.8}$$

$$\begin{aligned} F_{ci} &= -column_i^{(j)} + r^{(j)}(\phi_k, \lambda_k, h_k) + \varepsilon_{c_i} \\ &= -column_i^{(j)} + b_0^{(j)} + b_c^{(j)} \cdot \overline{column}_i^{(j)} + b_r^{(j)} \cdot \overline{row}_i^{(j)} + \varepsilon_{c_i} \\ &= 0 \end{aligned} \tag{4.9}$$

Applying the Taylor series expansion for observation equations above, linear model can be obtained as follows:

$$F_{i_0} + dF_i + \varepsilon = 0 \tag{4.10}$$

where

$$\begin{aligned} F_{i_0} &= \begin{bmatrix} F_{ri_0} \\ F_{ci_0} \end{bmatrix} \\ &= \begin{bmatrix} -row_i^{(j)} + p^{(j)}(\phi_k, \lambda_k, h_k) \\ -column_i^{(j)} + r^{(j)}(\phi_k, \lambda_k, h_k) \end{bmatrix} \\ &= \begin{bmatrix} -row_i^{(j)} + a_{0_0}^{(j)} + a_{c_0}^{(j)} \cdot \overline{column}_i^{(j)} + a_{r_0}^{(j)} \cdot \overline{row}_i^{(j)} \\ -column_i^{(j)} + b_{0_0}^{(j)} + b_{c_0}^{(j)} \cdot \overline{column}_i^{(j)} + b_{r_0}^{(j)} \cdot \overline{row}_i^{(j)} \end{bmatrix} = -w_{P_i} \end{aligned} \tag{4.11}$$

$$\begin{aligned} dF_i &= \begin{bmatrix} dF_{ri} \\ dF_{ci} \end{bmatrix} = \begin{bmatrix} \left.\frac{\partial F_{ri}}{\partial x^T}\right|_{x_0} \\ \left.\frac{\partial F_{ci}}{\partial x^T}\right|_{x_0} \end{bmatrix} dx \\ &= \begin{bmatrix} \left.\frac{\partial F_{ri}}{\partial x_A^T}\right|_{x_0} & \left.\frac{\partial F_{ri}}{\partial x_G^T}\right|_{x_0} \\ \left.\frac{\partial F_{ci}}{\partial x_A^T}\right|_{x_0} & \left.\frac{\partial F_{ci}}{\partial x_G^T}\right|_{x_0} \end{bmatrix} \begin{bmatrix} dx_A \\ dx_G \end{bmatrix} = \begin{bmatrix} A_{Ai} & A_{Gi} \end{bmatrix} \begin{bmatrix} dx_A \\ dx_G \end{bmatrix} \end{aligned} \tag{4.12}$$

Thus, the RPC block adjustment model can be expressed as follows:

$$\begin{bmatrix} A_A & A_G \end{bmatrix} \begin{bmatrix} dx_A \\ dx_G \end{bmatrix} + \varepsilon = w_P \tag{4.13}$$

$$\Rightarrow \; Adx + \varepsilon = w \tag{4.14}$$

Where ε is a vector of random errors; dx_A and dx_G stand for the vector of corrections for unknown parameters. dx_A is the vector of corrections to affine RPC parameters for n overlapping images, while dx_G is the vector of corrections to object coordinates for p tie points:

$$\begin{aligned} dx_A = \Big[& da_0^{(1)} \; da_c^{(1)} \; da_r^{(1)} \; db_0^{(1)} \; db_c^{(1)} \; db_r^{(1)} \\ & \ldots \; da_0^{(n)} \; da_c^{(n)} \; da_r^{(n)} \; db_0^{(n)} \; db_c^{(n)} \; db_r^{(n)} \Big]^T \end{aligned} \tag{4.15}$$

$$dx_G = \left[d\phi_1 \; d\lambda_1 \; dh_1 \; \ldots \; d\phi_p \; d\lambda_p \; dh_p \right]^T \tag{4.16}$$

w_P is the vector of misclosures for the image-space coordinates derived from equation (4.6)-(4.9). Thus, sub-vector of misclosures for the image-space coordinates of the i th image point can be described by:

$$\begin{aligned} & w_{P_i} \\ = & \begin{bmatrix} row_i^{(j)} - a_{0_0}^{(j)} - a_{c_0}^{(j)} \cdot \overline{column}_i^{(j)} - a_{r_0}^{(j)} \cdot \overline{row}_i^{(j)} \\ column_i^{(j)} - b_{0_0}^{(j)} - b_{c_0}^{(j)} \cdot \overline{column}_i^{(j)} - b_{r_0}^{(j)} \cdot \overline{row}_i^{(j)} \end{bmatrix} \end{aligned} \tag{4.17}$$

Under the resumption of $row_i^{(j)} = \overline{row}_i^{(j)}$ and $column_i^{(j)} = \overline{column}_i^{(j)}$, the initial values for affine transformation parameters are always given by $(0\;0\;1\;0\;1\;0)$ corresponding to $(a_{0_0} \; a_{c_0} \; a_{r_0} \; b_{0_0} \; b_{c_0} \; b_{r_0})$.

Then it is necessary to calculate design matrix A. Through calculation of derivation, the jacobian matrix A_A, A_G is obtained. Sub-vector of design matrix A_A (jacobian matrix) for affine RPC parameters is expressed as follows:

$$A_{A_i} = \begin{bmatrix} 0 \; \ldots \; 0 \; 1 \; \overline{column}_i^{(j)} \; \overline{row}_i^{(j)} \; 0 & 0 & 0 & 0 \; \ldots \; 0 \\ 0 \; \ldots \; 0 \; 0 & 0 & 0 & 1 \; \overline{column}_i^{(j)} \; \overline{row}_i^{(j)} \; 0 \; \ldots \; 0 \end{bmatrix} \tag{4.18}$$

Where A_{A_i} is for the i th image point on the j th image

Similarly, sub-vector of design matrix A_G (jacobian matrix) for object coordinates is given by (for the k th tie point which is also the i -th image point on the j -th image):

$$A_{G_i} = \begin{bmatrix} 0 \; \ldots \; 0 \; \left.\frac{\partial F_{ri}}{\partial \phi_k}\right|_{x_0} \; \left.\frac{\partial F_{ri}}{\partial \lambda_k}\right|_{x_0} \; \left.\frac{\partial F_{ri}}{\partial h_k}\right|_{x_0} \; 0 \; \ldots \; 0 \\ 0 \; \ldots \; 0 \; \left.\frac{\partial F_{ci}}{\partial \phi_k}\right|_{x_0} \; \left.\frac{\partial F_{ci}}{\partial \lambda_k}\right|_{x_0} \; \left.\frac{\partial F_{ci}}{\partial h_k}\right|_{x_0} \; 0 \; \ldots \; 0 \end{bmatrix} \tag{4.19}$$

The structure of A matrix is determined by numbers of tie points. It is obvious to see that for every tie point in each image two rows are needed. In one practical example, which contains four stereo images (2 stereo pairs: A.183, B.183, A.229 and B.229), 431 SIFT tie points have been found. Among them, 254 tie points lie in all the 4 images, 55 tie points are included in 3 images and 122 points are able to be found in only 2 images. Therefore, the number of observations which is also number of rows of design matrix A can be calculated by $254\times4\times2+55\times3\times2+122\times2\times2+6\times4=2874$. In addition, the number of parameters which is also number of columns of design matrix A is given by $431\times3+4\times6=1317$, which includes corrections to all 3D object coordinates and affine parameters.

With the a priori covariance matrix of the vector of misclosures w_P:

$$C_w=\begin{bmatrix}C_A & C_G\end{bmatrix} \tag{4.20}$$

Then it is able to handle the block adjustment for all selected images simultaneously. However, without ground control the results of adjustment are not accurate (see the results in next chapter). Thus, SRTM DSM covering the whole areas of all stereo scenes is chosen as the ground control (see Figure 4.5). In the new adjustment model, DSM data are directly insert into design matrix and the vector of misclosures. This process is introduced step by step as follows.

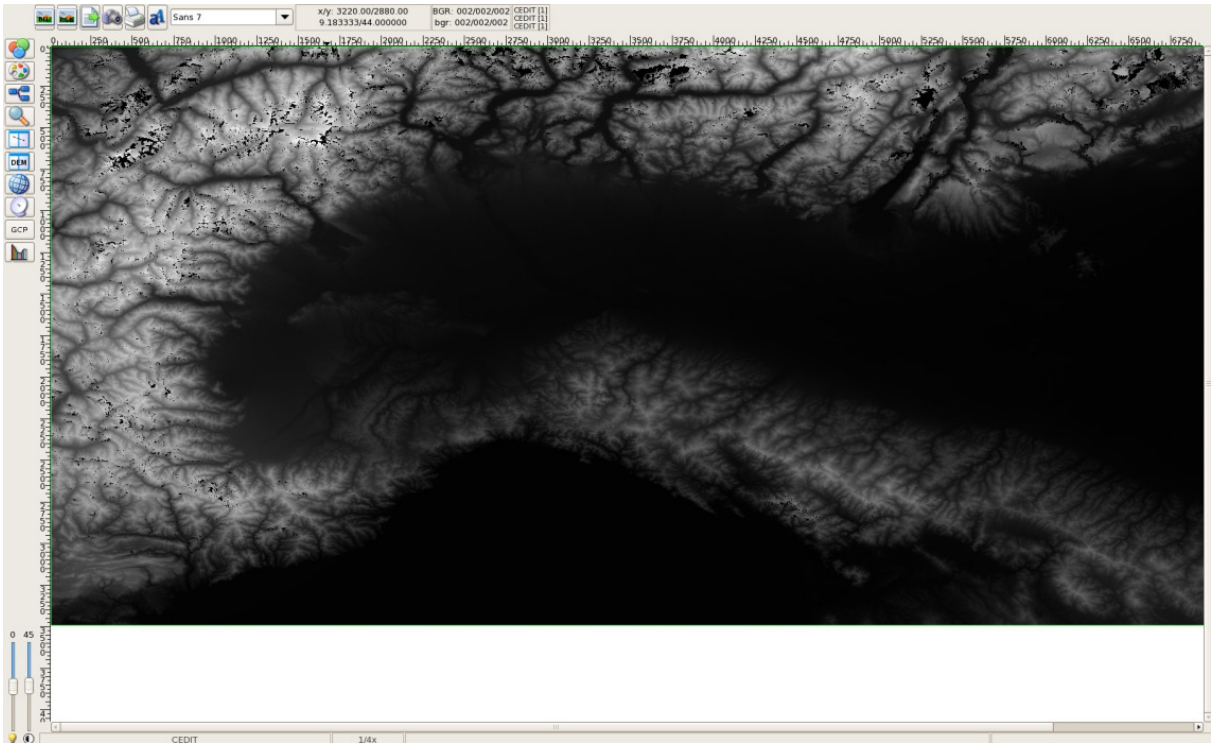

Figure 4.5: SRTM DSM of North Italy in Idibias window

At first, the vector of misclosures should be formed. In the first step, each tie point object coordinates (ϕ,λ,h) is transformed into the DSM image-space. Based on these resulting pixel coordinates $(row,column)$, the nearest neighborhood integer values r_{left}, c_{left}, r_{right}, c_{right} are easily to be found. By using DSM data, it is able to acquire height values

(h_1, h_2, h_3, h_4) for the four nearest neighborhood points (r_{left}, c_{left}), (r_{right}, c_{left}), (r_{left}, c_{right}) and (r_{right}, c_{right}). Then the DSM height of all tie points can be obtained through bilinear interpolation as follows:

$$\begin{aligned} dr &= row - r_{left} \\ dc &= column - c_{left} \end{aligned} \tag{4.21}$$

$$\begin{aligned} \Rightarrow\ h_{DSM} = &(1-dc)\times(1-dr)\times h_1 + (1-dc)\times dr \times h_2 + \\ &dc\times(1-dr)\times h_3 + dc\times dr\times h_4 \end{aligned} \tag{4.22}$$

Finally, the vector of misclosures for DSM terms can be described by height difference between DSM and tie points, as follows:

$$v_i = h_{DSM}(\phi_i, \lambda_i) - h_i \tag{4.23}$$

Along with misclosures it is able to acquire the design matrix for DSM terms. For the purpose of calculating partial derivatives with respect to ϕ_i, λ_i, h_i, the 4 neighborhood pixels that are 0.5 pixel away from each tie point in two directions (row and column directions) are selected. Similar to the method above, by bilinear interpolation DSM heights for 4 nearest neighborhood points can be obtained. Then it is able to calculate the horizontal derivatives because the slope in row and column directions are easily calculated through DSM heights differences between neighborhood points. In addition, derivations in height direction are always -1. Finally, the design matrix A_{DSM} for the DSM terms can be given by (for points $i,\ i+1$):

$$A_{DSM_i} = \begin{bmatrix} 0\ \dots\ 0 & \left.\frac{\partial v_i}{\partial \phi_i}\right|_{x_0} & \left.\frac{\partial v_i}{\partial \lambda_i}\right|_{x_0} & -1 & 0 & 0 & 0 & 0\ \dots\ 0 \\ 0\ \dots\ 0 & 0 & 0 & 0 & \left.\frac{\partial v_{i+1}}{\partial \phi_{i+1}}\right|_{x_0} & \left.\frac{\partial v_{i+1}}{\partial \lambda_{i+1}}\right|_{x_0} & -1 & 0\ \dots\ 0 \end{bmatrix} \tag{4.24}$$

Obviously, for each tie point there is one corresponding column in design matrix A_{DSM}. Thus, for the example including the 4 stereo images above, A_{DSM} has 413 rows and the same number of columns as A_G. Finally, the whole design matrix A has $2874 + 431 = 3305$ rows.

After adding a priori covariance information of DSM terms C_{DSM}, the whole adjustment model can be given as follows:

$$\begin{bmatrix} A_A & A_G \\ 0 & A_{DSM} \end{bmatrix} \begin{bmatrix} dx_A \\ dx_G \end{bmatrix} + \varepsilon = \begin{bmatrix} w_P \\ v \end{bmatrix} \tag{4.25}$$

$$\Rightarrow\ Adx + \varepsilon = w \tag{4.26}$$

With the a priori covariance matrix of the vector of misclosures:

$$C = \begin{bmatrix} C_A & C_G \\ 0 & C_{DSM} \end{bmatrix} \tag{4.27}$$

Following Gauss-Markov model, a least-squares solution for the corrections to unknown parameters is able to be obtained:

$$d\hat{x} = (A^T PA)^{-1} A^T Pw = (A^T C^{-1} A)^{-1} A^T C^{-1} w \tag{4.28}$$

The updated covariance matrix which is meaningful for results evaluation is obtained by following equation:

$$C_{\hat{x}} = (A^T PA)^{-1} = (A^T C^{-1} A)^{-1} \tag{4.29}$$

The original adjustment model is nonlinear, so that an iterative approach is necessary for block adjustment. If corrections to unknown parameters are larger than given convergence requirement, initial input parameters x_0 should be updated by $x_{0(new)} = \hat{x} = x_{0(old)} + d\hat{x}$ and a new iteration process is repeated until convergence requirement is met.

The following flow chart describes the whole working process of 1-step RPC block adjustment model that is introduced above:

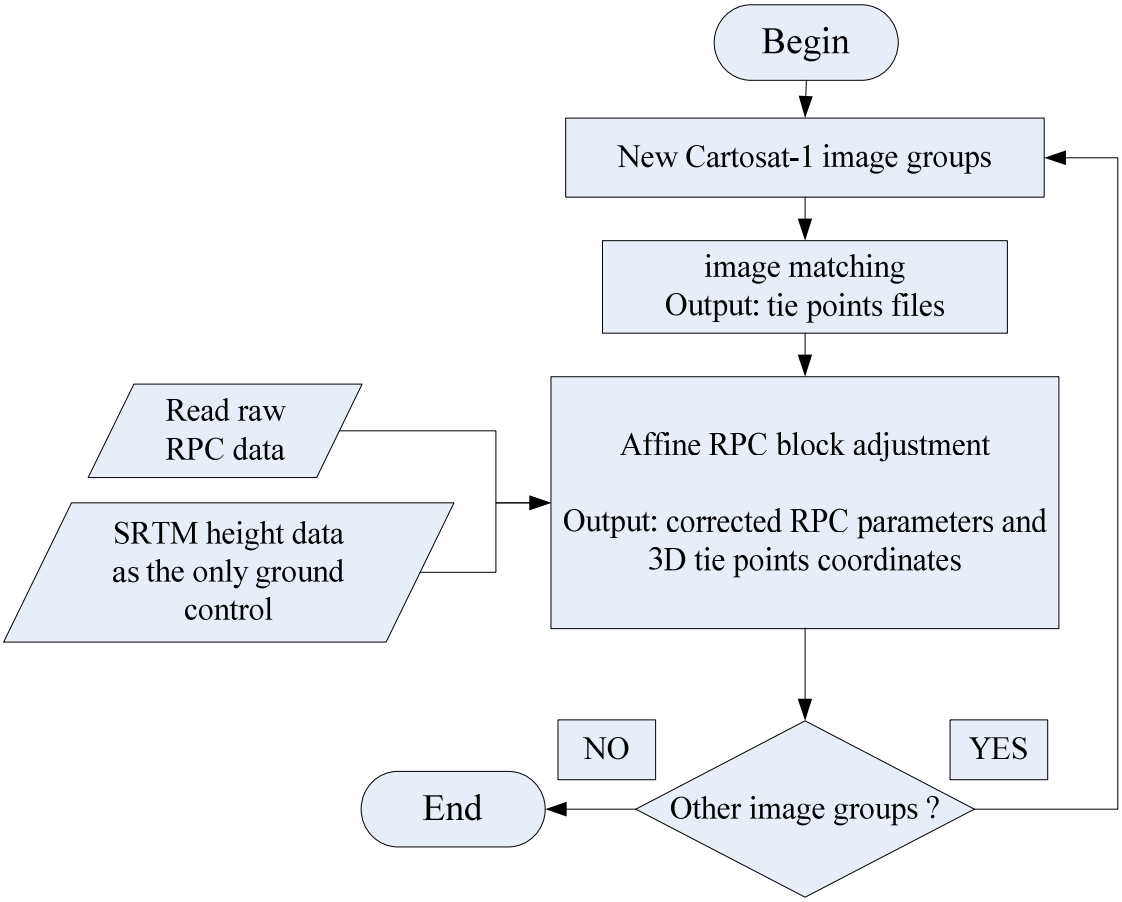

Figure 4.6: Working process of 1-step RPC correction

5 Evaluation of results for dataset 'North Italy'

Based on 1-step block adjustment models introduced above, a large block adjustment for dataset 'North Italy' is processed. After that, the improvement for RPCs parameters and 3D tie point coordinates are evaluated in this chapter. Various results (e.g. adjusted results of 1, 2 and all stereo pairs without/with SRTM DSM) are compared with each other in this chapter.

5.1 Overview of stereoblocks

As demonstrated in chapter 1.2, the main data resource of this diploma thesis is a block of 428 Cartosat-1 stereo pairs (region in north Italy). The overview of these images is given by following figure:

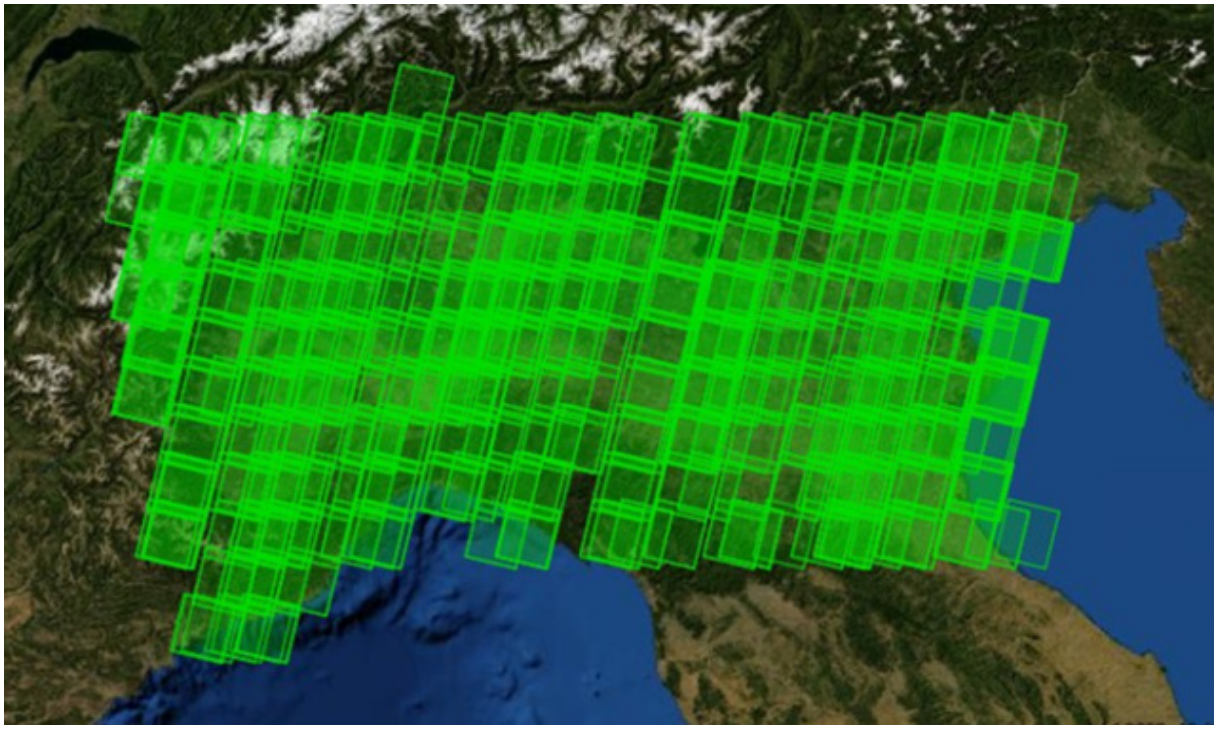

Figure 5.1: Overview of all Cartosat-1 stereo images in north Italy

From the figure some characteristics are discovered. This large block covers a region containing various kinds of landforms (such as mountains, flat areas and sea). The middle of this block is totally occupied by flat areas. Additionally, these flat areas are surrounded by mountainous areas in north, south and west directions. It is also very important to point out that the edge of this block in the east contains large amounts of sea and flat seaside. Finally, a few scenes at the south edge cover the areas of Mediterranean Sea.

Some typical Cartosat-1 images are given as follows:

Figure 5.2: City Genoa

Figure 5.3: Stereo image A.47 (cover the hilly areas and the Mediterranean Sea)

5.2 Results of 1-step block adjustment

5.2.1 Adjustment results of 1 stereo pair (1 step)

In order to make the process of the block adjustment easily work, a stereo pair A.183, B.183 which is mountainous area near the city Genoa is selected (see Figure 5.4).

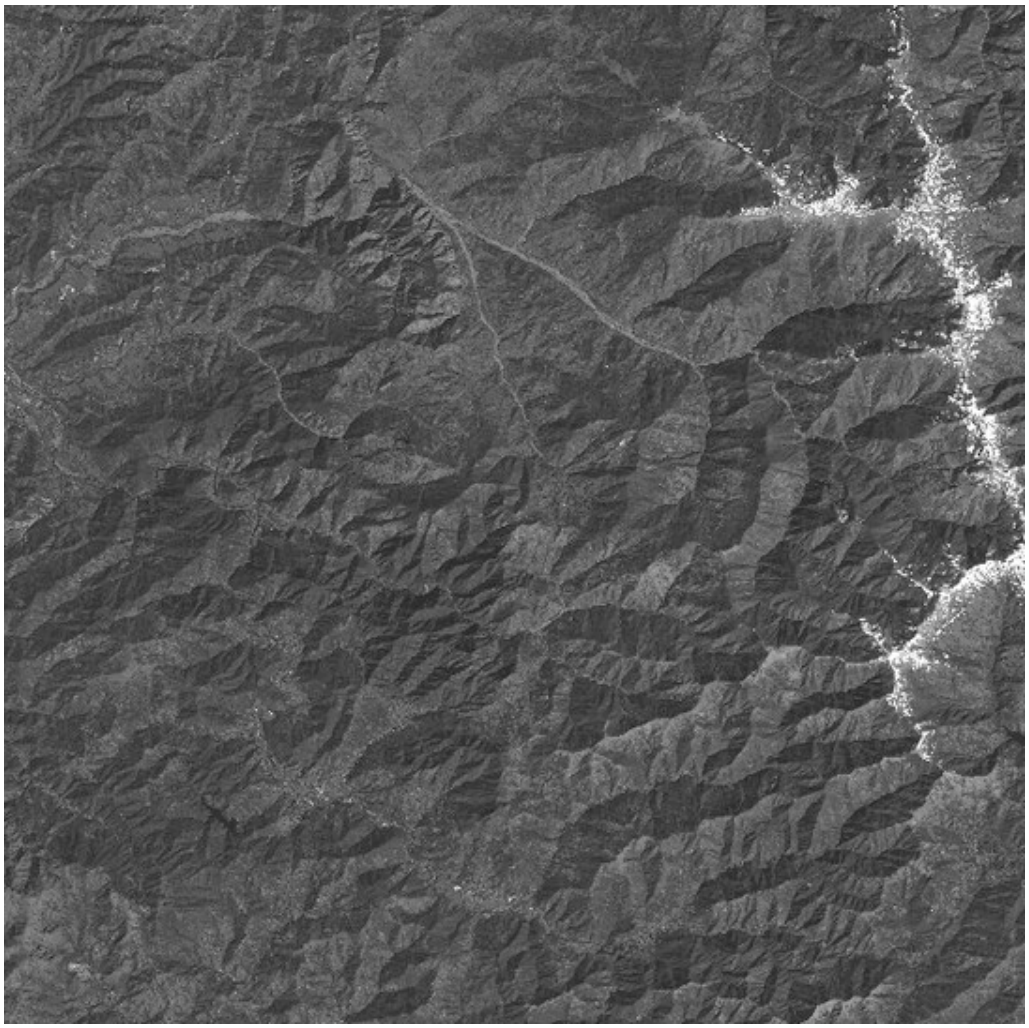

Figure 5.4: Cartosat-1 stereo scene A.183

In this scene, 317 SIFT tie points (accuracy: 0.5 pixel) are provided for block adjustment. The tie point distribution is given as follows (see Figure 5.5).

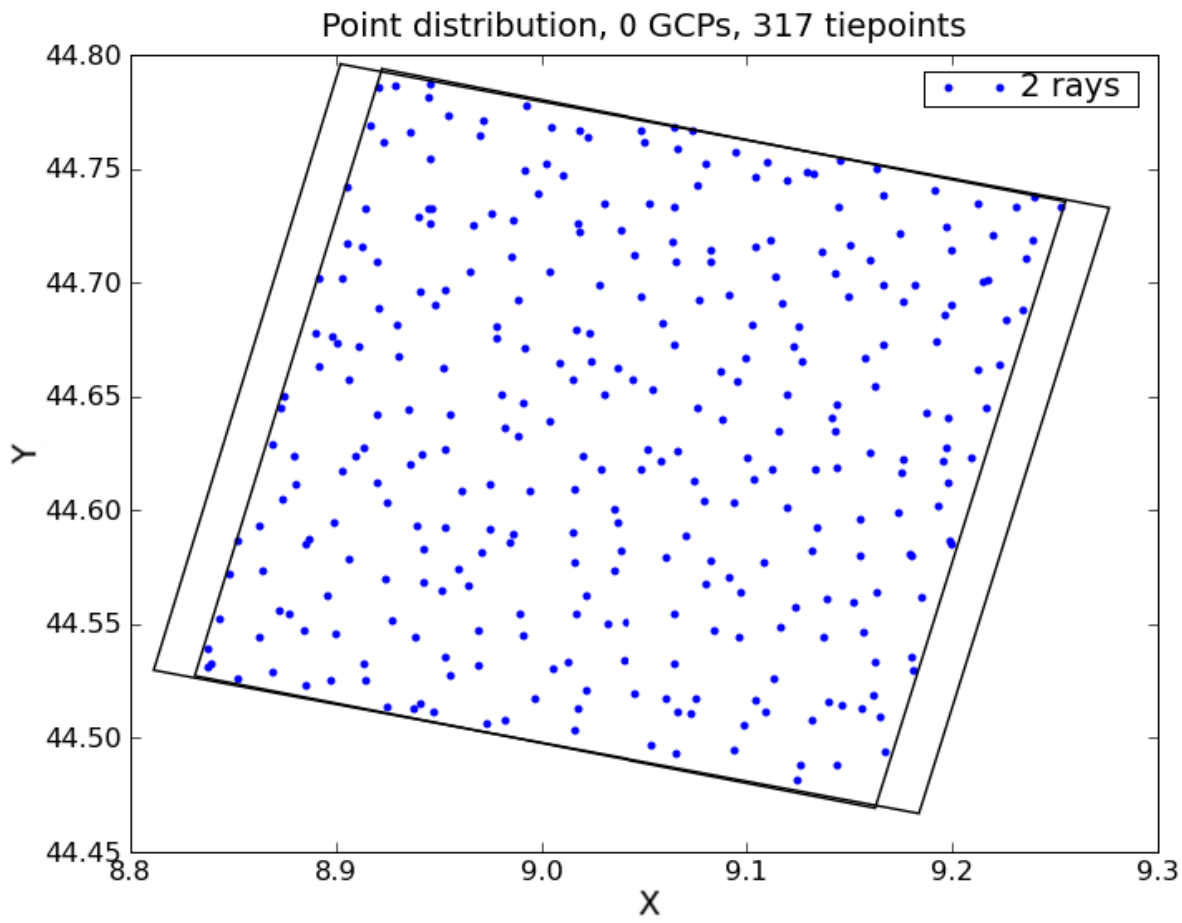

Figure 5.5: Tie points distribution of stereo pair 183 (X-axis: longitude, Y-axis: latitude, unit: degree)

By using 1-step block adjustment model, the RPCs parameters and tie points are improved. In order to make a better evaluation against this model, two situations are considered: without ground control and with ground control (SRTM DSM).

For the 1-step model without ground control, equation (4.13) is used to estimate the unknowns. This adjustment problem includes $317 \times 3 = 951$ parameters and $317 \times 2 \times 2 = 1268$ observations for this example. With the purpose of allowing a free adjustment without ground control, it is necessary to add constraint terms. Related to initial values of affine RPCs parameters, the weights of affine parameters $(a_{c_0}\ a_{r_0}\ b_{c_0}\ b_{r_0})$ are given by $1/(10^{-4})^2$, while the weights of bias parameters $(a_{0_0}\ b_{0_0})$ are given by $1/(200)^2$.

It is also essential to point out that the accuracy of SRTM DSM (ground control) is only circa 10 meters, while the residuals in image space should be under 0.3 pixel (ca. 0.75m). The resolution of the SRTM is 3 arc seconds, which roughly corresponds to a 90m grid. According to these two a priori standard deviations, it is simple to calculate the weight of SRTM DSM $(10m \Rightarrow weight: 1/(10)^2 = 0.01)$, which is much smaller than the weight of tie points $(0.3\,pixel \Rightarrow weight: 1/(0.3)^2 = 11.11)$.

Before starting the adjustment, it is useful to calculate the reprojection errors which reflect the existing RPCs accuracy. Thus, it is need to look for the predicted tie points coordinates in

image space. Compared to given image coordinates in tie point files, following reprojection errors and their histogram can be obtained (see Figure 5.6):

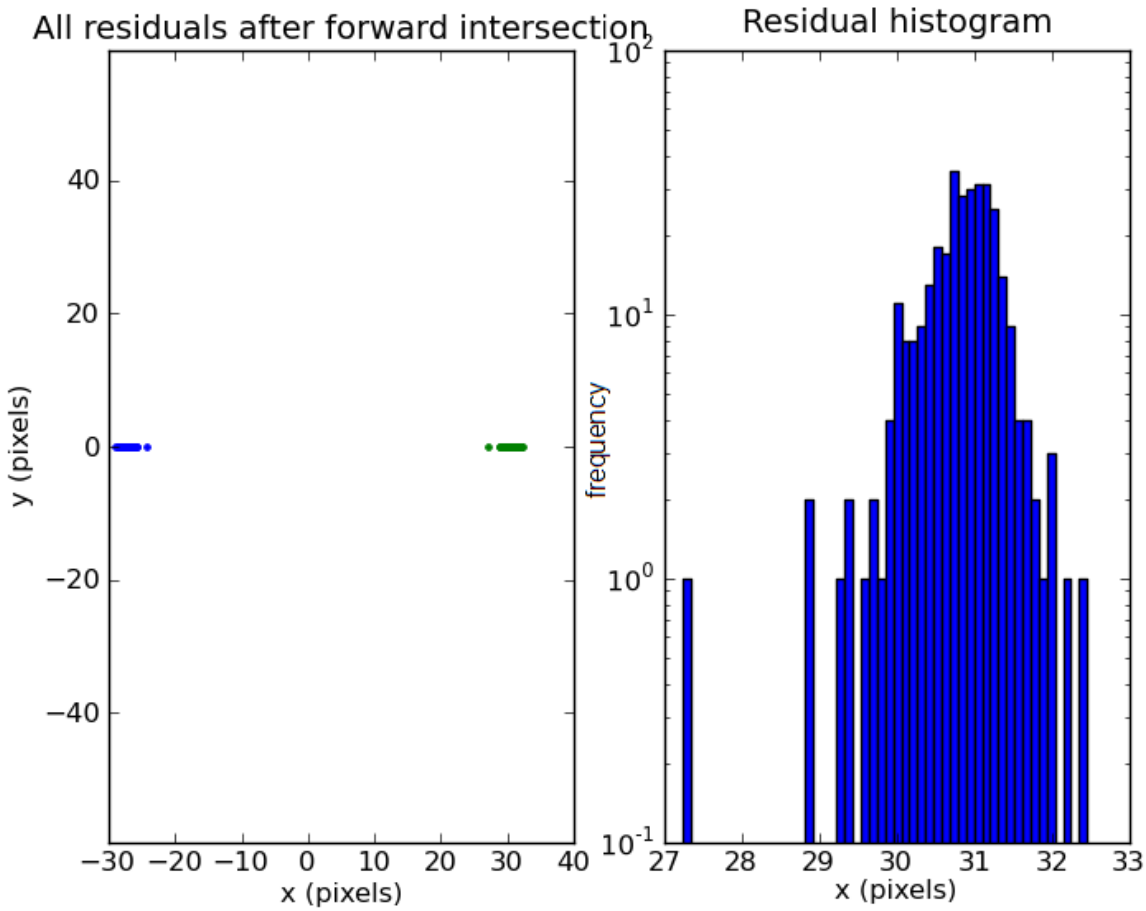

Figure 5.6: Reprojection errors for 1 stereo pair (before adjustment)

Obviously, before block adjustment the reprojection errors in row direction are relatively large (see the left figure). This fact can be explained by the poor accuracy of raw RPCs parameters. Then as the residual histogram in the right image shows (x-axis shows absolute horizontal errors $(=\sqrt{(\Delta x)^2+(\Delta y)^2})$ and y-axis expresses the frequency logarithmically), the main part of absolute horizontal reprojection errors stays in the interval between 29 and 32 pixels, which reflect an inaccurate RPCs accuracy of over 100 meters.

After 1-step block adjustment, the reprojection errors are expected to improve much. Reprojection errors and their histogram after using 1-step block adjustment model without ground control are given. (see Figure 5.7)

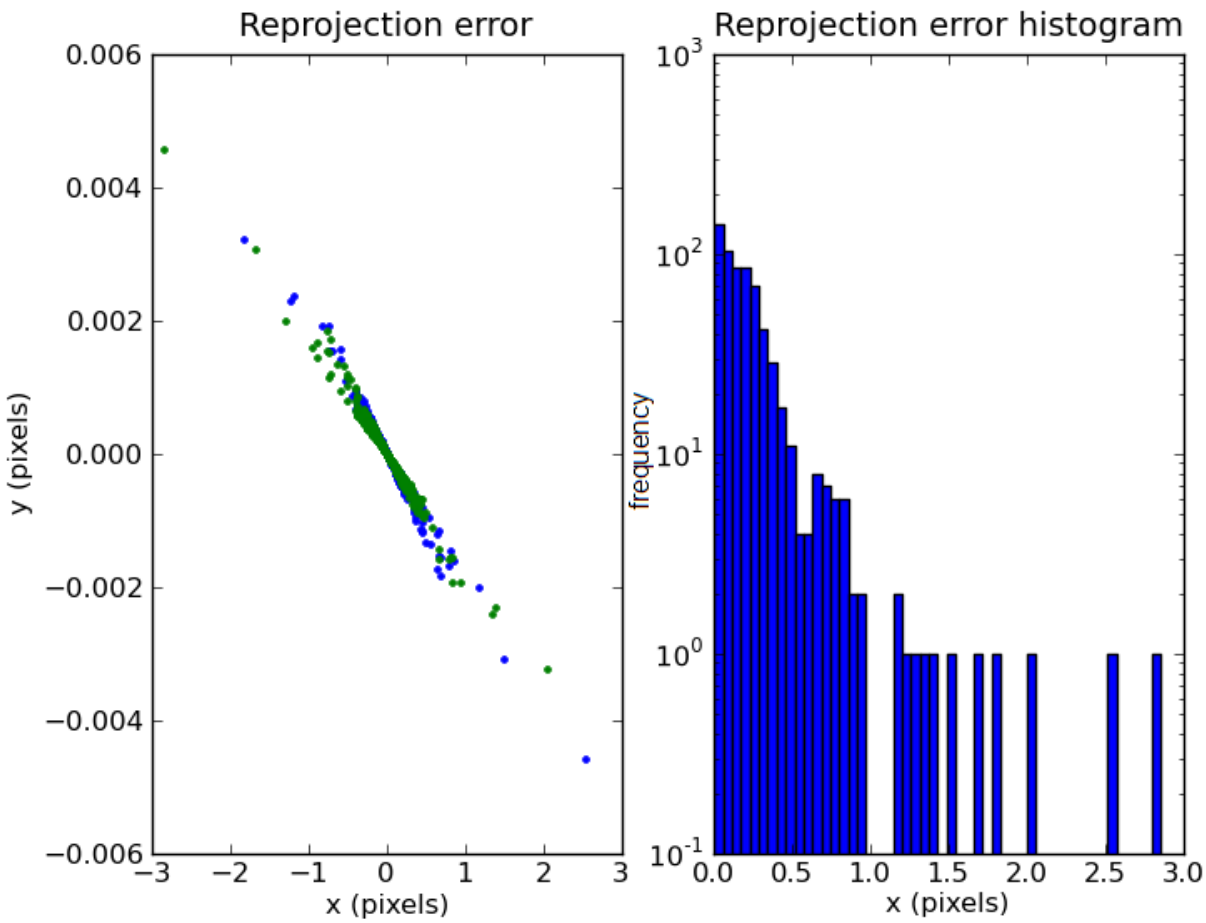

Figure 5.7: Reprojection errors after adjustment for 1 stereo pair (without DSM ground control)

As expected, reprojection errors reduced significantly after adjustment. Maximal value in row direction is below 3 pixels and the distribution of errors is like a nearly linear form. Lower residuals happen in row direction compared to the case before adjustment, as errors here are propagated into the height component of the object coordinates. The main part of absolute horizontal errors $(=\sqrt{(\Delta x)^2+(\Delta y)^2})$ presents in the interval between 0 and 1.

Then, the results with ground control are calculated, too. Its histogram of absolute horizontal reprojection errors is very similar to the histogram without ground control, but the distribution of reprojection errors is different (larger in column direction compared to the result without ground control, as the DSM observation term does not allow arbitrarily large height errors), as shown by the following figure:

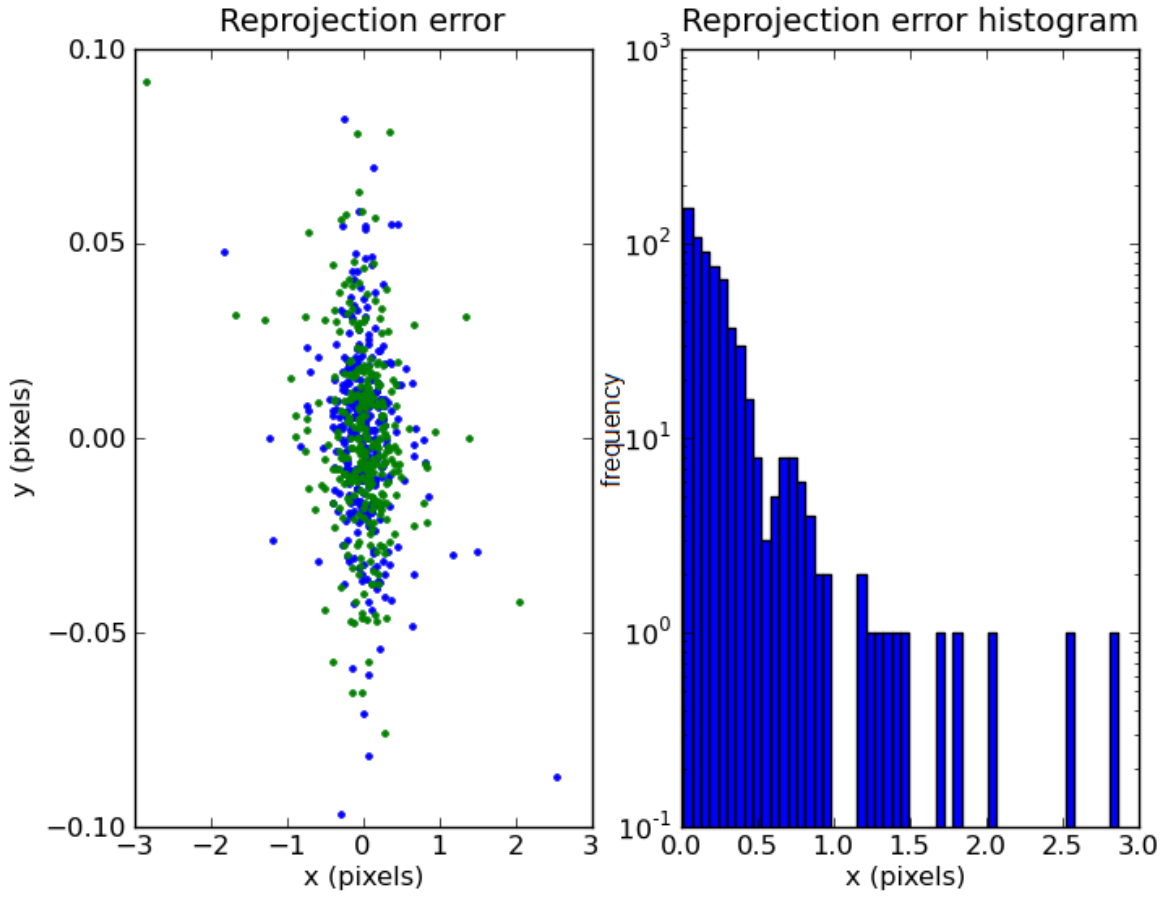

Figure 5.8: Reprojection errors after adjustment for 1 stereo pair (with DSM ground control)

Then the statistical results of reprojection errors are given (see Table 5.1).

		mean	median	std	min	max
Before adjustment	A.183	27.46	27.52	0.48	24.27	28.92
	B.183	30.81	30.88	0.54	27.23	32.45
Without DSM	A.183	0.21	0.16	0.26	0.00	2.55
	B.183	0.24	0.18	0.29	0.00	2.86
With DSM	A.183	0.22	0.16	0.26	0.01	2.54
	B.183	0.24	0.18	0.29	0.01	2.86

Table 5.1: Statistical results of reprojection errors for a stereo pair (unit: pixel)

Clearly, mean values and median values improve much compared to the results before adjustment. In addition, standard deviations are only about a half of previous values. However, the reprojection errors for the latter two situations (without ground control and with ground control) vary only a little. Thus, in order to observe the difference of accuracy between these two situations, only the observation of reprojection errors is not enough. Here, the covariance matrix of corrected tie points is chosen as an important standard of accuracy. According to the explanation in the appendix for quality evaluation, plotting the confidence ellipse is a good way to visually show the covariance information of tie points. Especially, the great attention is paid on the horizontal accuracy of tie points. For this purpose, 90% confidence ellipses for horizontal coordinates of all adjusted tie points are plotted, as shown in Figure 5.9 and Figure 5.10:

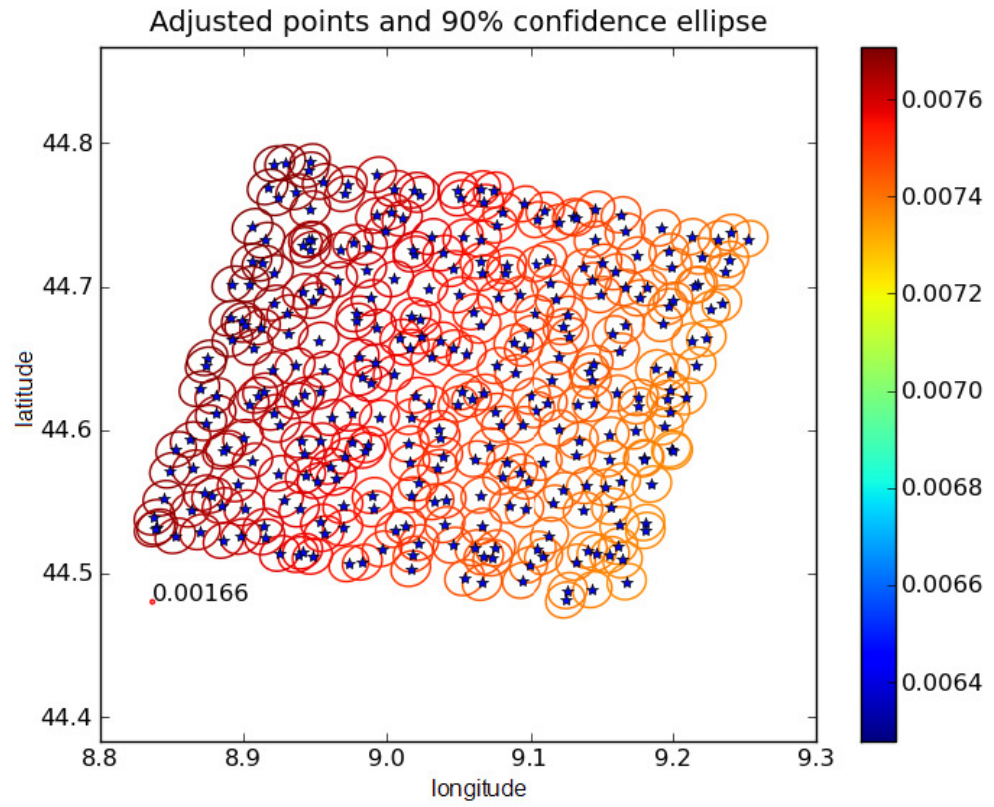

Figure 5.9: Confidence ellipse for 1 stereo pair (without DSM ground control, unit: degree)

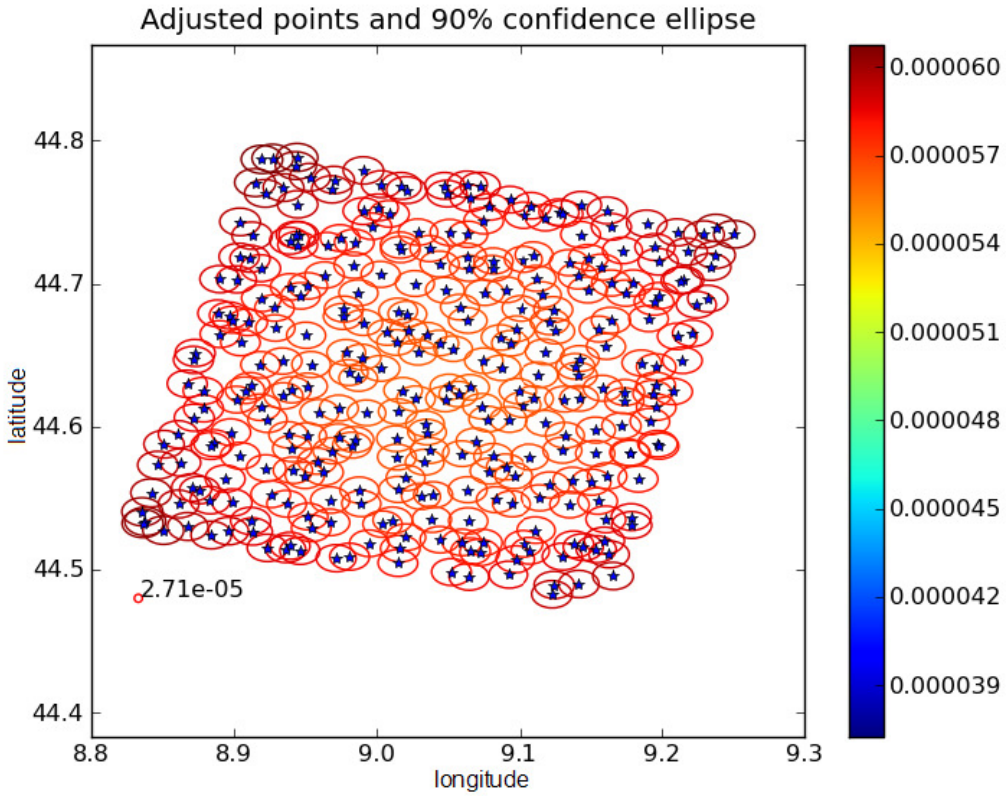

Figure 5.10: Confidence ellipse for 1 stereo pair (with DSM ground control, unit: degree)

In order to show the confidence ellipses better, different scales are used for these two cases (Without DSM: 0.00166 degree; With DSM: 2.71e-5 degree). As expected, it is obvious to see that DSM terms significantly reduce the uncertainty of the estimated object points (see the color bar): (Without DSM) between 0.0064 and 0.0076 degrees, (With DSM) between 0.000039 and 0.00006 degrees.

5.2.2 Adjustment results of 4 images (1 step)

In this section, two Cartosat-1 scenes (including 4 stereo images) are chosen to test the effect of 1-step block adjustment model. Along with A.183 and B.183, an additional nearest neighbor scene A.229 and B.229 are selected (see Figure 5.11).

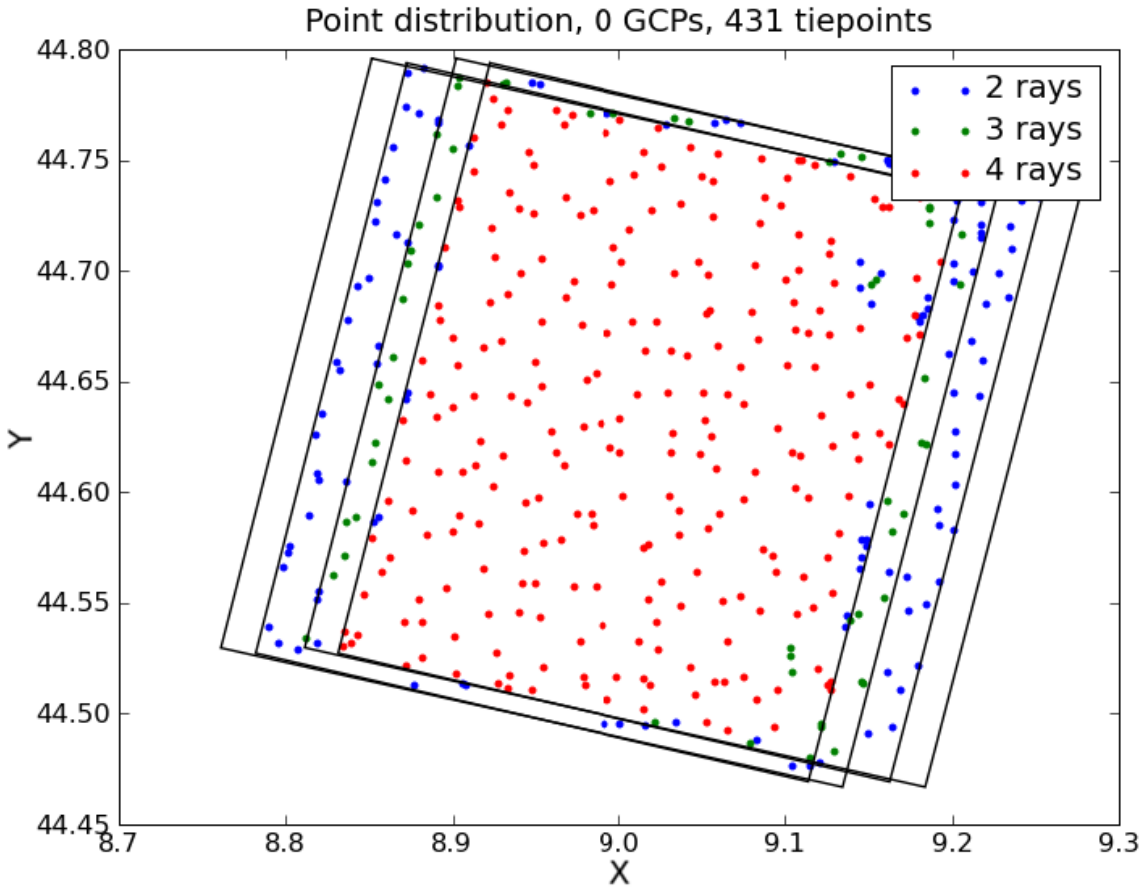

Figure 5.11: Tie points distribution of 2 stereo pairs (X-axis: longitude, Y-axis: latitude, unit: degree)

As the figure above presents, 431 SIFT tie points are selected for block adjustment. Blue points mean that they exist in two images; green points mean that they can be found in three images and red points are involved in all four images.

Similar to the situation of 1 stereo pair, the reprojection errors before adjustment for these 4 images are plotted (see Figure 5.12).

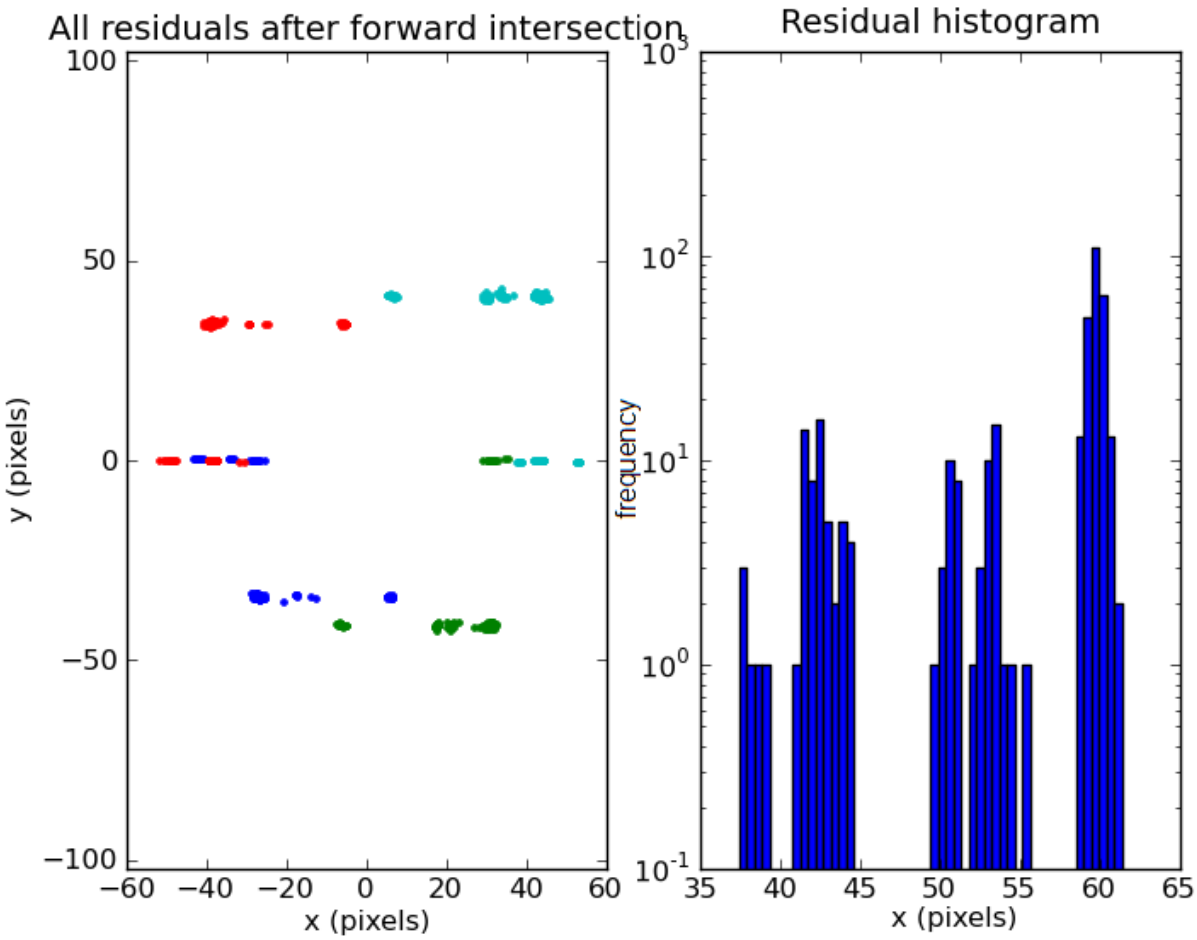

Figure 5.12: Reprojoction errors for 2 stereo pairs (before adjustment)

The figure above enables to see that the reprojection errors before adjustment are very large. Compared to the situation of 1 stereo pair (see Figure 5.6), errors in row direction nearly reach 60 pixels and these values give an indication of absolute geolocation accuracy of Cartosat-1 by using raw RPCs parameters. In addition, some tie points can be found in all the four stereo images. Under the effects of inaccurate RPCs parameters of all 4 images the errors of these points in column direction increase much and even almost reach 40 pixels. Furthermore, as residual histogram shows, the absolute horizontal errors $(=\sqrt{(\Delta x)^2+(\Delta y)^2})$ are between 35 and 65 pixels.

After 1-step block adjustment, the improved reprojection errors are expected. Both the results without ground control and the results with ground control are calculated. Reprojection errors and their histograms after using 1-step block adjustment model can be plotted, too (see Figure 5.13 and Figure 5.14).

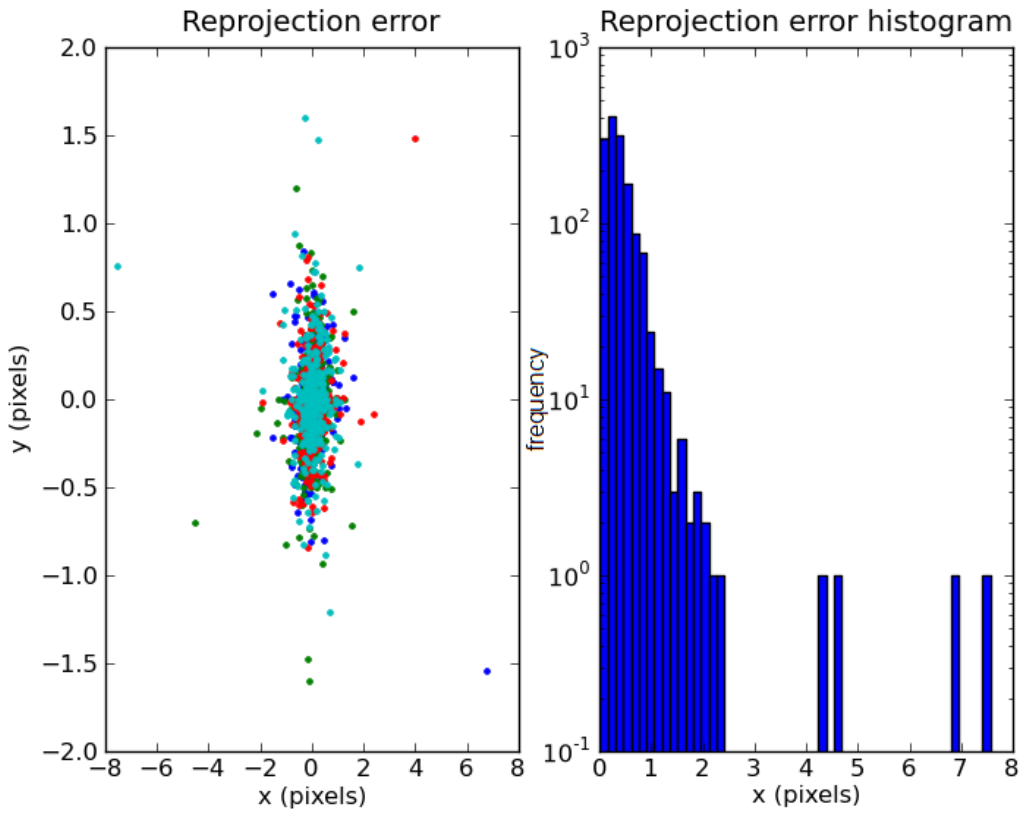

Figure 5.13: Reprojection errors after adjustment for 2 stereo pairs (without DSM ground control)

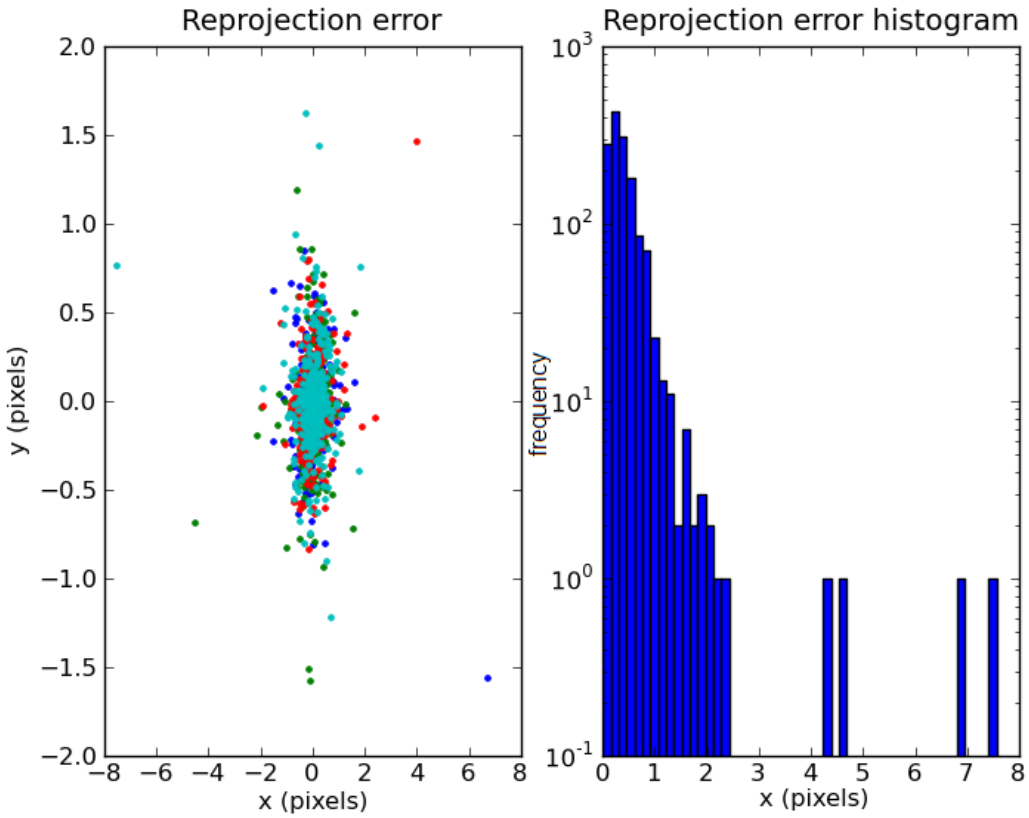

Figure 5.14: Reprojection errors after adjustment for 2 stereo pairs (with DSM ground control)

As expected, reprojection errors reduced sharply after 1-step block adjustment. All reprojection errors in row direction present below 8 pixels, while in column direction no more than 2 pixels. As shown in reprojection error histogram, the main part of absolute horizontal errors $(=\sqrt{(\Delta x)^2+(\Delta y)^2})$ stays below 2 pixels. Furthermore, the reprojection errors without ground control and with ground control show nearly the same distribution and histogram, as 3 or more ray points constrain all object coordinates.

It is clearer to see the differences when the results of statistics are given by following table:

		mean	median	std	min	max
Before adjustment	A.183	40.93	43.45	5.38	25.72	44.67
	B.183	47.84	51.41	6.67	28.86	52.94
	A.229	49.00	51.72	5.66	30.65	53.41
	B.229	55.70	59.46	6.68	37.43	61.36
Without DSM	A.183	0.38	0.29	0.44	0.00	6.92
	B.183	0.39	0.30	0.38	0.00	4.57
	A.229	0.37	0.30	0.36	0.00	4.25
	B.229	0.40	0.31	0.48	0.01	7.56
With DSM	A.183	0.39	0.30	0.44	0.00	6.90
	B.183	0.39	0.30	0.38	0.00	4.57
	A.229	0.38	0.31	0.35	0.01	4.26
	B.229	0.41	0.31	0.48	0.02	7.56

Table 5.2: Statistical results of reprojection errors for 2 stereo pairs (unit: pixel)

It is again obvious that mean values and median values after adjustment improve much comparing to the results before adjustment. In addition, standard deviations reduce below half pixel.

As demonstrated before, the reprojection errors after 1-step block adjustment are nearly the same even after adding DSM terms. Thus, in order to observe the difference of accuracy between these two situations (without ground control and with ground control), the covariance matrix of corrected tie points is also observed. 90% confidence ellipses for horizontal coordinates of all adjusted tie points are plotted, as shown in Figure 5.15 and Figure 5.16.

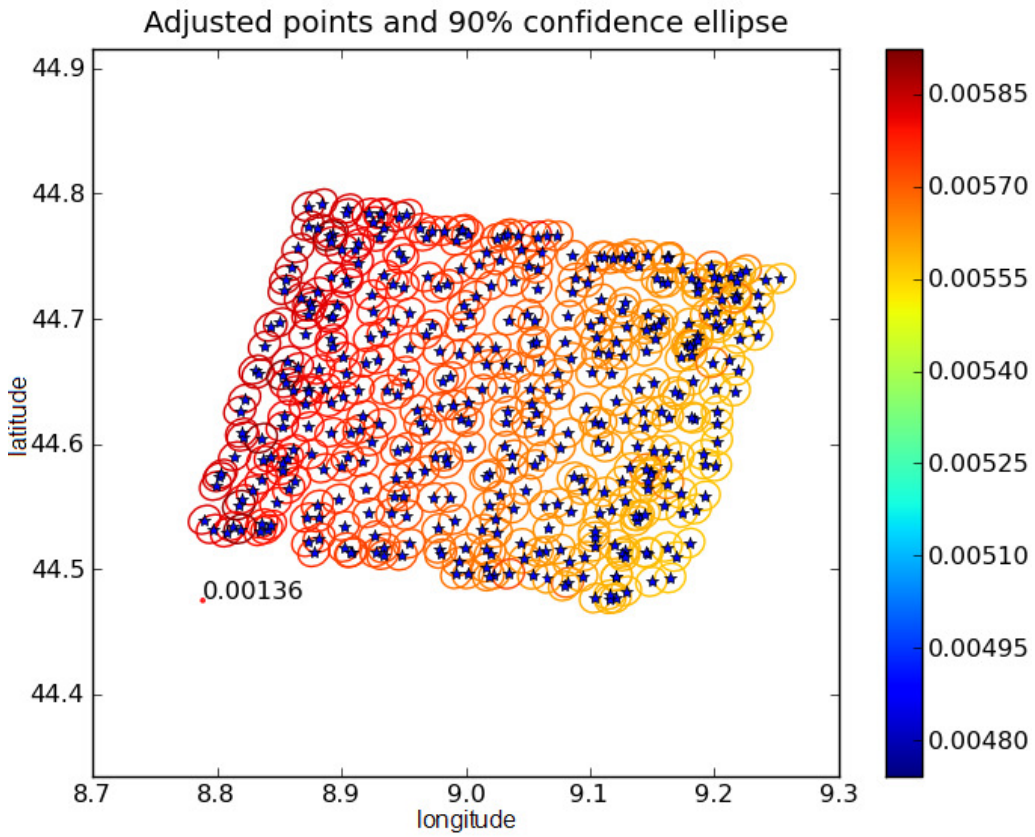

Figure 5.15: Confidence ellipse for 2 stereo pairs (without DSM ground control, unit: degree)

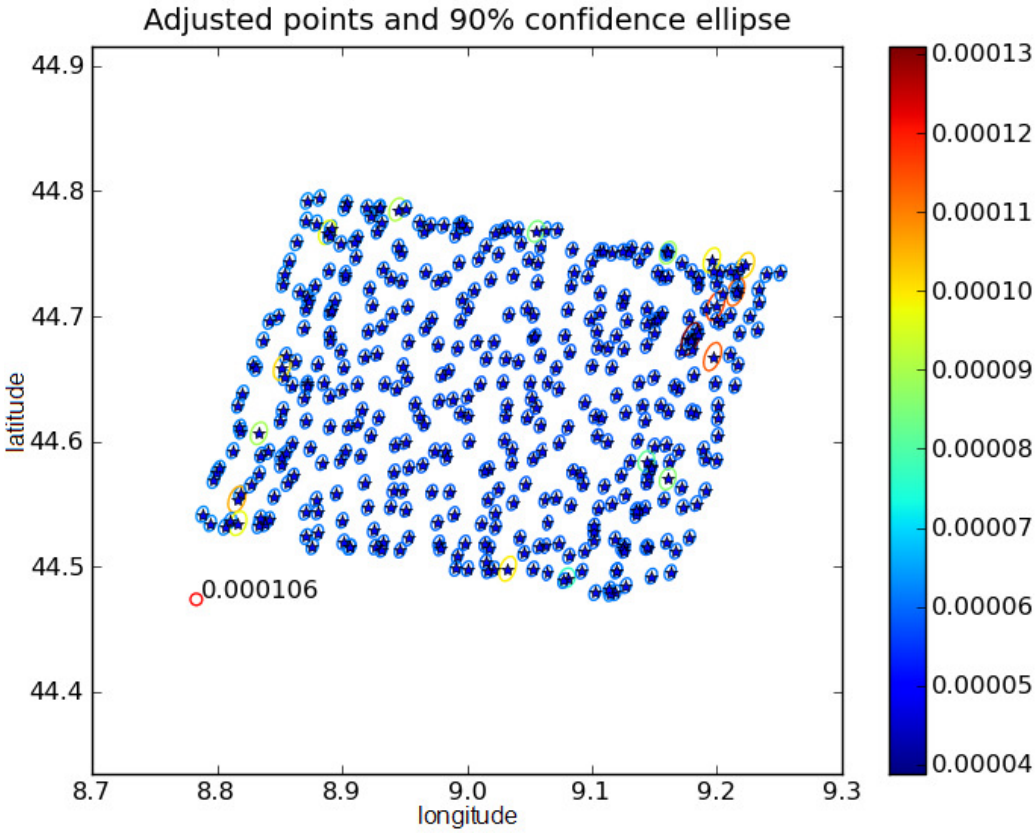

Figure 5.16: Confidence ellipse for 2 stereo pairs (with DSM ground control, unit: degree)

Similar to the 1-stereopair situation, different scales are used for these two cases. It is obvious that after adding DSM terms into 1-step adjustment model the uncertainty of the estimated object points reduce significantly, too: (Without DSM) between 0.0048 and 0.00585 degrees, (With DSM) between 0.00004 degrees and 0.00013 degrees.

5.2.3 Large block adjustment results of all stereo pairs (1 step)

In this chapter, all stereo images (over 400 stereo pairs) are selected to test 1-step block adjustment model (including scene 183), as shown by the following figure:

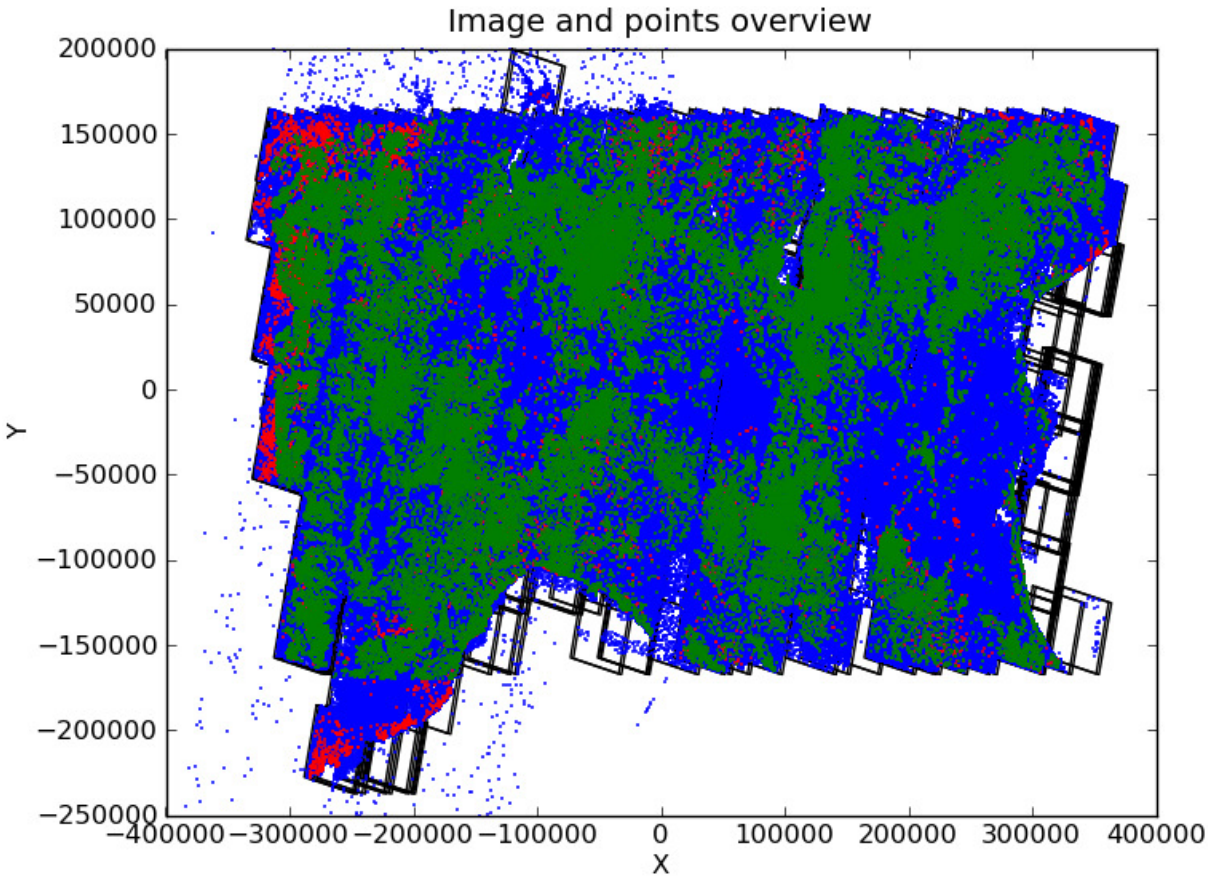

Figure 5.17: Scenes and points overview (unit of X-axis and Y-axis: meter)

2358629 tie points (including both SIFT and LSM tie points), 14384 GCPs derived from Landsat dataset and 96472 CPs automatically matched against the Euro-Map 2D mosaic are selected for the whole region. Blue points stand for tie points; red points are Landsat GCPs and green points are check points. For the purpose of processing the block adjustment without ground control, a priori standard deviation of Landsat GCPs is set to 500m, which leads to a tiny weight in the adjustment model. In this way, the influence of ground control can be simply ignored. In addition, tie points have a priori standard deviation of 0.2 pixel, and SRTM DSM has a priori standard deviation of 10m.

Not only reprojection errors and their histogram, but also the confidence ellipses for all scenes can be given here. As shown at the left hand side of Figure 5.18, all the reprojection errors in row or column direction stay in the interval [-1.5 pixel, 1.5 pixel] after adjustment. According to the right figure it is easy to know that the main part of absolute reprojection

errors $(=\sqrt{(\Delta x)^2+(\Delta y)^2})$ is under 0.6 pixel. Figure 5.19 shows that RPC bias parameters of most of scenes have a 95% confidence error below 5m (Exceptions happen at the edge of large blocks because of bad image matching or covering the area of sea).

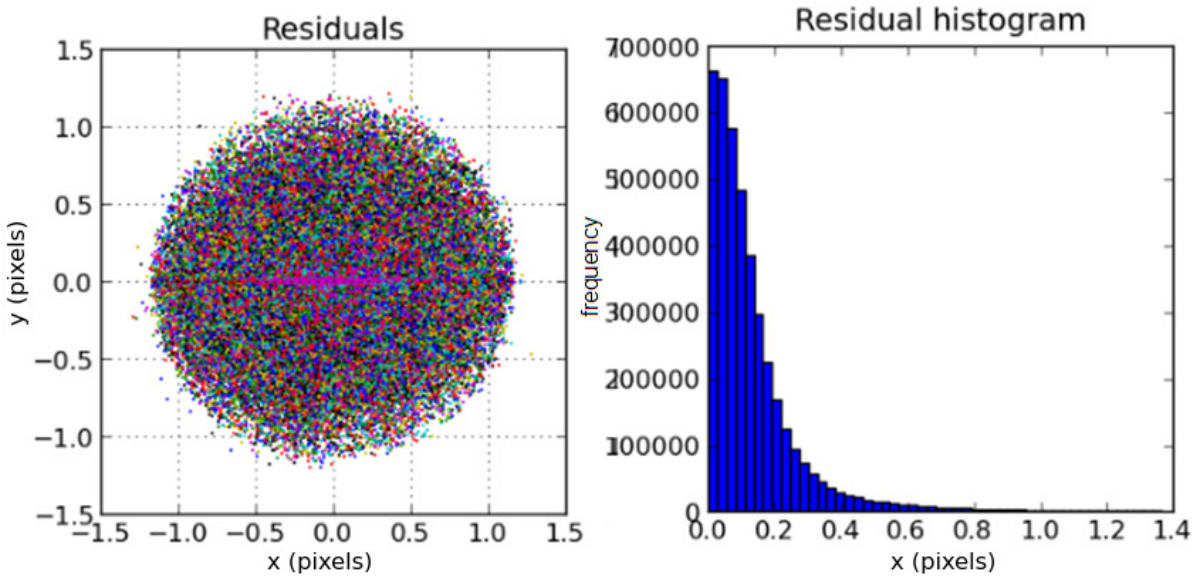

Figure 5.18: Reprojection errors after adjustment for all stereo pairs

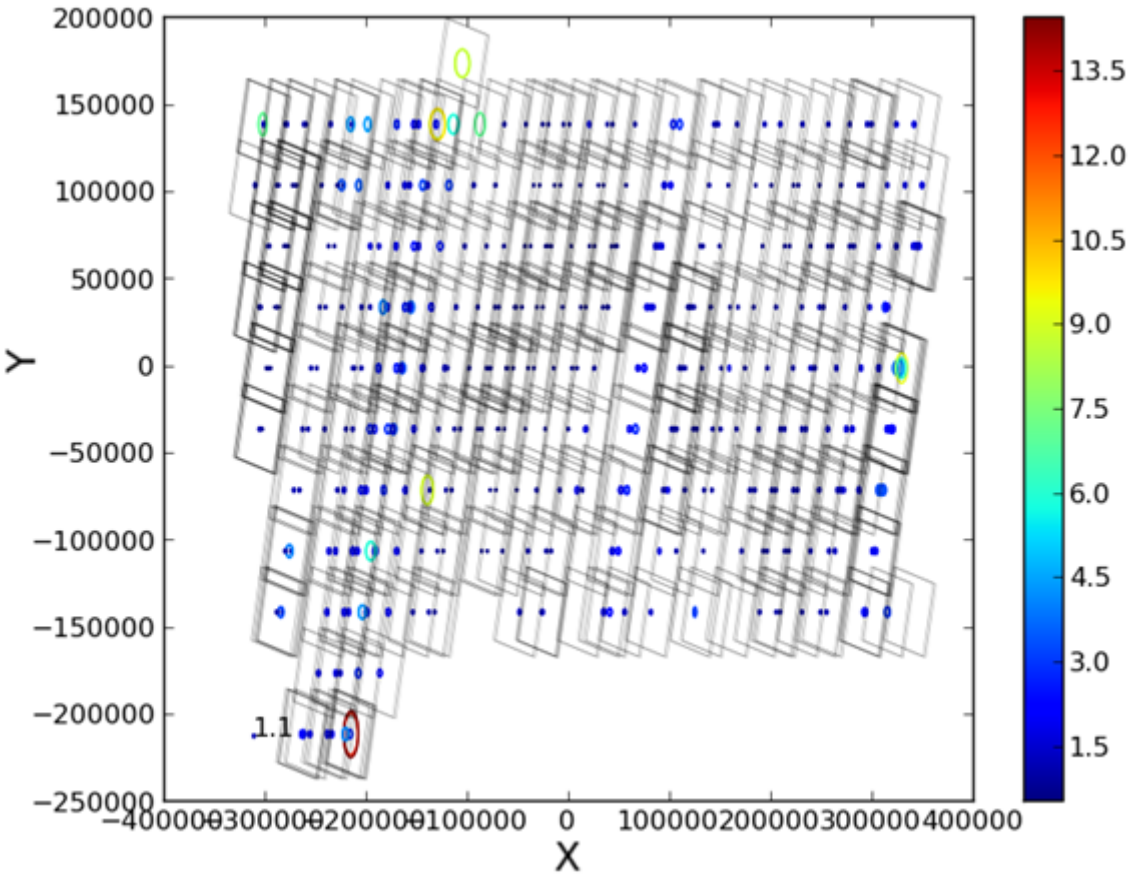

Figure 5.19: Confidence ellipses for all stereo pairs (unit of X-axis, Y-axis and color-bar: meter)

Finally, an evaluation against the adjustment model has to be made. According to the theory of quality control (see the appendix), the estimated standard deviation $\hat{\sigma}_0$ is a good indicator for the adjustment. $\hat{\sigma}_0$ should be as close as possible to the theoretical standard deviation σ_0 which is always set to 1. All the estimated standard deviations $\hat{\sigma}_0$ for the adjustment with 3 different numbers of images are calculated (see Table 5.3).

	Image Nr.	Estimated standard deviation $\hat{\sigma}_0$
Without DSM	1 stereo pair	1.70
	2 stereo pairs	1.82
With DSM	1 stereo pair	1.30
	2 stereo pairs	1.65
	All scenes	0.91

Table 5.3: Estimated standard deviations $\hat{\sigma}_0$

For the adjustment of 1 and 2 stereo pairs, only SIFT tie points are chosen. But for the situation of all scenes, both SIFT tie points and more accurate LSM tie points are used for the large block adjustment. Thus, large block adjustment of all scenes with DSM has the best estimated standard deviation $\hat{\sigma}_0$ after adjustment, which is already very close to the theoretical standard deviation $\sigma_0 = 1$.

5.3 Evaluation with check points (CPs)

In chapter 5.2 various results of 1-step block adjustment model have shown that after 1-step adjustment by adding ground control (DSM terms), the horizontal accuracies of tie points have improved much. In this chapter, check points are used to test the accuracy of RPC corrections. Since the horizontal accuracy of the Euro-Maps 2D is 15m (CE90, Circular Error of 90%), an accurate evaluation with checkpoints derived from Euro-Maps 2D is not possible. Aerial images are chosen as a better source of CPs.

Basing on the demonstration above, checkpoints are derived from two sources:

1) Euro-Maps 2D (horizontal coordinates, accuracy 15m (CE90) and SRTM DSM (height coordinates, accuracy 10m).

2) Aerial images with an accuracy of 2.5m (CE 95, for the whole Italy mosaic) and SRTM DSM (height coordinates, accuracy 10m).

5.3.1 Evaluation with CPs derived from Euro-map 2D

Along with check points given by Euro-Map and SRTM DSM, RPC affine corrections derived from results of 1-step block adjustment can be evaluated through the reprojection for stereo pairs. Stereo images A.183 and B.183 are chosen as the reference. In this stereo pair, 233 check points derived from Euro-Map and SRTM DSM are selected for the evaluation.

5.3.1.1 RPC corrections of 1 stereo pair 183

After the 1-step block adjustment in chapter 5.2.1, affine RPC corrections for the stereo pair 183 are obtained as follows (without DSM and with DSM):

A.183 (without DSM)	a_r [-]	a_c [-]	a_0 [pixel]
	0.999999	-0.000002	31.608053
	b_r [-]	b_c [-]	b_0 [pixel]
	-0.000065	0.999905	-22.280639
B.183 (without DSM)	a_r [-]	a_c [-]	a_0 [pixel]
	1.000001	0.000002	-29.726323
	b_r [-]	b_c [-]	b_0 [pixel]
	0.000021	1.000096	33.779156
A.183 (with DSM)	a_r [-]	a_c [-]	a_0 [pixel]
	1.000002	0.000156	55.447620
	b_r [-]	b_c [-]	b_0 [pixel]
	-0.000065	0.999908	58.882328
B.183 (with DSM)	a_r [-]	a_c [-]	a_0 [pixel]
	1.000003	-0.000205	63.757845
	b_r [-]	b_c [-]	b_0 [pixel]
	0.000020	1.000106	106.216732

Table 5.4: Affine RPC corrections of stereo pair 183 (derived from the block adjustment of a stereo pair)

Estimated standard deviations of affine RPC corrections for the stereo pair 183 are also obtained as follows (without DSM and with DSM):

A.183 (without DSM)	$\sigma(a_r)$ [-]	$\sigma(a_c)$ [-]	$\sigma(a_0)$ [pixel]
	1.697e-04	1.697e-04	3.371e+02
	$\sigma(b_r)$ [-]	$\sigma(b_c)$ [-]	$\sigma(b_0)$ [pixel]
	1.251e-04	1.217e-04	2.533e+02
B.183 (without DSM)	$\sigma(a_r)$ [-]	$\sigma(a_c)$ [-]	$\sigma(a_0)$ [pixel]
	1.697e-04	1.697e-04	3.372e+02
	$\sigma(b_r)$ [-]	$\sigma(b_c)$ [-]	$\sigma(b_0)$ [pixel]
	1.116e-04	1.218e-04	2.257e+02
A.183 (with DSM)	$\sigma(a_r)$ [-]	$\sigma(a_c)$ [-]	$\sigma(a_0)$ [pixel]
	9.350e-05	8.960e-05	1.787e+00
	$\sigma(b_r)$ [-]	$\sigma(b_c)$ [-]	$\sigma(b_0)$ [pixel]
	9.424e-05	9.052e-05	2.104e+00
B.183 (with DSM)	$\sigma(a_r)$ [-]	$\sigma(a_c)$ [-]	$\sigma(a_0)$ [pixel]
	9.377e-05	9.842e-05	1.866e+00

	$\sigma(b_r)$ [-]	$\sigma(b_c)$ [-]	$\sigma(b_0)$ [pixel]
	8.411e-05	9.053e-05	1.893e+00

Table 5.5: Estimated standard deviations of affine RPC corrections of stereo pair 183 (derived from the block adjustment of a stereo pair)

Obviously, the standard deviations of bias parameters are very large because the bias parameters contain major part of the attitude and ephemeris errors. After adding DSM terms into the adjustment model, the standard deviations of bias parameters $\sigma(a_0), \sigma(b_0)$ have come down significantly (from over 200 pixels to 2 pixels, see the green marks). However, they still have large uncertainty.

By using these affine RPC corrections, a new forward intersection into object-space can be made for the stereo check points. With obtained estimated 2D object coordinates, a comparison to the given 2D object coordinates of check points can be made (see Figure 5.20 and Figure 5.21). X-axis gives the East values, while Y-axis stands for the North values. Different scales are used for the plot and the color bars provide the numerical results.

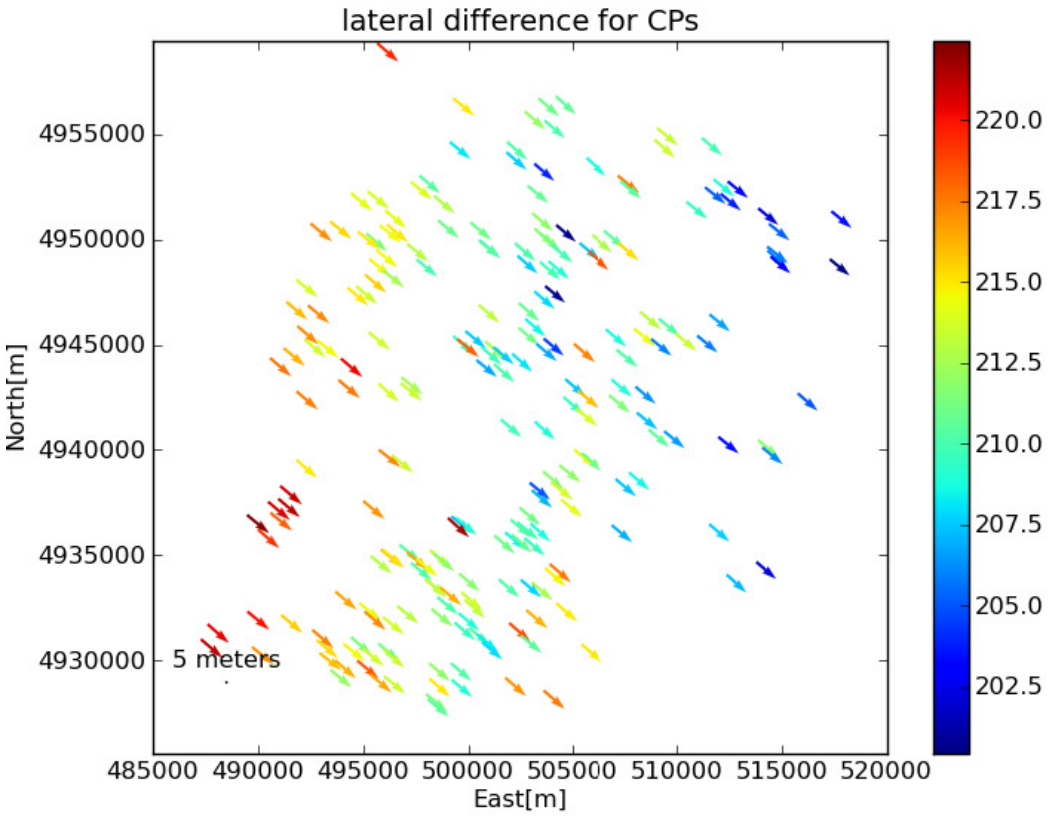

Figure 5.20: Horizontal errors for Euro-Maps 2D CPs of the stereo pair 183 (without DSM)

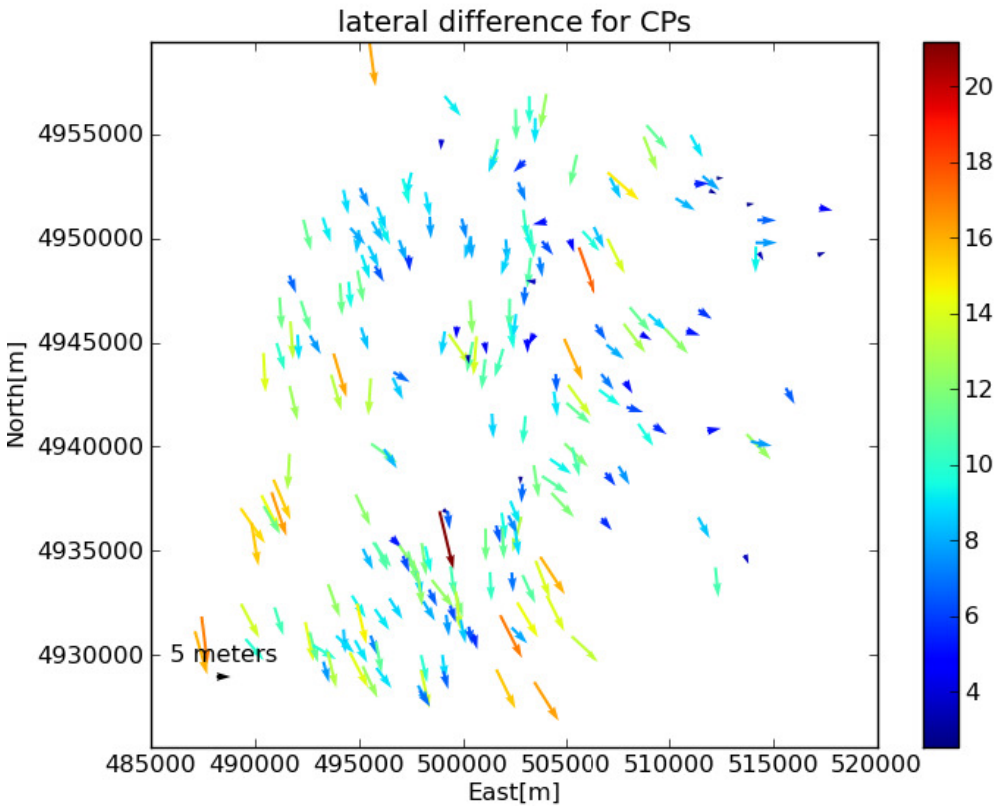

Figure 5.21: Horizontal errors for Euro-Maps 2D CPs of the stereo pair 183 (with DSM)

From the figure above it is obvious to see that the RPC corrections derived from 1-step block adjustment without ground control are very inaccurate and result in absolute horizontal differences $(=\sqrt{(\Delta X)^2+(\Delta Y)^2})$ which are over 200m. However, when the DSM terms are added into the adjustment, the absolute horizontal differences are greatly improved. Some important statistical characters of horizontal differences are given by following tables:

		mean	median	std	min	max
Without DSM	ΔX (East)	161.43	161.16	3.77	152.71	171.83
	ΔY (North)	-137.26	-137.27	3.75	127.80	149.49
With DSM	ΔX (East)	3.08	2.87	3.03	0.069	11.10
	ΔY (North)	-8.40	-8.46	3.76	0.030	20.59

Table 5.6: Statistical results of horizontal differences for stereo pair 183 (unit: meter)

According to the horizontal differences, the RMSE can also be calculated for these two cases: 211.91m (without DSM) and 9.6m (with DSM).

5.3.1.2 RPC corrections of 2 stereo pairs

Then the affine RPC corrections of stereo pair 183 derived from adjustment of two Cartosat-1 scenes (including 4 stereo images) are chosen to test the accuracy. Along with A.183 and B.183, an additional nearest neighbor scene A.229 and B.229 are selected here. After the 1-step block adjustment in chapter 5.2.2, affine RPC corrections for the stereo pair 183 are obtained (without DSM and with DSM, see Table 5.7):

A.183 (without DSM)	a_r [-]	a_c [-]	a_0 [pixel]
	1.000023	0.000040	-30.155005
	b_r [-]	b_c [-]	b_0 [pixel]
	-0.000048	0.999884	-25.936798
B.183 (without DSM)	a_r [-]	a_c [-]	a_0 [pixel]
	1.000028	0.000060	-44.722352
	b_r [-]	b_c [-]	b_0 [pixel]
	0.000017	1.000089	30.681159
A.183 (with DSM)	a_r [-]	a_c [-]	a_0 [pixel]
	0.999993	0.000155	54.447828
	b_r [-]	b_c [-]	b_0 [pixel]
	-0.000049	0.999892	59.672034
B.183 (with DSM)	a_r [-]	a_c [-]	a_0 [pixel]
	1.000057	-0.000103	61.838528
	b_r [-]	b_c [-]	b_0 [pixel]
	0.000015	1.000099	107.021502

Table 5.7: Affine RPC corrections of stereo pair 183 (derived from the block adjustment of 2 stereo pairs)

Estimated standard deviations of affine RPC corrections for the stereo pair 183 are also obtained (without DSM and with DSM, see Table 5.8):

A.183 (without DSM)	$\sigma(a_r)$ [-]	$\sigma(a_c)$ [-]	$\sigma(a_0)$ [pixel]
	1.287e-04	1.286e-04	2.547e+02
	$\sigma(b_r)$ [-]	$\sigma(b_c)$ [-]	$\sigma(b_0)$ [pixel]
	9.498e-05	9.222e-05	1.919e+02
B.183 (without DSM)	$\sigma(a_r)$ [-]	$\sigma(a_c)$ [-]	$\sigma(a_0)$ [pixel]
	1.286e-04	1.285e-04	2.546e+02
	$\sigma(b_r)$ [-]	$\sigma(b_c)$ [-]	$\sigma(b_0)$ [pixel]
	8.476e-05	9.261e-05	1.710e+02
A.183 (with DSM)	$\sigma(a_r)$ [-]	$\sigma(a_c)$ [-]	$\sigma(a_0)$ [pixel]
	8.602e-05	8.134e-05	1.791e+00
	$\sigma(b_r)$ [-]	$\sigma(b_c)$ [-]	$\sigma(b_0)$ [pixel]
	8.509e-05	8.168e-05	2.191e+00
B.183 (with DSM)	$\sigma(a_r)$ [-]	$\sigma(a_c)$ [-]	$\sigma(a_0)$ [pixel]
	8.526e-05	8.882e-05	1.836e+00
	$\sigma(b_r)$ [-]	$\sigma(b_c)$ [-]	$\sigma(b_0)$ [pixel]
	7.594e-05	8.168e-05	1.968e+00

Table 5.8: Estimated standard deviations of affine RPC corrections of stereo pair 183 (derived from the block adjustment of 2 stereo pairs)

Similar to the case of 1 stereo pair, the standard deviations of bias parameters are large, too. In addition, after adding DSM terms into the adjustment model, the standard deviations of bias parameters have improved from several hundred pixels to nearly 2 pixels (see the green marks).

As before, a new forward intersection into object-space can also be made for the check points according to their given image coordinates. With obtained estimated 2D object coordinates, a comparison to the given 2D object coordinates of check points can be made, as shown in Figure 5.22 and Figure 5.23:

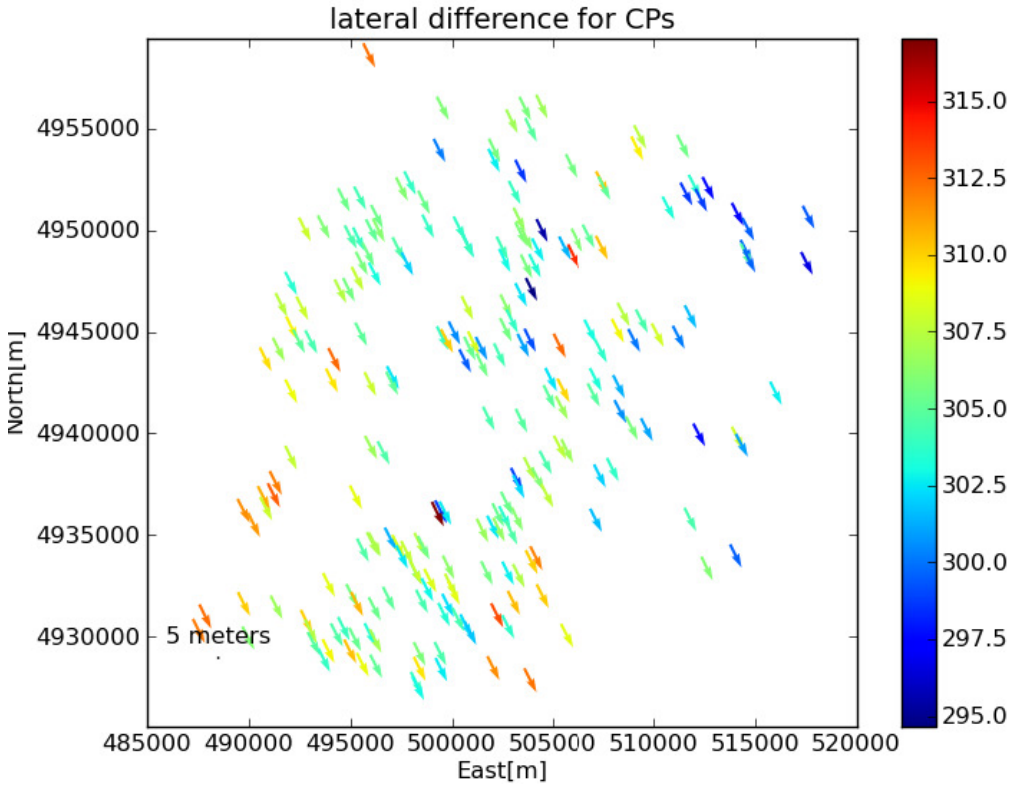

Figure 5.22: Horizontal errors for Euro-Maps 2D CPs of the stereo pair 183 (without DSM)

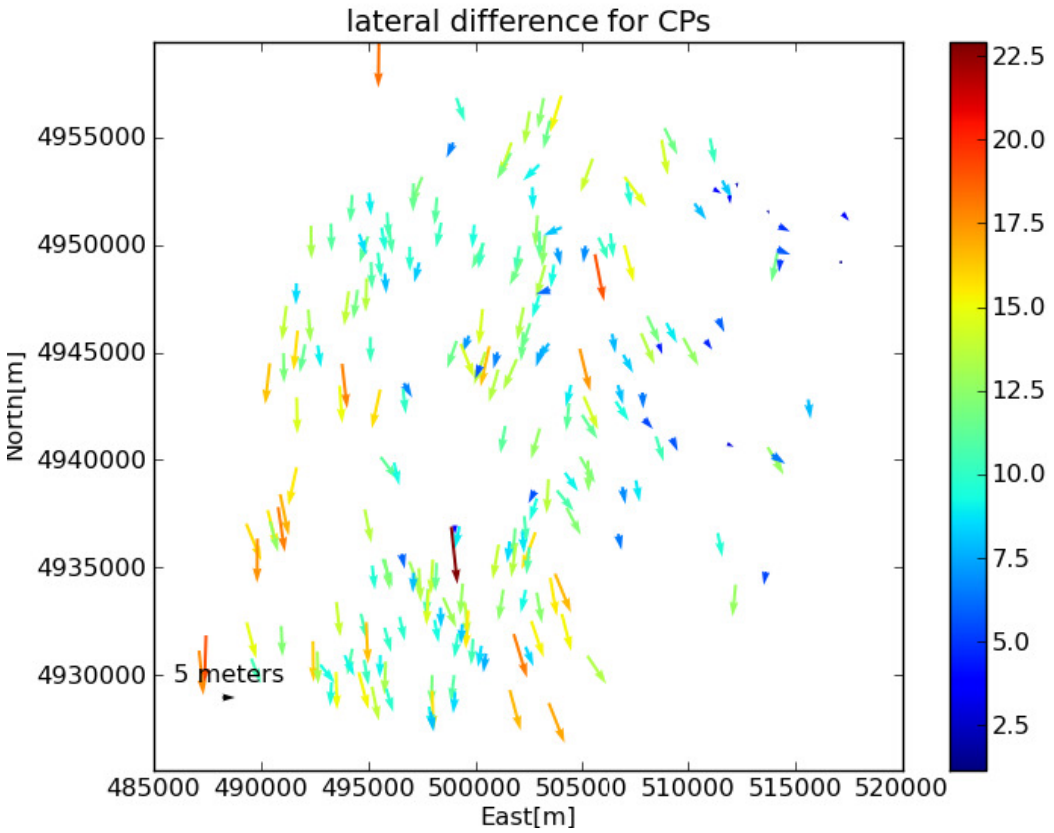

Figure 5.23: Horizontal errors for Euro-Maps 2D CPs of the stereo pair 183 (with DSM)

From the figure above it is obvious to see that the RPC corrections derived from 1-step block adjustment without ground control are very inaccurate and result in absolute horizontal differences $(=\sqrt{(\Delta X)^2+(\Delta Y)^2})$ which are over 295m. However, when the DSM terms are added into the adjustment, the absolute horizontal differences reduce sharply to below 23m, which is similar to the situation of 1 stereo pair. Some important statistical characters of horizontal differences are given (see Table 5.9).

		mean	median	std	min	max
Without DSM	ΔX (East)	135.79	135.93	2.99	127.63	143.35
	ΔY (North)	-273.50	-273.58	3.60	264.65	285.57
With DSM	ΔX (East)	0.63	0.39	3.03	0.017	8.77
	ΔY (North)	-10.60	-10.69	3.79	0.90	22.78

Table 5.9: Statistical results of horizontal differences for stereo pair 183 (unit: meter)

According to the horizontal differences the value of RMSE can also be calculated for these two cases: 305.37m (without DSM) and 11.10m (with DSM).

Clearly, the horizontal differences after adjustment shown in Figure 5.21 and Figure 5.23 are not accurate enough because the horizontal accuracy of Euro-Maps 2D checkpoints is circa 15m (CE90).

5.3.1.3 RPC corrections of all stereo pairs

Finally the affine RPC corrections of all stereo pairs derived from adjustment of all Cartosat-1 scenes (over 800 images) are chosen to test the accuracy. Affine RPC corrections and estimated standard deviations of them for the stereo pair 183 are calculated as before (see Table 5.10 and Table 5.11).

A.183	a_r [-]	a_c [-]	a_0 [pixel]
	1.000034	-0.000399	60.652351
	b_r [-]	b_c [-]	b_0 [pixel]
	-0.000050	1.000045	59.098650
B.183	a_r [-]	a_c [-]	a_0 [pixel]
	1.000034	-0.000742	68.863618
	b_r [-]	b_c [-]	b_0 [pixel]
	0.000019	1.000250	106.395127

Table 5.10: Affine RPC corrections of stereo pair 183 (derived from the block adjustment of all stereo pairs)

A.183	$\sigma(a_r)$ [-]	$\sigma(a_c)$ [-]	$\sigma(a_0)$ [pixel]
	9.485e-07	7.541e-07	0.016
	$\sigma(b_r)$ [-]	$\sigma(b_c)$ [-]	$\sigma(b_0)$ [pixel]
	8.222e-07	6.596e-07	0.016
B.183	$\sigma(a_r)$ [-]	$\sigma(a_c)$ [-]	$\sigma(a_0)$ [pixel]
	8.975e-07	8.846e-07	0.016
	$\sigma(b_r)$ [-]	$\sigma(b_c)$ [-]	$\sigma(b_0)$ [pixel]
	6.543e-07	6.516e-07	0.012

Table 5.11: Estimated standard deviations of affine RPC corrections of stereo pair 183 (derived from the block adjustment of all stereo pairs)

Compared to the results derived from the block adjustment of single or 2 stereo pairs, standard deviations of affine RPC corrections derived from the block adjustment of all stereo pairs are much smaller: about 0.016 pixel or even less. This satisfied result presents an obvious advantage of large block adjustment on single stereo pair: much larger redundancy than single stereo pair adjustment, which leads to a better improvement of uncertainty.

A new forward intersection into object-space can also be made for the check points as before. Obtained estimated 2D object coordinates are compared to the given 2D object coordinates of check points. Horizontal position errors of check points for stereo pair 183 are calculated and RMSE of check points for all stereo pairs are plotted as well (see Figure 5.24 and Figure 5.25).

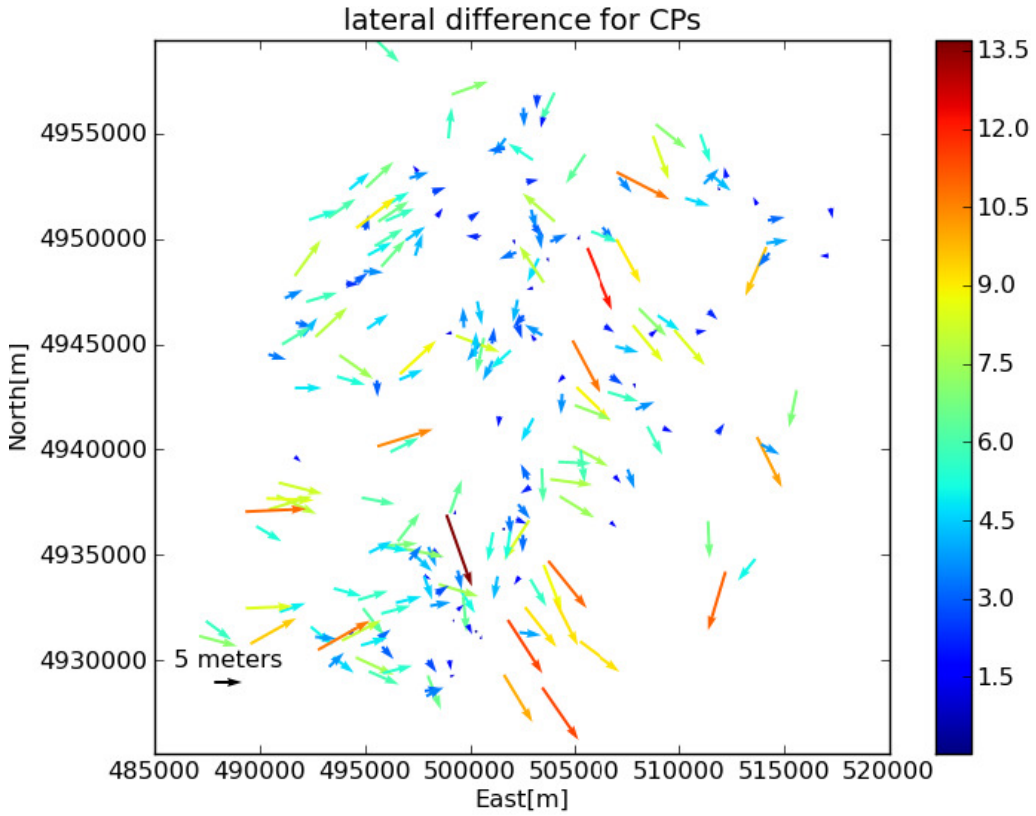

Figure 5.24: Horizontal errors for Euro-Maps 2D CPs of the stereo pair 183

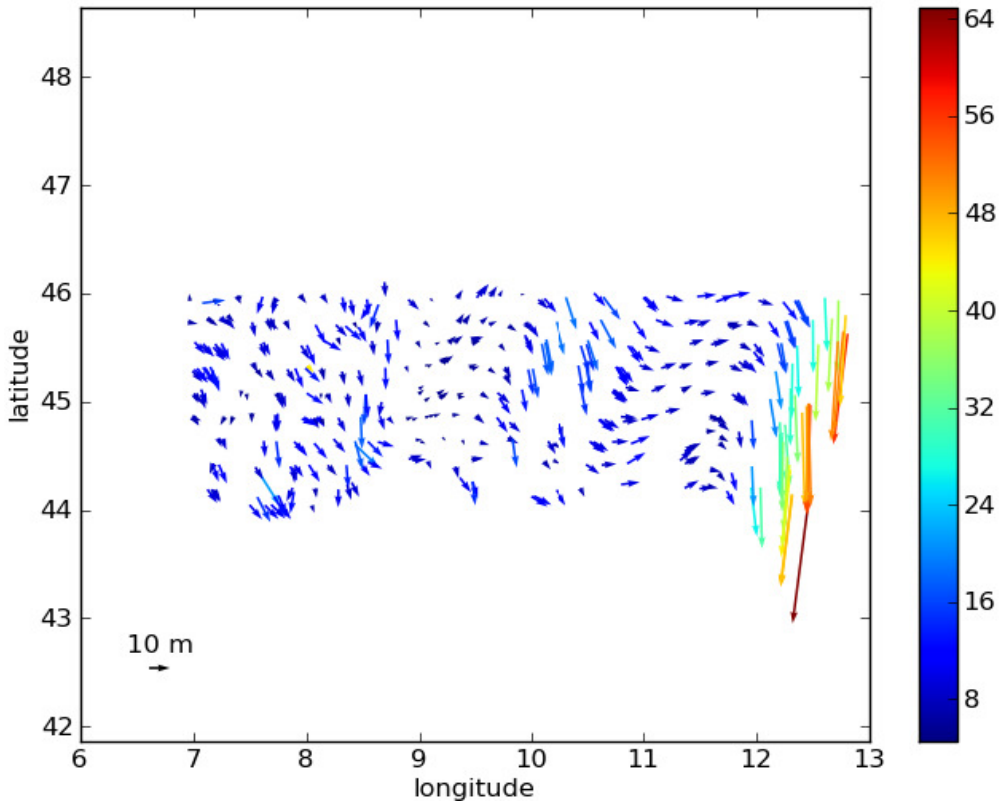

Figure 5.25: Mean horizontal errors for Euro-Maps 2D CPs of all stereo pairs (Each arrow shows the RMSE of the CP errors in a scene, unit of color-bar: meter)

Apparently, all horizontal errors for Euro-Maps 2D CPs of stereo pair 183 stay below 13.5m and are better than the results derived from adjustment of 1 or 2 stereo pairs (maximal values are 20m and 22.5m, respectively). A possible reason is that not only SIFT tie points but also more accurate LSM tie points are applied for the large block adjustment. Moreover, as shown in Figure 5.25, most of stereo pairs have a RMSE which is smaller than 16m after large block adjustment (even for the large flat areas in the middle of this large bolck). However, some scenes at the right hand side (see the green and red arrows) which have the latitude larger than 12 degrees present relatively large RMSE (even over 60m). That's because the DSM constraint data only occupy a part instead of the whole image in these flat areas (the rest part of these areas are covered by sea without DSM constraint). What's more, there are not enough hilly areas nearby for correcting these large RMSE.

5.3.2 Evaluation with CPs derived from aerial images

Compared to given checkpoints from Euro-Maps 2D, aerial images have a higher horizontal accuracy (2.5m, CE95) and can be chosen as an ideal source of check points. 16 test areas including mountainous and flat areas are selected. These areas are marked by red rectangles (see Figure 5.26) and check points derived from aerial images in these areas are marked by green color (see Figure 5.27).

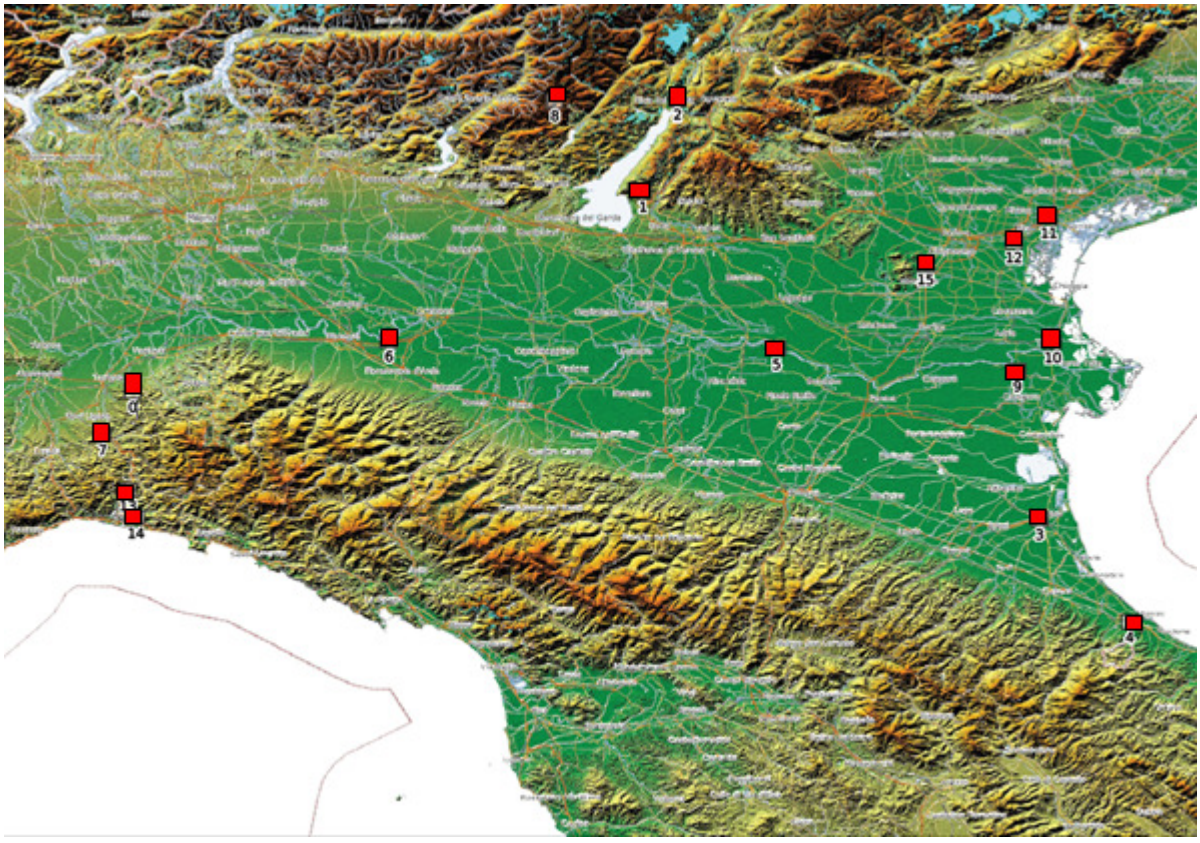

Figure 5.26: Overview of test areas for which aerial reference images are available

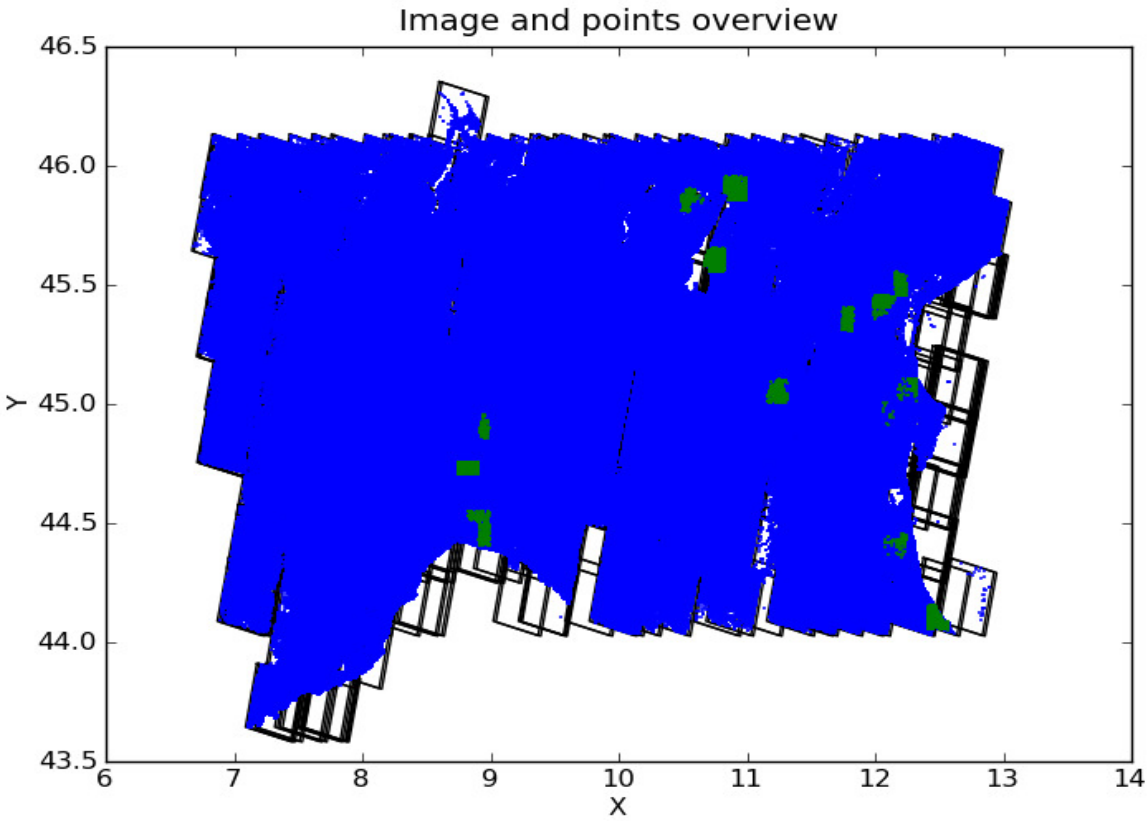

Figure 5.27: Scenes and points overview (X-axis: longitude, Y-axis: latitude, unit: degree)

These test areas will be used to evaluate the absolute accuracy of the adjustment. Along with different kinds of tie points, check points derived from aerial images are used to evaluate the adjustment results.

5.3.2.1 Influence of the number of tie points on single stereo pair RPC corrections

For every test area, two main kinds of tie points are provided for the block adjustment: tie points derived from SIFT image matching and from LSM image matching. Using corrected RPC affine parameters derived from 1-step adjustment of single stereo pair, it is able to evaluate the results.

As the DSM alignment depends on well distributed points at various slopes and aspects, a large number of tie points is required. By varying the number of used tie points, the relationship between the number of tie points and the accuracy and stability of the block adjustment is evaluated. Different numbers of SIFT tie points are derived from image matching by thinning with a grid. Only a single tie point is selected from each grid cell.

The mountainous test area 7 including the image pair 183 is evaluated at first. Here, 5 sizes are selected for the generation of SIFT tie points (see Table 5.12).

Image Nr.	Grid cell width/height (unit: pixel)				
	50	100	500	1000	2000
183	10087	6003	563	144	36
2	8773	5436	530	142	36
202	9347	5965	566	144	36
229	10596	6247	558	144	36
251	13949	7993	564	144	36
402	8564	5458	562	143	36
41	11172	7090	575	144	36
91	11289	7307	576	144	36

Table 5.12: The number of SIFT tie points for test area 7

Tie points derived from the LSM image matching are also used for these test areas. Different numbers of LSM tie points are derived from image matching under the constraint of the grid with different sizes. Here, 6 sizes are selected for the generation of LSM tie points. Additionally, LSM tie points that are generated without constraint of the grid are considered (see Table 5.13).

Image No.	Grid cell width/height (unit: pixel)						
	no grid	50	100	200	500	1000	2000
183	-	28224	9974	3072	551	142	36
2	193860	39322	12221	3275	550	140	36
202	136477	31700	11479	3378	573	144	36
229	170160	32231	10689	3097	539	140	35
251	135078	33070	12103	3437	571	144	36
402	-	28117	10940	3429	575	144	36
41	111448	28095	10903	3346	568	143	36
91	208947	42254	13269	3521	576	144	36

Table 5.13: The number of LSM tie points for test area 7

The results of RMSE for the mountainous test area 7 are given for both SIFT tie points and LSM tie points (see Figure 5.28 and Figure 5.29).

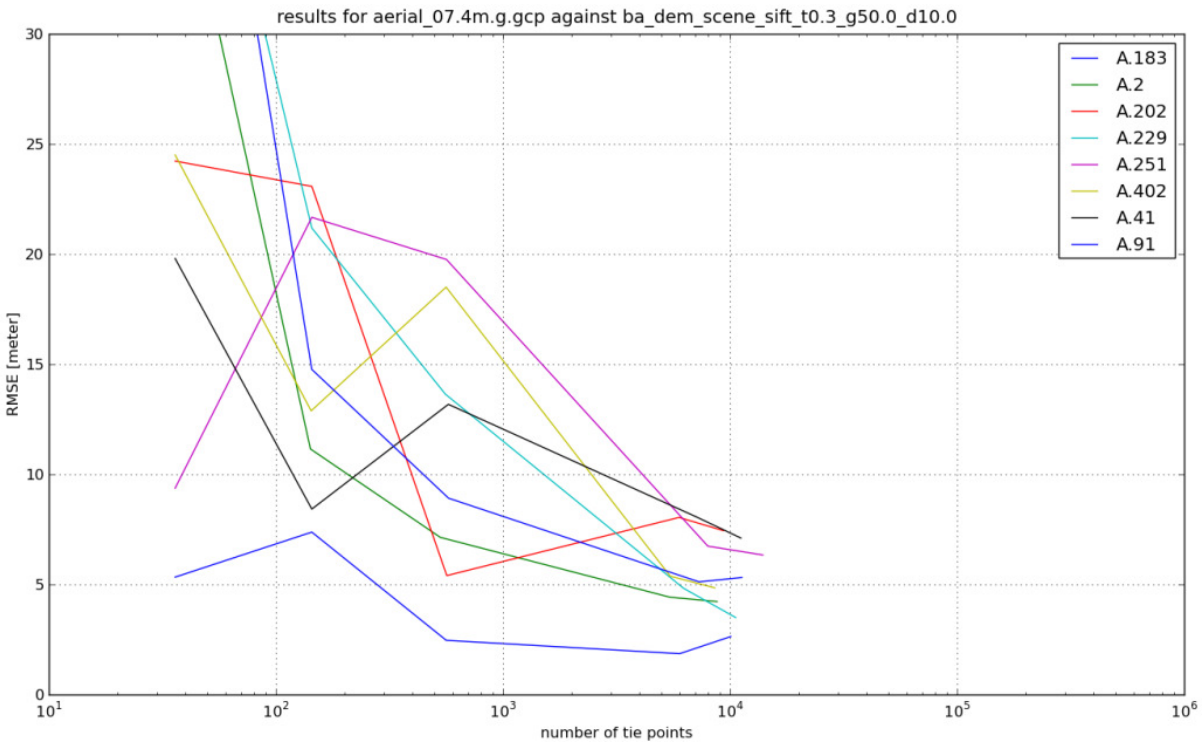

Figure 5.28: Results of RMSE for test area 7 (using SIFT tie points)

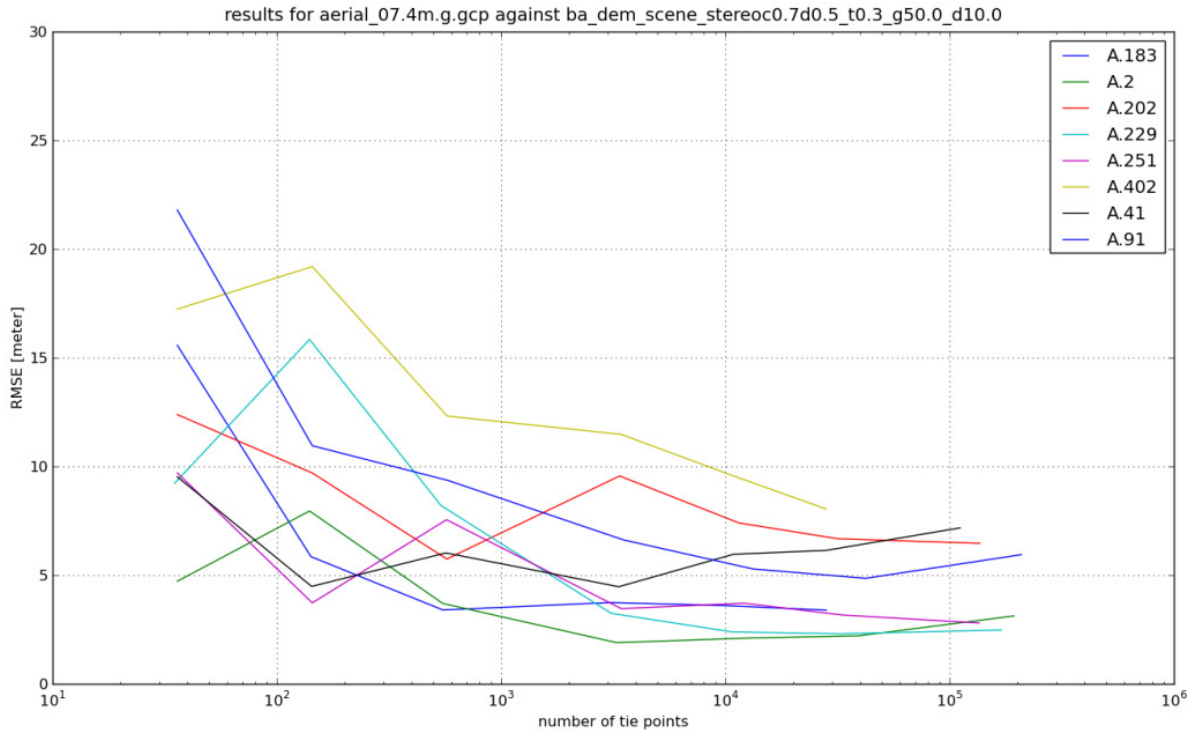

Figure 5.29: Results of RMSE for test area 7 (using LSM tie points)

For the stereo pair adjustment by using SIFT tie points, following assumptions about the priori information are given. Tie points have a priori standard deviation of 0.3 pixel; GCPs of landsat image have a priori standard deviation of 50m and SRTM DSM has a priori standard deviation of 10m. For the stereo pair adjustment by using LSM tie points, tie points, GCPs of

landsat image and SRTM DSM have the same priori deviations as before. In addition, the threshold value of correlation coefficient for LSM image matching is 0.7 and the threshold value for a bidirectional matching check is 0.5 pixel.

As Figure 5.28 and Figure 5.29 show, 8 image pairs in test area 7 are evaluated. X-axis gives the number of tie points. Y-axis presents the results of horizontal RMSE (root mean square deviation). It is expected that as the number of tie points increases, the RMSE should reduce. Apparently, not all the image pairs present exactly such a trend. However, it is still clear to observe that if the number of tie points is larger than 1000, the RMSE for each stereo pair are all under 15m (SIFT) or 20m (LSM). When the number reaches 10000, all RMSE are all below 10m for both SIFT and LSM tie points.

Like chapter 5.3.1, the horizontal errors of CPs are plotted. As before, the stereo pair 183 is chosen for the evaluation. Here tie points limited with 50-pixel grid are selected. Obviously, with more than 10000 SIFT tie points, the maximal value of absolute horizontal differences decreases below 4m. This result is a little better than the LSM tie points whose maximal absolute horizontal differences sink below 5m (As shown in Figure 5.30 and Figure 5.31). In fact, these results are much better than the result by using Euro-map 2D CPs, because here more accurate tie points (over 10000) are generated for the adjustment.

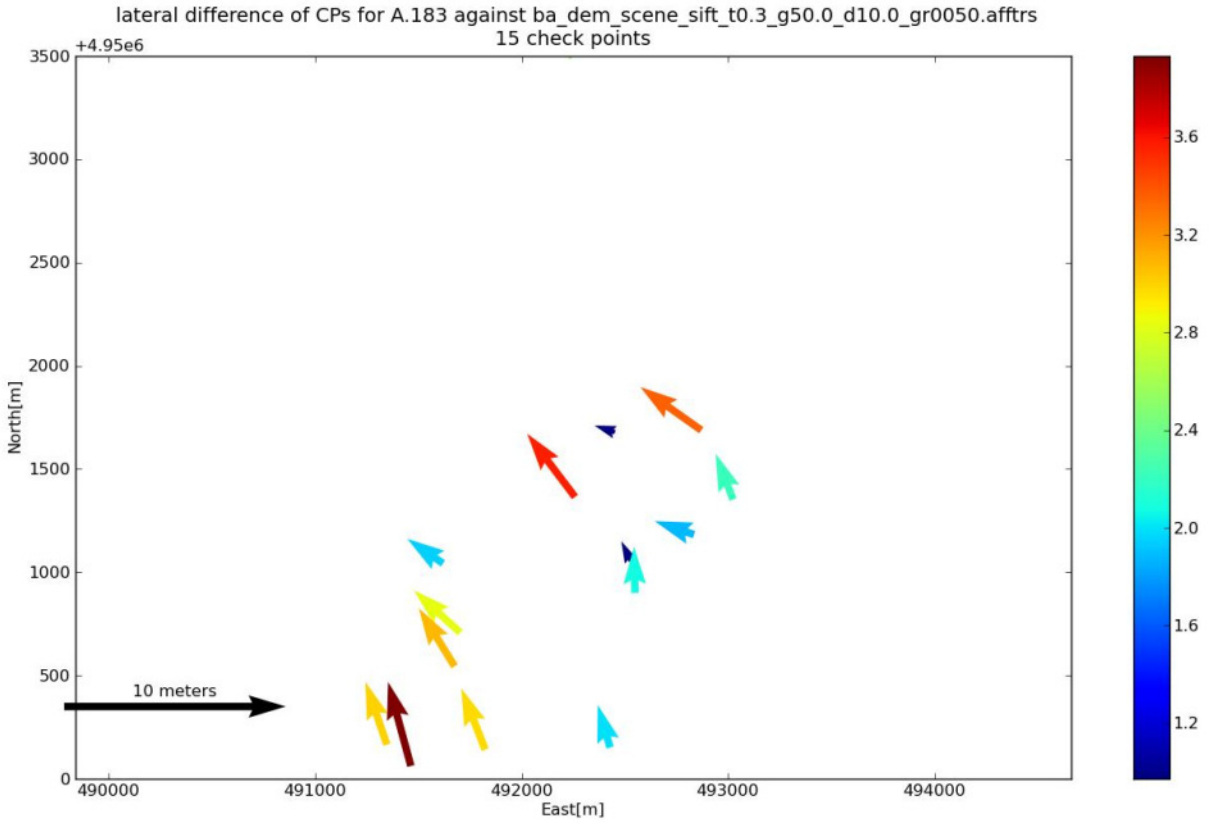

Figure 5.30: Horizontal errors of aerial image CPs for stereo pair 183 (10087 SIFT tie points)

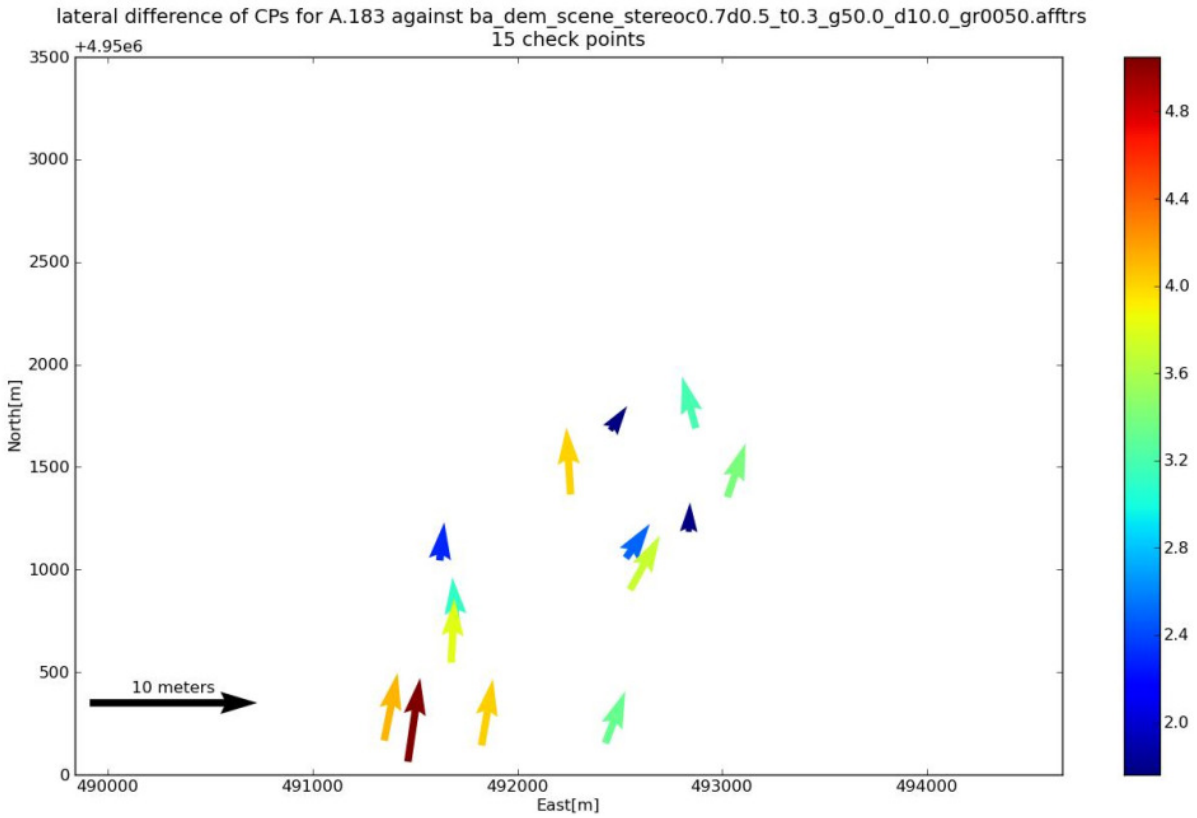

Figure 5.31: Horizontal errors of aerial image CPs for stereo pair 187 (28224 LSM tie points)

Then some other mountainous test areas (1 and 2) are observed, too. The RMSE for these two test areas are shown (see Figure 5.32 - Figure 5.35)

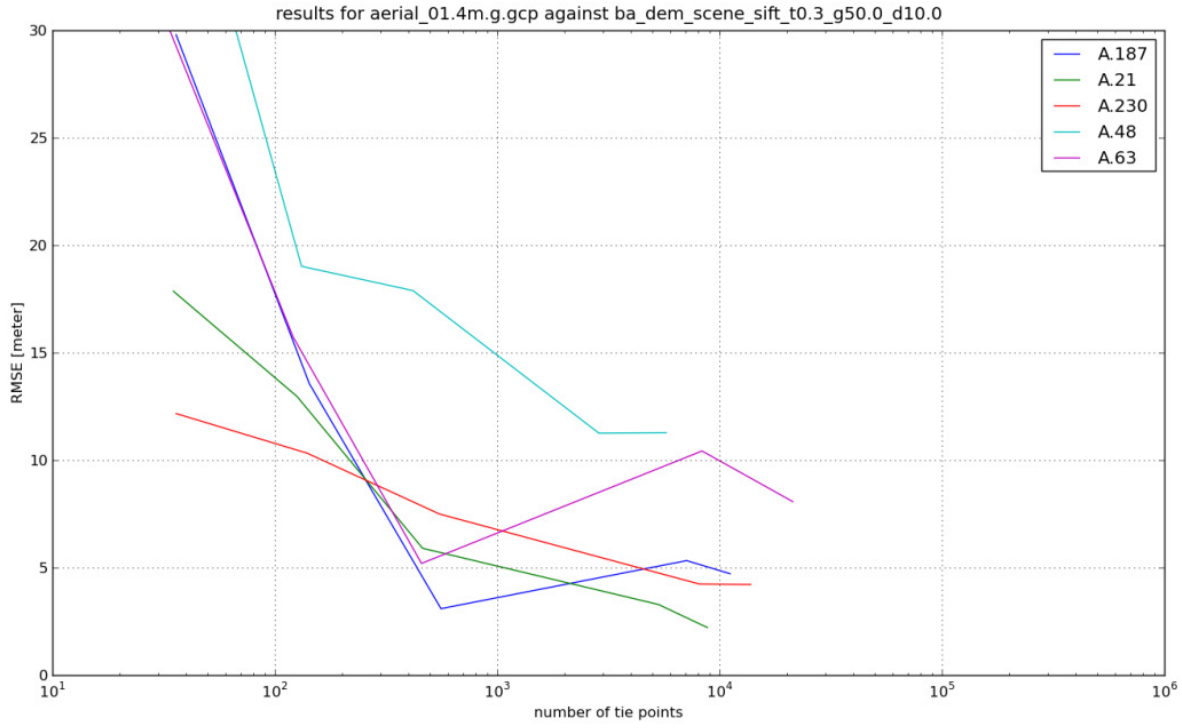

Figure 5.32: Results of RMSE for test area 1 (using SIFT tie points)

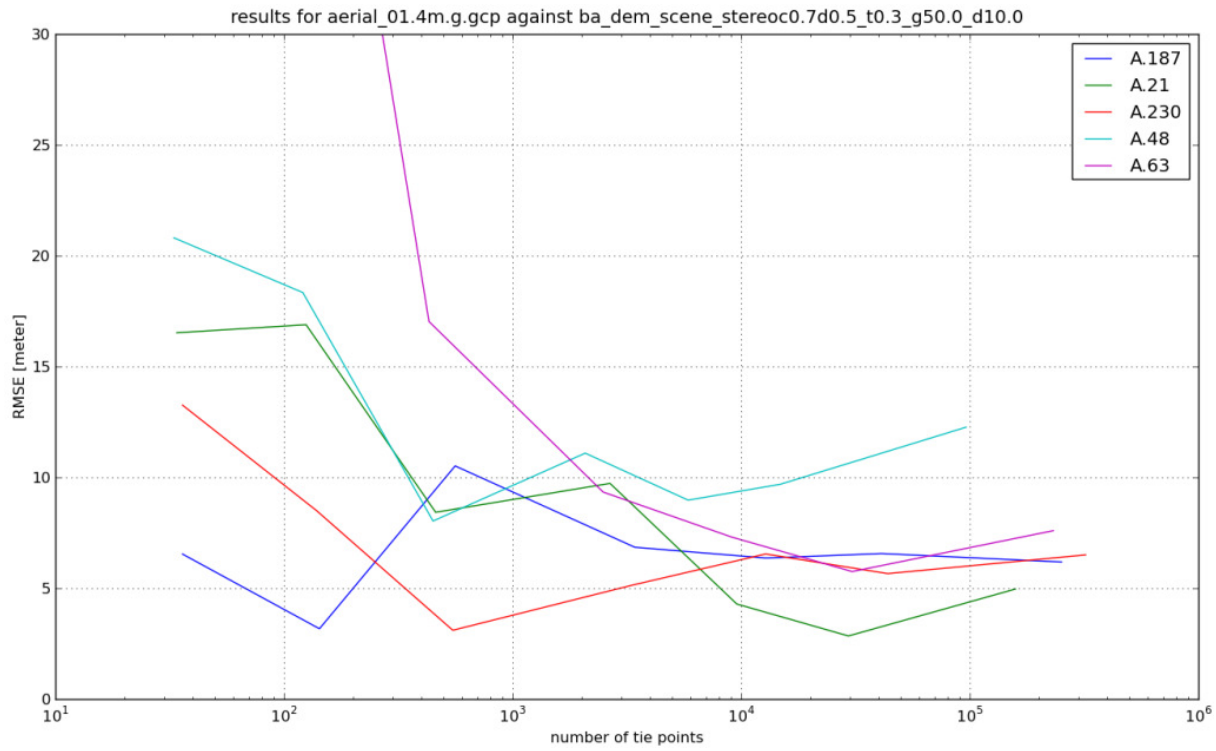

Figure 5.33: Results of RMSE for test area 1 (using LSM tie points)

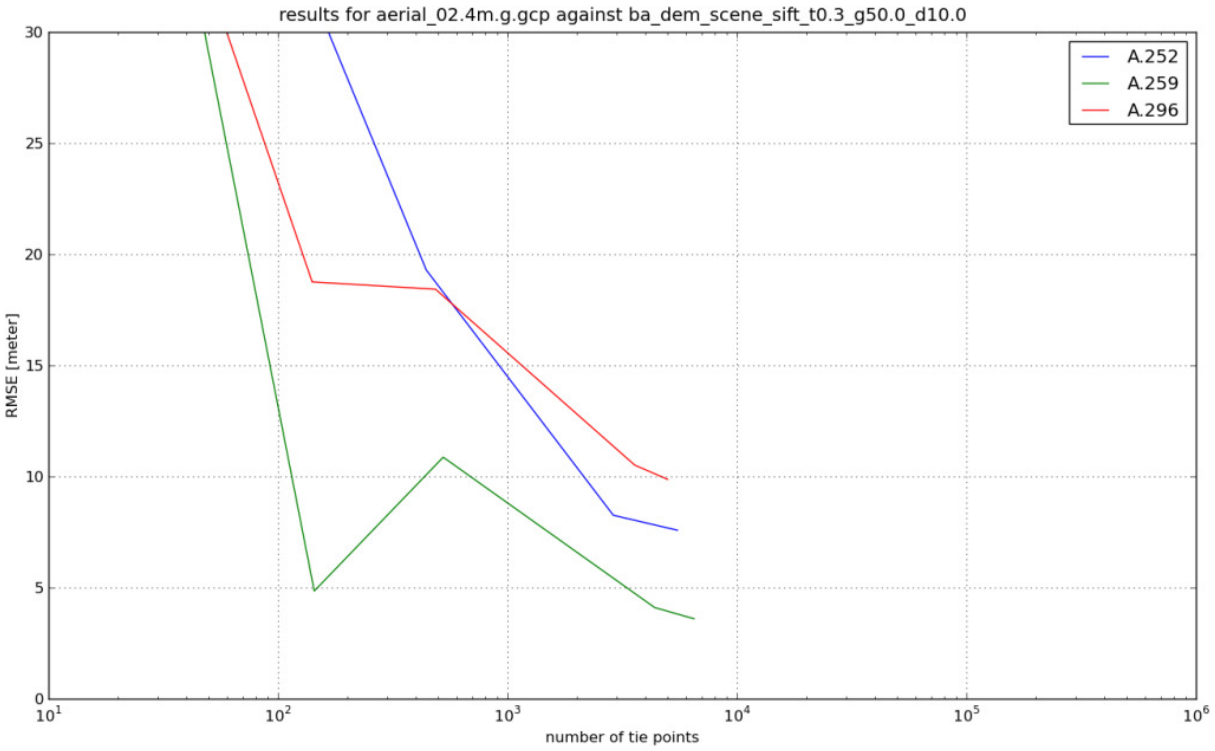

Figure 5.34: Results of RMSE for test area 2 (using SIFT tie points)

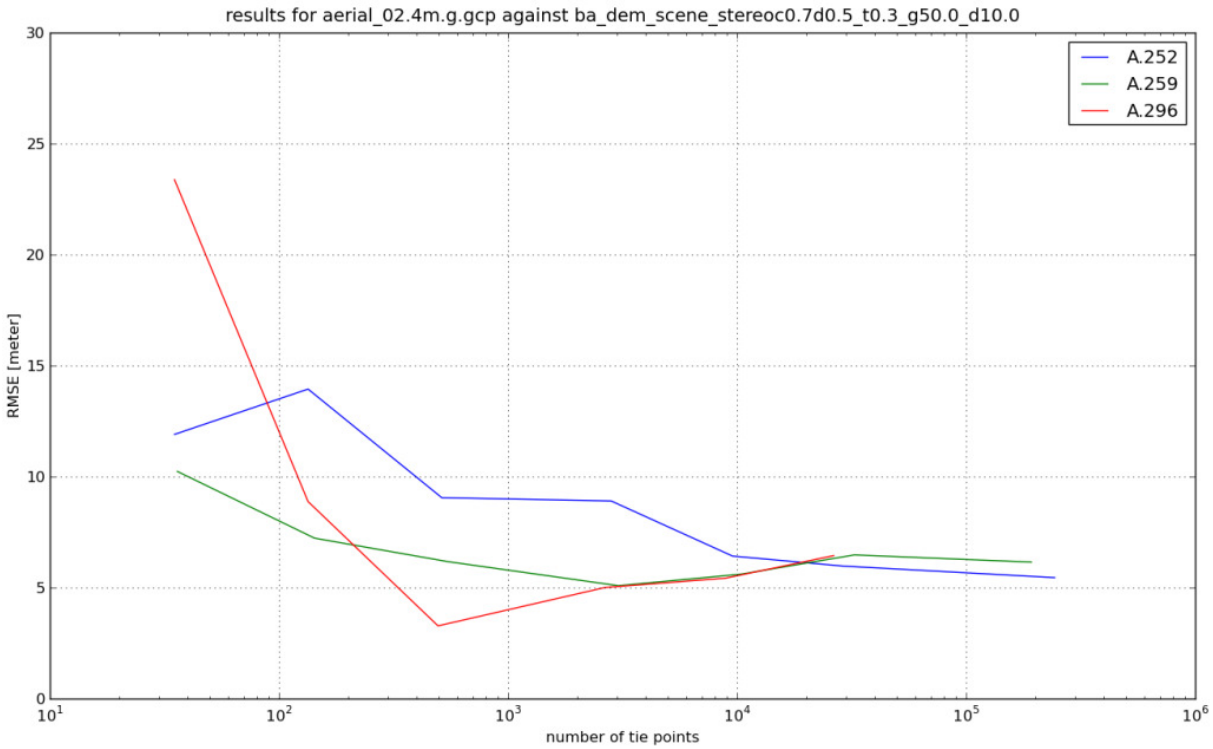

Figure 5.35: Results of RMSE for test area 2 (using LSM tie points)

As the 4 figures above show, 5 stereo pairs in test area 1 are evaluated, while 3 stereo pairs in test area 2 are selected to test the quality of results. Clearly, if the number of tie points reaches nearly 1000, the RMSE for test area 1 can reduce below 15m. When the number of tie points increases until over 1000, the RMSE for each image in test area 2 all decrease under 10 meters (image pair 296 by using SIFT tie points is probably an exception).

The tables which give the number of tie points for these test areas (1 and 2) and the figures that plot horizontal errors of CPs for single stereo pair can be found in the appendix.

According to all of the above, although there are still some variations for the RMSE values, the main trend can be determined: As the number of tie points (from SIFT and LSM matching) increases, most of the RMSE values of check points derived from aerial images sink obviously. If the number of tie points is over 10000, RMSE values will even reduce below 10m. What's more, the RMSE by using LSM tie points are smaller than that by using SIFT tie points if the number of tie points reaches 1000 or even 10000. In addition, by using adjusted affine RPC corrections, CPs derived from aerial images have obviously smaller horizontal differences than Euro-Map CPs (image pair 183 is a good example for that). The variation of some curves can be explained by bad stereo image matching in certain areas. Another important reason is that the SRTM Data (90m grid) have a low resolution, which influences the results of height difference and degreesient in the functional adjustment model.

5.3.2.2 Evaluation of all test stereo pairs

In this chapter, the situation for all stereo pairs is considered. Using corrected RPC affine parameters derived from 1-step adjustment of all test stereo pairs, it is able to evaluate the results.

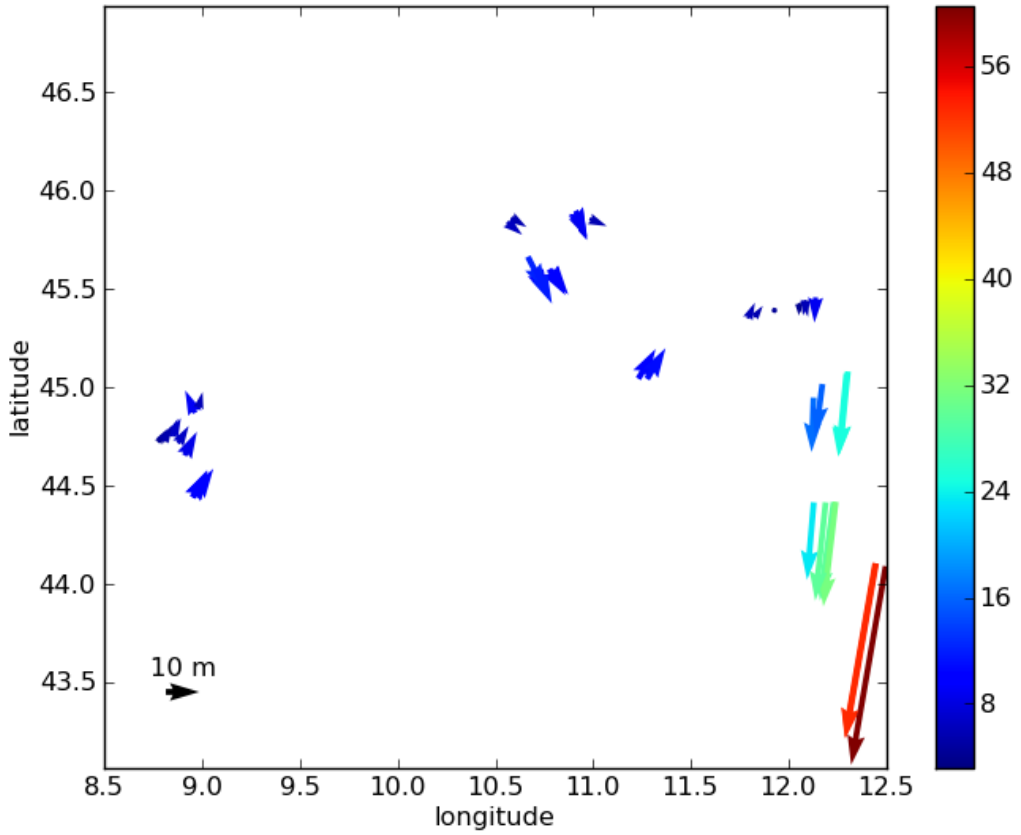

Figure 5.36: Mean horizontal errors for aerial image CPs of all test areas (Each arrow shows the RMSE of the CP errors in a scene, unit of color-bar: meter)

Similar to Figure 5.25, considering all the test areas, the RMSE of the CP errors in each test scene are plotted. Most of stereo pairs have a RMSE which is smaller than 16m or even below 8m (see the blue arrows). However, some scenes at the right hand side (see the green and red arrows) present large RMSE which is even over 56m. In fact, these areas are exactly the east edge of the large block and cover the flat regions and even the sea so that the DSM constraint functions not well in these areas. In addition, there are not enough other stereo pairs which cover mountainous areas nearby. Thus, for the purpose of improving large RMSE in these areas, a few high accurate GCPs are demanded in the future.

In order to observe the results of test areas clearly, the RMSE of all scenes in horizontal directions (East and North) and heights are calculated as follows:

Image No.	Easting [m]	Northing [m]	Height [m]
A.123	9.26	52.33	2.38
A.251	2.64	4.24	3.61
A.255	4.71	3.36	3.5
A.139	5.33	8.97	3.66
A.330	1.58	8.65	4.68
A.93	4	8.84	5.68
A.356	3.07	4.59	2.23
A.397	0.22	3.15	3.07

A.1	10.49	59.59	3.07
A.36	6.14	6.8	5.77
A.145	2.65	24.86	2.23
A.365	2.05	3.8	1.9
A.409	4.16	29.44	4.44
A.401	4.78	4.1	2.95
A.204	1.56	5.8	2.56
A.205	0.69	16.36	1.51
A.373	1.61	3.57	2.31
A.370	2.38	5.36	2.18
A.21	4.81	9.01	2.66
A.187	5.54	7.53	3.41
A.296	3.8	7.83	6.2
A.47	4.97	8.4	8.4
A.202	3.26	5.92	4.47
A.259	3.71	8.26	5.7
A.2	2.18	3.61	3.34
A.156	3.76	31.26	1.99
A.120	4.65	8.93	7.97
A.70	3.35	4.99	2.53
A.91	2.67	4.68	3.51
A.41	3.45	5.71	3.75
A.183	3.92	7.33	4.84
A.237	2.61	24.89	2.17
A.402	2.66	4.95	3.51
A.171	2.67	5.22	1.67
A.65	2.85	15.65	1.67
A.229	3.33	5.66	4.84
A.192	5.51	8.62	7.3
A.48	5.68	10.88	3.97
A.230	5.14	7.98	3.52
A.371	2.45	23.2	2.62
A.63	5.08	10.54	3.36
A.116	5.64	9.28	2.51
A.153	1.25	3.87	2.44
A.334	3.25	29.49	2.85
A.252	5.19	2.56	3.93
A.239	9.21	52.04	3.84

Table 5.14: RMSE for aerial image 3D CPs of all test areas

From Table 5.14 it is obvious to find out that large RMSE in Easting and Northing usually appear together (see the red marks). The largest value in Easting can reach 10m, while in Northing this value can even reach 60m. The possible reason is that the corresponding stereo image pairs (123, 1, 239) all cover the flat areas or even sea areas. The largest RMSE in elevations is almost 8 meters and most of scenes have a RMSE in heights below 5 meters.

5.3.3 Comparison with other results

By Indian Space Research organization, evaluations of Cartosat-1 data are handled, too. DGPS measurements are used for collecting 27 and 13 high accurate GCPs for hilly areas Dehradun and Shimla regions respectively. Among them, 20 and 10 points are chosen as control points respectively for these two regions. These control points are used for the updating of RPC parameters. Then the corrected RPC parameters are applied for generating DEM and ortho image. Finally, the planimetry from the ortho image and elevation values at all check points (10 for Dehradun and 3 for Shimba sites) are compared to the DGPS measured values. [Ahmed 2007] The RMSE in horizontal directions and elevations are shown in Table 5.15.

	Easting [m]	Northing [m]	Height [m]
Dehradun	1.86	1.81	4.38
Shimla	3.02	2.36	3.69

Table 5.15: RMSE of 3D check points for Dehradun and Shimla [Ahmed 2007]

The Institute of Geodesy and Photogrammetry (IGP) in ETH Zurich is also participating in the Cartosat-1 evaluation program. Within this program, various test sites with reference data have been established and Cartosat-1 images have been acquired over these sites. Catalonia test sites of ISRO and test site in Sakurajima (Japan) are evaluated. After adding a few GCPs, an affine RPC adjustment is processed. The results were checked and were compared using the provided reference data: Catalonia DTM (grid spacing: 15m, accuracy: 1.1m, height range: 0m-970m) and Sakurajima DSM (grid spacing: 5m, height range: 300m-1100m). The RMSE in horizontal directions and elevations are shown in Table 5.16 (* GCPs well-distributed over the images, ** GCPs cover approximately 1/4th of the image area).

	GCP No.	Easting [m]	Northing [m]	Height [m]
Catalonia	All (70)	0.94	1.31	1.26
	6 *	0.98	1.43	1.49
	6 **	1.23	2.02	1.6
Sakurajima	All (61)	1.43	1.31	1.42
	6 *	1.64	1.55	1.77
	6 **	2.73	2.5	2.1

Table 5.16: 3D RMSE for Catalonia and Sakurajima [Kocaman 2008]

Apparently, the results of ISRO and ETH Zurich have the accuracy below 2 pixels or even sub-pixel due to the accurate reference data.

Compared to the results of ISRO and ETH Zurich, most of scenes in the test areas have a comparable accuracy, especially in Easting and in elevation. The large shifts occur mainly in

North direction, which is the satellite flight direction. The reason for that should be searched in the future.

6 Conclusions and future work

6.1 Conclusions

In this diploma thesis, a new adjustment method against large Cartosat-1 stereo blocks by using SRTM DSM as the ground control is introduced. This method is used for improving the poor accuracy of raw RPCs parameters which is in the order of hundred meters and avoiding using high accurate ground control points as well. The main part of this thesis is the 1-step large block adjustment and evaluation of the adjusted affine RPC corrections with high accurate check points.

In the following the whole working process was shortly illustrated. First of all, a large Cartosat-1 stereo block including overlapping images was selected. Tie points files were generated after accurate image matching (e.g. SIFT image matching and LSM image matching). Then, along with raw RPC data and SRTM DSM data as the ground control instead of GCPs, a large block adjustment was made. The final outputs were the corrected affine RPC parameters and 3D tie point coordinates. Finally, check points were extracted from aerial images for the purpose of evaluating the adjusted results.

The main dataset used in this thesis is a large Cartosat-1 stereo block included 428 stereo pairs (region in north Italy). This large block covers various kinds of landforms such as mountains, flat areas, cities and Mediterranean so that it is very suitable to test the quality and stability of block adjustment.

By using 1-step adjustment model and high accurate check points derived from aerial images, after the evaluation of the results, following conclusions and future work can be given.

1) After single stereo pair adjustment with DSM as ground control, RMSE decreases with increasing number of tie points. If the number of tie points reaches nearly 10000 or even more, RMSE of all scenes reduce significantly to below 10m or even 5m. What's more, adjusted results derived from LSM tie points are better than results from SIFT tie points.

2) After the 1-step large block adjustment, estimated standard deviations of bias RPC corrections of a single scene improve much after large block adjustment (can reach sub-pixel accuracy) compared to the results after single pair adjustment.

3) In the selected 16 test areas, the evaluation along with check points derived from aerial images is processed. After 1-step large block adjustment horizontal point errors of most scenes are below 16m or even 8m. Even the flat scenes in the middle of the large block obtain relative small horizontal point errors after large block adjustment. However, some scenes of selected test areas at the right hand side still present large RMSE which is even over 56m. In fact, these areas are exactly the east edge of the large block and cover the flat regions and even the sea so that the DSM constraint functions not well in these areas. In addition, there are not enough other stereo pairs which cover mountainous areas nearby.

4) The RMSE of all scenes in horizontal directions (Easting and Northing) and heights are calculated as well. Compared to other results from ISRO and ETH, the 3D RMSE are comparable in easting (<10m) and height (<5m), although still a little worse. Large RMSE (even 60m) usually occurs in the satellite flight direction (Northing). The possible reason is

that the reference data used in this thesis are not so accurate as ISRO and ETH. Instead of accurate GCPs, inaccurate SRTM DSM (grid 90m) is chosen as the only ground control for the large block adjustment.

According to all of the above, 1-step adjustment model can avoid using high accurate GCPs and reach an accuracy which is lower but adequate in Easting and height compared to the situation using GCPs. Thus, if the demand of accuracy is not very strict, or high accurate GCPs are not available, 1-step adjustment model can be an optional replacement.

6.2 Future work

As discussed above, 3D RMSE are relative large due to the inaccurate SRTM data. In order to process a more accurate block adjustment, it is possible to add a few high accurate GCPs in these areas where large RMSE occur. The method to calculate the gradient of reference data should be further improved in the future, too. Then, the large block adjustment should be processed once again in order that smaller RMSE can be obtained.

Appendix A: Quality evaluation

A.1 Methods of quality evaluation

A.1.1 Global test before quality evaluation

A regular adjustment model is expressed as follows (Gauss - Markov - Model):

$$l + v = Ax, \quad \sum_{ll} = \sigma_0^2 Q_{ll} = \sigma_0^2 P^{-1} \qquad \text{involves } n \text{ observations and } u \text{ unknowns} \tag{A.1}$$

$$\hat{x} = (A^T PA)^{-1} A^T Pl \tag{A.2}$$

$$v = A\hat{x} - l \tag{A.3}$$

Where $\hat{x}$ is the optimal estimation of unknown parameter x; A is the design matrix; l is the misclosure; P stands for the weight matrix; Q_{ll} is the cofactor matrix; σ_0^2 is the variance factor; $\sum_{ll}$ is covariance matrix; and v is the vector of residuals.

Normal matrix and cofactor matrix for optimal estimation $\hat{x}$ are given by following equations:

$$N = A^T PA \tag{A.4}$$

$$Q_{xx} = (A^T PA)^{-1} \tag{A.5}$$

Based on the equations above, as another important parameter, cofactor matrix for the corrections is expressed as follows:

$$Q_{vv} = Q_{ll} - AQ_{xx}A^T \tag{A.6}$$

Two other parameters play a very important role in quality evaluation of an adjustment: The sum of squares of corrections $\Omega = v^T Pv$ and the variance vector σ_0^2. The estimated variance vector $\hat{\sigma}_0^2$ can be derived from Ω and the degrees of freedom $f = n - u$:

$$\hat{\sigma}_0^2 = \frac{\Omega}{f} = \frac{v^T Pv}{f} \tag{A.7}$$

With these two vital indicators, a global test for the adjustment models can be performed. A null hypothesis is as follows:

$$H_0: \qquad E(l) = Ax \tag{A.8}$$

The following probability formula plays a vital role for global test:

$$P\left\{\frac{\Omega}{\sigma_0^2}=\frac{v^T P v}{\sigma_0^2}=\frac{f\cdot\hat{\sigma}_0^2}{\sigma_0^2}>\chi^2_{f,1-\alpha}\,\middle|\,H_0\right\}=\alpha \tag{A.9}$$

If Ω/σ_0^2 is larger than the corresponding value $\chi^2_{f,1-\alpha}$ of the χ^2- distribution, then the null hypothesis H_0 with the level of significance $1-\alpha$ has to be rejected. Given an ideal value σ_0^2, global test can be performed. A failure of the global test indicates an incorrect adjustment model (either functional or statistical model). [Niemeier 2008]

A.2.1 Definition of data quality

For adjustment or estimation of parameters there exist two main quality criteria: accuracy criteria and reliability criteria.

When the functional relationship between unknown parameters and measured values is correct and ideal and valid a priori assumptions for standard deviation and correlation of measured values are known, the accuracy of the unknown parameters can be estimated. For a general adjustment model shown in equation (A.1), the cofactor matrix of unknown parameters Q_{xx} (see equation (A.5)) is selected as an indicator of accuracy. Another important factor is variance factor σ_0^2 or optimal estimated variance factor $\hat{\sigma}_0^2$.

In a given adjustment model, reliability relates not only to the possibility of control for observations that involve blunders, but also to the effect on parameters that are caused by this possibility of control. In addition, with the development of reliability theory, reliability is also meaningful for the estimation of impacts on parameters which derive from unobservable measurement uncertainty and errors. All ordinary reliability measures derive from the cofactor of corrections Q_{vv} (see equation (A.6)). Reliability measures are widely used for protecting from effects of blunders and further negative effects, so that they are called internal geodetic criteria as well. [Niemeier 2008]

A.2.2 Accuracy evaluation

In this chapter some criteria for the accuracy evaluation will be introduced.

A.2.2.1 Cofactor matrix and covariance matrix

As demonstrated before, two important factors for accuracy evaluation are cofactor matrix of parameters Q_{xx} and variance factor σ_0^2 (or estimated variance factor $\hat{\sigma}_0^2$).

For example, the cofactor matrix of parameters Q_{xx} for n 2D points can be described by:

$$Q_{xx} = \begin{array}{c} \begin{matrix} x_1 & y_1 & x_2 & y_2 & \cdots & x_n & y_n \end{matrix} \\ \begin{bmatrix} q_{x_1x_1} & q_{x_1y_1} & q_{x_1x_2} & q_{x_1y_2} & \cdots & q_{x_1x_n} & q_{x_1y_n} \\ q_{y_1x_1} & q_{y_1y_1} & q_{y_1x_2} & q_{y_1y_2} & \cdots & q_{y_1x_n} & q_{y_1y_n} \\ q_{x_2x_1} & q_{x_2y_1} & q_{x_2x_2} & q_{x_2y_2} & \cdots & q_{x_2x_n} & q_{x_2y_n} \\ q_{y_2x_1} & q_{y_2y_1} & q_{y_2x_2} & q_{y_2y_2} & \cdots & q_{y_2x_n} & q_{y_2y_n} \\ \vdots & \vdots & \vdots & \vdots & \ddots & \vdots & \vdots \\ q_{x_nx_1} & q_{x_ny_1} & q_{x_nx_2} & q_{x_ny_2} & \cdots & q_{x_nx_n} & q_{x_ny_n} \\ q_{y_nx_1} & q_{y_ny_1} & q_{y_nx_2} & q_{y_ny_2} & \cdots & q_{y_nx_n} & q_{y_ny_n} \end{bmatrix} \end{array} \tag{A.10}$$

In addition, with the help of variance factor σ_0^2, the theoretical covariance matrix Σ_{xx} of the estimated parameter $\hat{x}$ can be given by:

$$\Sigma_{xx} = \sigma_0^2 Q_{xx} \tag{A.11}$$

If the estimated variance factor $\hat{\sigma}_0^2$ is known, the empirical covariance matrix $\overline{\Sigma}_{xx}$ instead of Σ_{xx} is given by:

$$\overline{\Sigma}_{xx} = \hat{\sigma}_0^2 Q_{xx} \tag{A.12}$$

A.2.2.2 Local accuracy criteria

The common criteria for the accuracy evaluation of a network are local accuracy criteria. Local accuracy criteria only utilize small or even smallest sub-matrix of Q_{xx}.

For individual unknown parameter x_i, a common criterion is the estimation of standard deviation σ_{x_i} (or $\hat{\sigma}_{x_i}$). As shown by following equations:

$$\sigma_{x_i} = \sigma_0 \sqrt{q_{x_ix_i}} \tag{A.13}$$

$$\hat{\sigma}_{x_i} = \hat{\sigma}_0 \sqrt{q_{x_ix_i}} \tag{A.14}$$

With a given level of significance $1-\alpha$, it is able to get the confidence intervals of individual unknown as follows:

$$P(\hat{x}_i - y_{1-\alpha/2} \cdot \sigma_{x_i} \le \tilde{x}_i \le \hat{x}_i + y_{1-\alpha/2} \cdot \sigma_{x_i}) = 1-\alpha \tag{A.15}$$

$$P(\hat{x}_i - t_{f,1-\alpha/2} \cdot \hat{\sigma}_{x_i} \le \tilde{x}_i \le \hat{x}_i + t_{f,1-\alpha/2} \cdot \hat{\sigma}_{x_i}) = 1-\alpha \tag{A.16}$$

Where $\hat{x}_i$ stands for the estimation of individual unknown parameter; $y_{1-\alpha/2}$ is the quantile of normal distribution and $t_{f,1-\alpha/2}$ is the quantile of t-distribution (with f degrees of freedom) respectively.

If the accuracy interval of a point in a network is required, Helmert error ellipses and confidence ellipses can be computed. There are two main catalogs: one is for σ_0^2 and the other is for $\hat{\sigma}_0^2$.

According to equation (A.10), a common cofactor sub-matrix for a 2D point (x, y) in network can be described by:

$$Q = \begin{bmatrix} q_{xx} & q_{xy} \\ q_{yx} & q_{yy} \end{bmatrix} \tag{A.17}$$

With known σ_0^2, thereby, the major semi-axis A_F, minor semi-axis B_F and angle of direction θ_F, which are the three main parameters of a Helmert error ellipse are given as follows:

$$\begin{aligned} A_F^2 &= \frac{1}{2}\sigma_0^2(q_{xx} + q_{yy} + \omega) \\ B_F^2 &= \frac{1}{2}\sigma_0^2(q_{xx} + q_{yy} - \omega) \\ \tan 2\theta_F &= 2\frac{q_{xy}}{q_{xx} - q_{yy}} \end{aligned} \tag{A.18}$$

Where

$$\omega^2 = (q_{xx} - q_{yy})^2 + 4q_{xy}^2$$

Another approach for Helmert error ellipse uses spectral decomposition of Q, as follows:

$$Q = SDS^T = [s_1 \; s_2]\begin{bmatrix} \lambda_1 & 0 \\ 0 & \lambda_2 \end{bmatrix}\begin{bmatrix} s_1^T \\ s_2^T \end{bmatrix} \tag{A.19}$$

Where λ_1 and λ_2 stand for eigenvalues along the main diagonal; s_1 and s_2 stand for eigenvectors.

Thereby, the three parameters can be given also by:

$$\begin{aligned} A_F^2 &= \sigma_0^2\lambda_1 \\ B_F^2 &= \sigma_0^2\lambda_2 \\ \tan\theta_F &= \frac{s_{1x}}{s_{1y}} \end{aligned} \tag{A.20}$$

Where s_{1x} and s_{1y} stand for $x-$ and $y-$ components of eigenvector s_1 and $\lambda_1 > \lambda_2$.

Further, a $(1-\alpha)$-quantile of χ^2-distribution with 2 degrees of freedom is added for the purpose of obtaining 3 confidence ellipse parameters (A_K, B_K, θ_K). As follows:

$$
\begin{aligned}
A_K^2 &= A_F^2 \cdot \chi_{2,1-\alpha}^2 = \sigma_0^2 \cdot \lambda_1 \cdot \chi_{2,1-\alpha}^2 \\
B_K^2 &= B_F^2 \cdot \chi_{2,1-\alpha}^2 = \sigma_0^2 \cdot \lambda_2 \cdot \chi_{2,1-\alpha}^2 \\
\theta_K &= \theta_F
\end{aligned}
\tag{A.21}
$$

However, the practical accuracy evaluation $\hat{\sigma}_0^2$ is used. In a similar way, the 3 parameters of Helmert error ellipse are given by:

$$
\begin{aligned}
\overline{A}_F^2 &= \frac{1}{2}\hat{\sigma}_0^2(q_{xx} + q_{yy} + \omega) \\
\overline{B}_F^2 &= \frac{1}{2}\hat{\sigma}_0^2(q_{xx} + q_{yy} - \omega) \\
\tan 2\theta_F &= 2\frac{q_{xy}}{q_{xx} - q_{yy}}
\end{aligned}
\tag{A.22}
$$

Where

$$
\omega^2 = (q_{xx} - q_{yy})^2 + 4q_{xy}^2 \tag{A.23}
$$

For generating a confidence ellipse, a $(1-\alpha)$-quantile of F-distribution $F_{2,f,1-\alpha}$ is added. Here f identifies excessive observations. Three parameters $\overline{A}_K, \overline{B}_K, \theta_K$ are described as:

$$
\begin{aligned}
\overline{A}_K^2 &= 2 \cdot \overline{A}_F^2 \cdot F_{2,f,1-\alpha}^2 = 2 \cdot \hat{\sigma}_0^2 \cdot \lambda_1 \cdot F_{2,f,1-\alpha}^2 \\
\overline{B}_K^2 &= 2 \cdot \overline{B}_F^2 \cdot F_{2,f,1-\alpha}^2 = 2 \cdot \hat{\sigma}_0^2 \cdot \lambda_2 \cdot F_{2,f,1-\alpha}^2 \\
\theta_K &= \theta_F
\end{aligned}
\tag{A.24}
$$

An often applied criterion for point accuracy is so-called point error. There are two main point error scales:

Helmert (mean) point error:

$$
s_P^H = \sqrt{s_x^2 + s_y^2} = \hat{\sigma}_0\sqrt{\lambda_1 + \lambda_2} \tag{A.25}
$$

Werkmeister point error:

$$
s_P^W = \sqrt{s_x^2 \cdot s_y^2 + s_{xy}^2} = \hat{\sigma}_0\sqrt{\lambda_1 \cdot \lambda_2} \tag{A.26}
$$

Helmert point error only considers the trace of cofactor matrix and covariance matrix, so it is also called trace criterion; Werkmeister point error takes the volume of error ellipse into account so that it is also called volume criterion.

A.2.2.3 Global accuracy criteria

Compare with local accuracy criteria, global accuracy criteria relate to evaluation of points precision (for this thesis precision of RPC corrections is also included) for the whole network and network optimization respectively. Because of this, the whole theoretical covariance matrix Σ_{xx} or the whole empirical covariance matrix $\overline{\Sigma}_{xx}$ instead of sub-matrix is the best

indicator, which represents the accuracy of all the points in the network. Here only give the situation with known σ_0^2 and when it is substituted by $\hat{\sigma}_0^2$, the process is similar.

Generally, a spectral decomposition for Σ_{xx} (or $\overline{\Sigma}_{xx}$) is necessary, too. As follows:

$$\Sigma_{xx} = SDS^T = [s_1\ s_2 \cdots s_u] \begin{bmatrix} \lambda_1 & & 0 \\ & \lambda_2 & \\ & & \ddots \\ 0 & & \lambda_u \end{bmatrix} \begin{bmatrix} s_1^T \\ s_2^T \\ \vdots \\ s_u^T \end{bmatrix} \tag{A.27}$$

Two minimal requirements help guarantee the accuracy of network. As follows:

$$\det(\Sigma_{xx}) = \lambda_1 \cdot \lambda_2 \cdot \ldots \cdot \lambda_u = \prod_{i=1}^{u} \lambda_i \to \min \tag{A.28}$$

$$trace(\Sigma_{xx}) = \lambda_1 + \lambda_2 + \ldots + \lambda_u = \sum_{i=1}^{u} \lambda_i \to \min \tag{A.29}$$

Here $\det(\Sigma_{xx})$ is called u-dimensional Werkmeister point error, while $trace(\Sigma_{xx})$ is called u-dimensional Helmert (mean) point error.

The problem is: although for u- dimensional situation it is still possible to calculate all the semi-axes, plot such a so-called u-dimensional (u>3) confidence ellipse is of course impossible.

$$A_i^2 = \sigma_0^2 \lambda_i \chi_{u,1-\alpha}^2 \tag{A.30}$$

Further the so-called mean coordinate accuracy is given by:

$$\hat{\sigma}_x^2 = trace(\Sigma_{xx}) \cdot \frac{1}{u} \tag{A.31}$$

It is a vital precision specification for the whole network optimization.

Another import optimization criterion is the ratio of largest to smallest eigenvalue $\lambda_{\max} / \lambda_{\min}$. The requirement is that $\lambda_{\max}$ and $\lambda_{\min}$ should be nearly the same, which leads to a homogeneous or even isotropic structure of confidence ellipses. A homogenous structure means all confidence ellipses have the same form; while an isotropic structure represents the same accuracy in all directions. Two equivalent formulations are given by:

$$\frac{\lambda_{\max}}{\lambda_{\min}} \to 1 \tag{A.32}$$

$$\lambda_{\max} - \lambda_{\min} \to \min \tag{A.33}$$

In order to find the weak positions within the network, a principal component analysis is performed. The simple calculation of principal components bases on the eigenvalue λ_i and its belonging eigenvector s_i. For example, the 1st principal component, which is the most important component, is given by following formula:

$$p_1 = s_1 \cdot \sqrt{\lambda_1} \qquad with\ \lambda_1 = \lambda_{\max} \tag{A.34}$$

This means 1st principal component is determined by the largest eigenvalue and its belonging eigenvector. Similarly 2nd principal component relate to the second largest eigenvalue etc.

The largest eigenvalue λ_1 and occupies a large percent of total variance $\sum \lambda_i = trace(\Sigma_{xx})$. Thereby, the corresponding eigenvector s_1 of 1st principal component is also called "essential eigenvector", since it reflects the direction, which is determined most imprecise (In other words, the direction strongly influenced by random errors).

A.2.3 Reliability evaluation

As introduced before, the concept of reliability for network analysis is composed of two catalogs: interior reliability and exterior reliability. Interior reliability describes the ability of a network to find blunders which are as small as possible. Exterior reliability has the task to evaluate the effect caused by a just undetectable model error and then tell the users how much it will influence the coordinates of network points.

Choose the same general adjustment model like equation (A.1) with the resumption that cofactor matrix Q_{ll} and weight matrix P are both identify matrix.

To ensure a reliable estimation of parameters, enough redundant observations are necessary. In this way, the possible inaccurate observations can be detected and eliminated. As described before, the cofactor matrix of corrections Q_{vv} plays the most important role in reliability evaluation and it can be given with the help of well-known Hat-matrix H (also called projection matrix), as follows:

$$H = A(A^T A)^{-1} A^T \tag{A.35}$$

$$Q_{vv} = Q_{ll} - A(A^T A)^{-1} A^T = I - H \tag{A.36}$$

Then it is possible to calculate the trace of Q_{vv}, which relates to a degrees of freeedom $r = n - u$:

$$trace(Q_{vv}) = trace(I - H) = \sum_{i=1}^{n} (1 - h_{ii}) = n - \sum_{i=1}^{n} h_{ii} = n - u = r \tag{A.37}$$

According to the reliability theory, redundancy proportions r_i derived from the i-te diagonal element of Q_{vv} play a decisive role in reliability evaluation. As follows:

$$r_i = (q_{vv})_{ii} = 1 - h_{ii} \tag{A.38}$$

With the purpose of judging whether the redundancy of a point is good or not, a new concept of mean redundancy proportions should be given as follows:

$$\overline{r_i} = 1 - \frac{u}{n} = 1 - \overline{h_{ii}} \tag{A.39}$$

If mean redundancy proportions r_i are larger than mean redundancy proportions $\overline{r_i}$, these individual observations are called “well-controlled“ observations; On the other hand, if r_i are significant smaller than $\overline{r_i}$ or even nearly zero, they will be called “bad controlled“ observations.

It is important to point out that the observations which have too small redundancy proportions r_i are called Hebel observations and the possible exiting blunders in these observations are difficult to detect. Therefore, in the process of network optimization, the redundancy proportions smaller than 0.2 are commonly not allowed.

Appendix B: Results of test area 1 and 2

Image No.	Grid cell width/height (unit: pixel)				
	50	100	500	1000	2000
187	11163	7116	559	143	36
21	8821	5311	462	126	35
230	13792	8133	550	140	36
48	5761	2869	418	132	36
63	21365	8341	457	121	33

Table B.1: The number of SIFT tie points for test area 1

Image No.	Grid cell width/height (unit: pixel)						
	no grid	50	100	200	500	1000	2000
187	252202	41157	12875	3428	561	143	36
21	158522	29467	9576	2669	461	125	34
230	321328	43768	12798	3337	548	139	36
48	96427	14862	5867	2080	449	121	33
63	232190	30589	9102	2490	431	116	31

Table B.2: The number of LSM tie points for test area 1

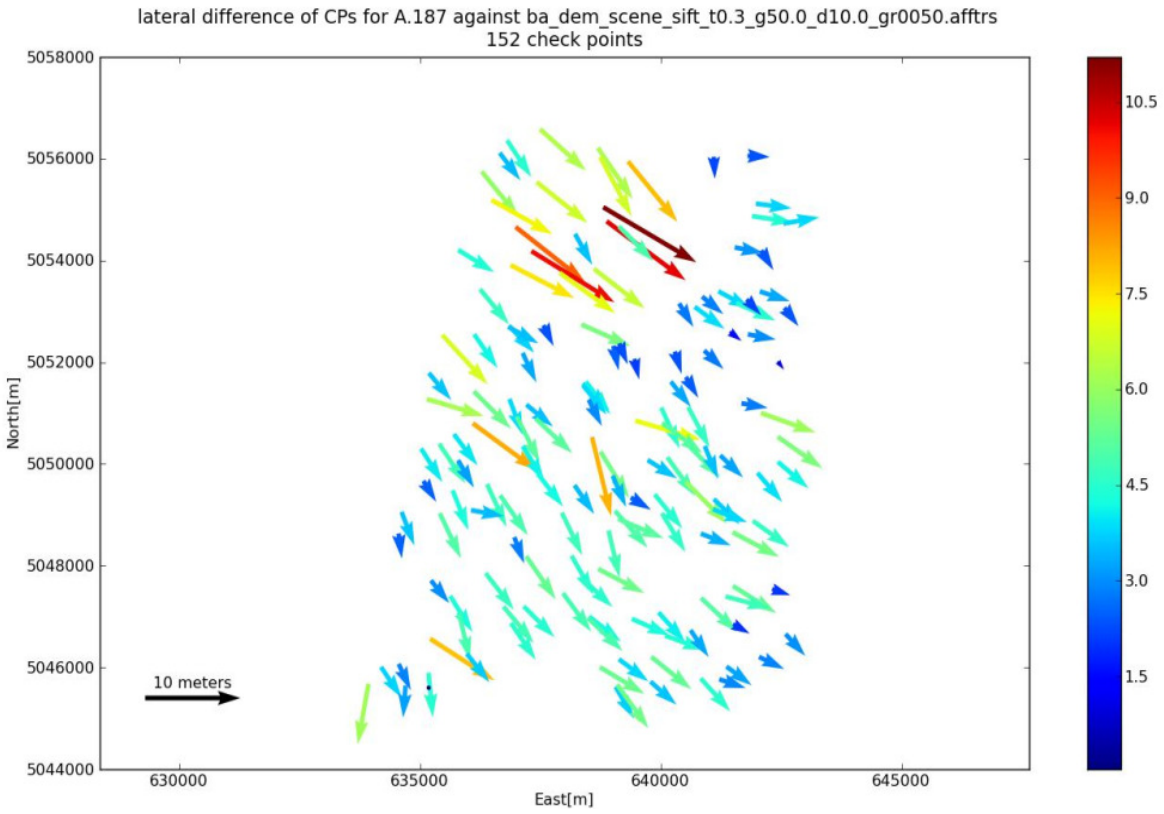

Figure B.1: Horizontal errors of aerial image CPs for stereo pair 187 (11163 SIFT tie points)

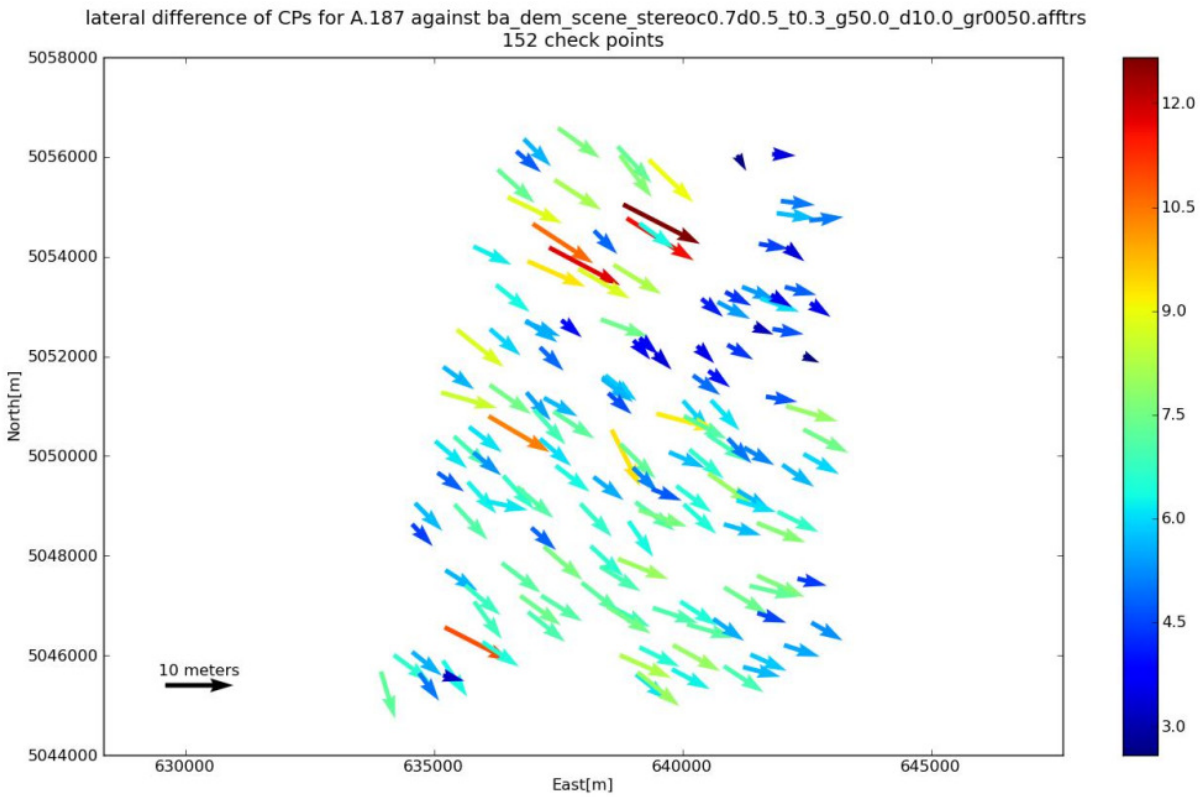

Figure B.2: Horizontal errors of aerial image CPs for stereo pair 187 (41157 LSM tie points)

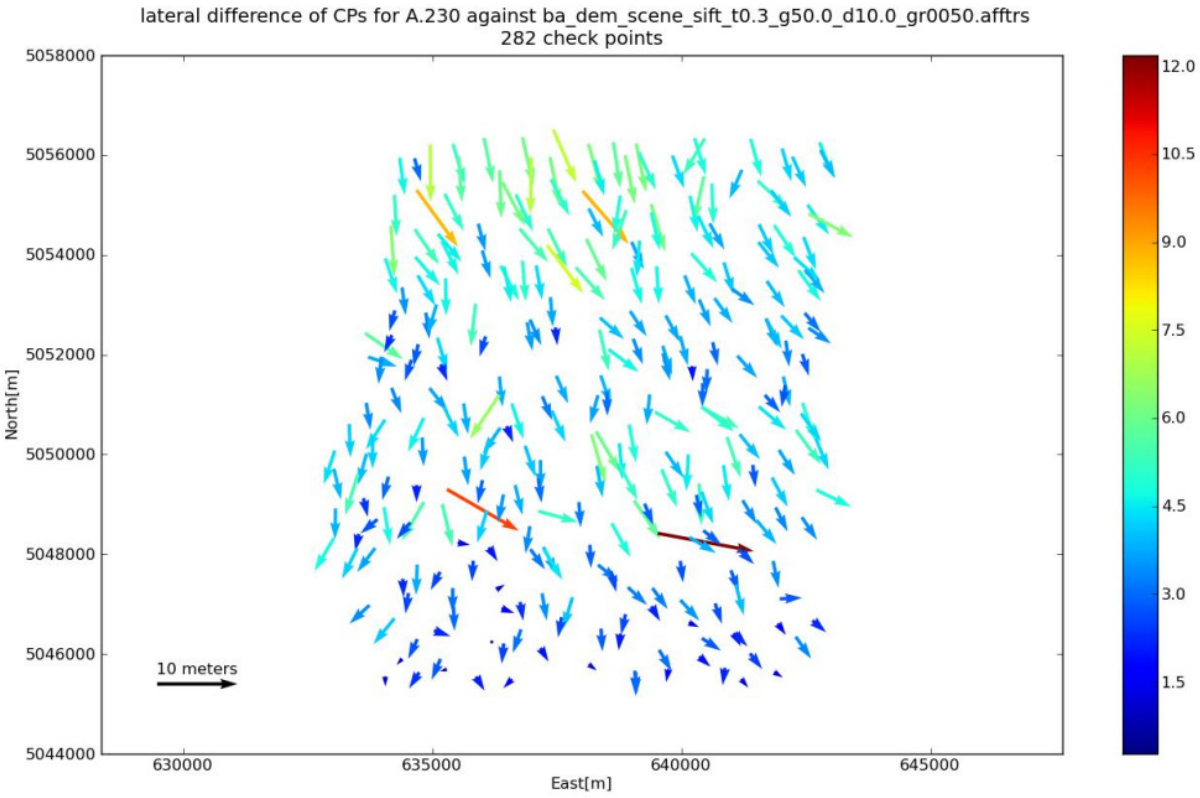

Figure B.3: Horizontal errors of aerial image CPs for stereo pair 230 (13792 SIFT tie points)

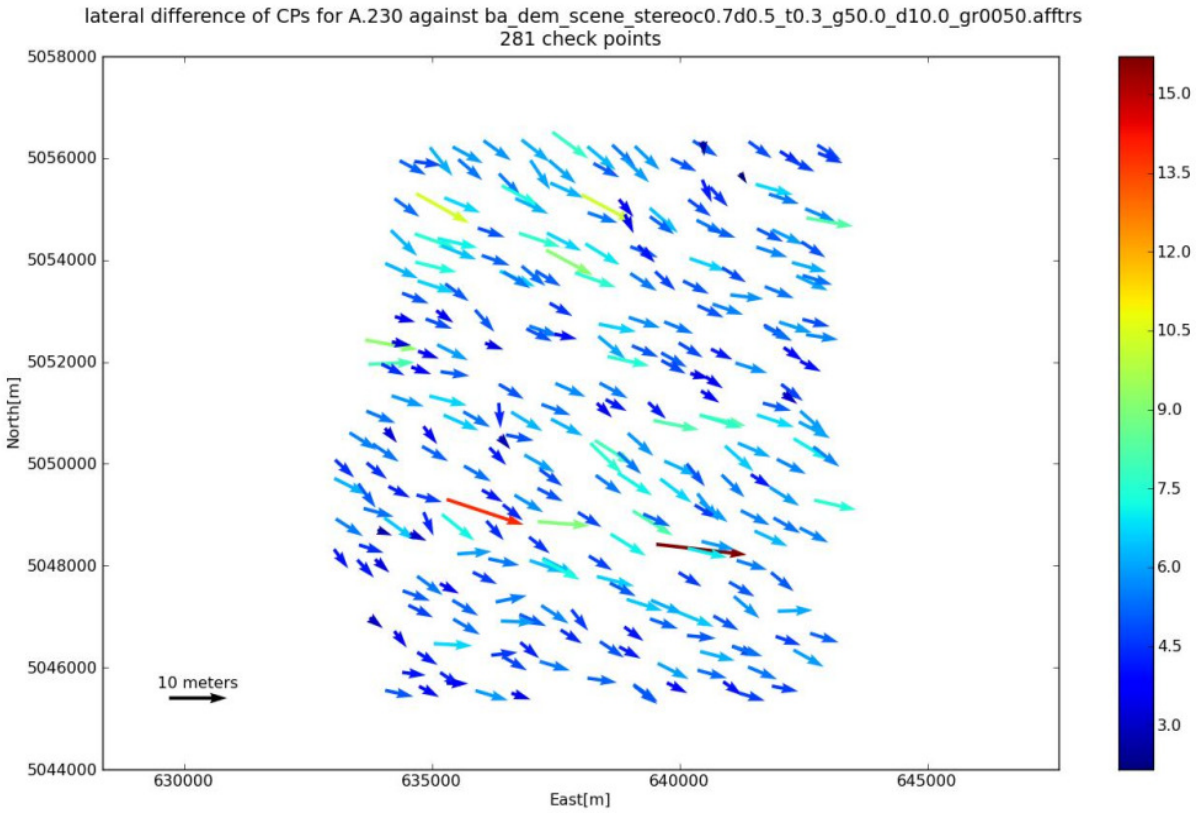

Figure B.4: Horizontal errors of aerial image CPs for stereo pair 230 (43768 LSM tie points)

Image No.	Grid cell width/height (unit: pixel)				
	50	100	500	1000	2000
252	5508	2893	443	141	36
259	6502	4378	525	144	36
296	4989	3586	486	141	36

Table B.3: The number of SIFT tie points for test area 2

Image No.	Grid cell width/height (unit: pixel)						
	no grid	50	100	200	500	1000	2000
252	243551	28912	9560	2822	514	134	35
259	192791	32529	10460	3035	548	143	36
296	-	26414	8894	2657	495	134	35

Table B.4: The number of LSM tie points for test area 2

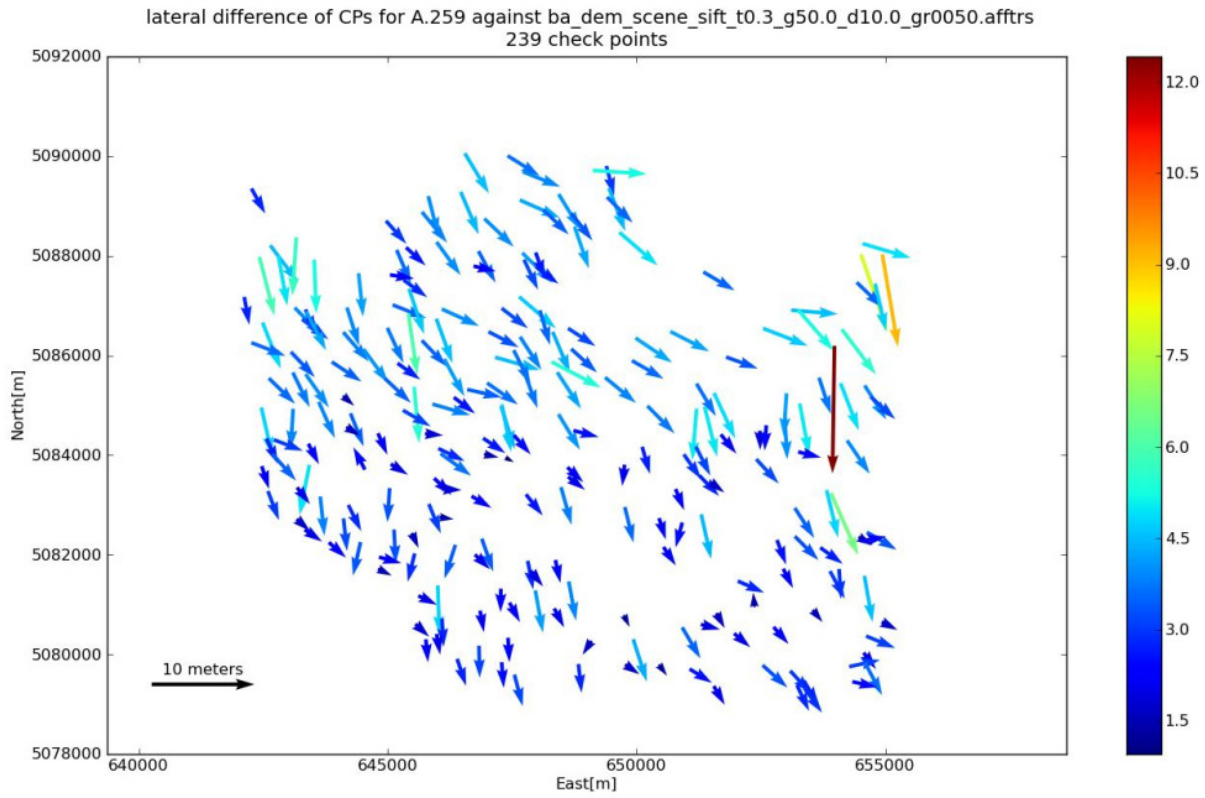

Figure B.5: Horizontal errors of aerial image CPs for stereo pair 259 (6502 SIFT tie points)

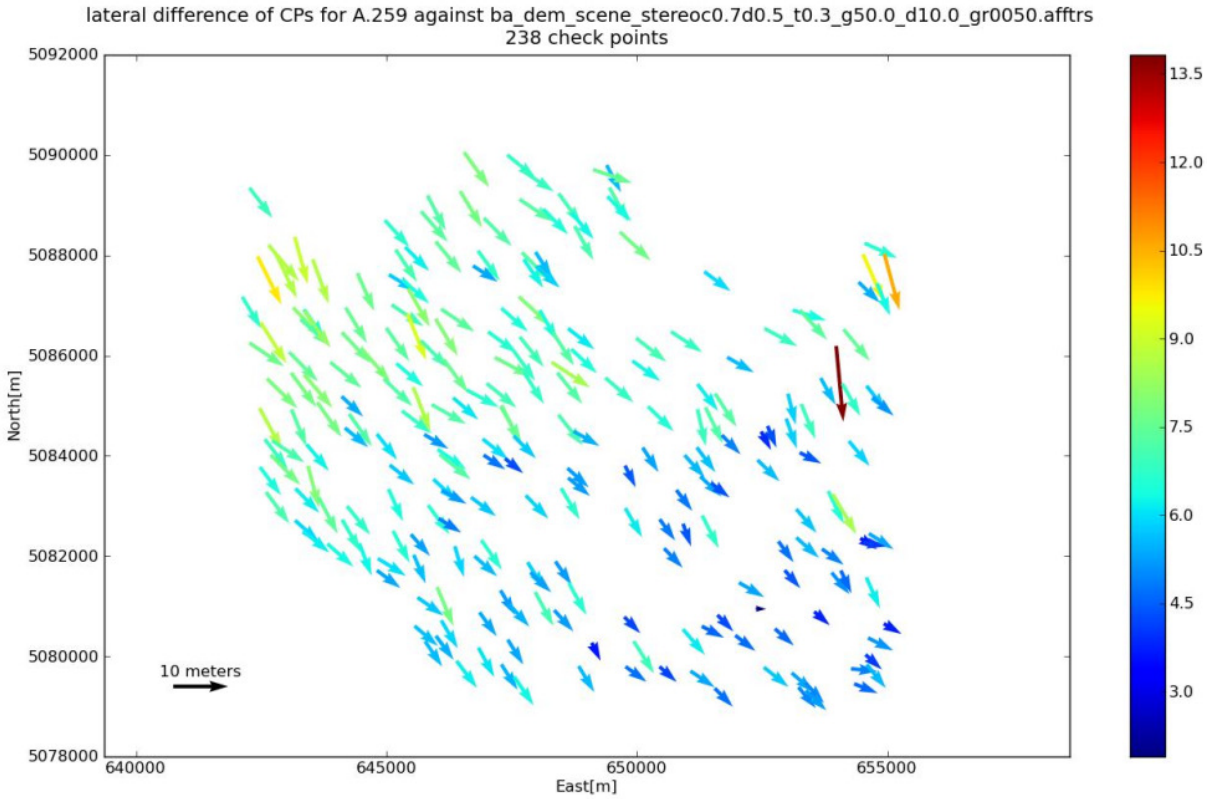

Figure B.6: Horizontal errors of aerial image CPs for stereo pair 259 (32529 LSM tie points)

Acknowledgment

First of all, I would like to thank everyone who helps me finish this diploma thesis.

I must thank for the supervision of Dr. -Ing. Pablo d'Angelo of remote sensing technology institute, department photogrammetry and image analysis. During this time, you taught me a lot about how to finish this thesis well. What's more, you spent much precious time to read and correct my thesis.

I also want to say thank you to Dr. -Ing. Michael Cramer of the institute for photogrammetry. Thank you for your supervision. Additionally, after learning the courses "Image acquisition and monoplotting" and "Aerotriangulation and stereoplotting" you've given in the university Stuttgart, I've gotten the motivation to do a final thesis with this topic.

I also want to thank every colleague of department photogrammetry and image analysis, especially Dr. Peter Reinartz, who gave me a chance to finish my final thesis in DLR, remote sensing technology institute, department photogrammetry and image analysis.

Finally, I would like to thank my family for their support.

Bibliography

Ahmed, N. et al. (2007): “Extraction and validation of Cartosat-1 DEM”, Photonirvachak, Journal of the Indian Society of Remote Sensing, Vol. 35, No.2, 2007.

Böhm, J. (2007): “Nahbereichsphotogrammetrie”. Vorlesungsskript im WS 07/08, Institut für Photogrammetrie, Universität Stuttgart.

Chen, Liang-Chien., Teo, Tee-Ann. and Lo, Chao-Yuan (2008): “Elevation-controlled block adjustment for weakly convergent satellite images”, Commission I, WG I/5, The International Archives of the Photogrammetry, Remote Sensing and Spatial Information Sciences. Vol. XXXVII. Part B1. Beijing 2008. Digital available at: http://www.isprs.org/proceedings/XXXVII/congress/1_pdf/131.pdf (last visited on 18.03.2011)

Cramer, M. (2010): “Bildaufzeichnung & Monoplotting”. Vorlesungsskript im WS 10/11, Institut für Photogrammetrie, Universität Stuttgart.

Crespi, M., Barbato, F., De Vendictis, L., Iannucci, G., Poli, D., Volpe, F., and Wang, X. (2006): “Cartosat-1 stereo imagery: potentialities about orientation, DSM extraction and orthorectification”, Commision I, WG I/5, Proceedings of ISPRS Commission IV Symposium, September 27-30, 2006, Goa, India. Digital available at: http://www.ipi.uni-hannover.de/fileadmin/institut/pdf/Crespi_barbarto_etal.pdf (last visited on 18.03.2011)

Dabrowski, R., Fedorowicz-Jackowski, W., Kedzierski, M., Walczykowski, P. and Zych, J. (2008): “Cartosat-1: Orientation, DEM and orthorectification quality assessment”, Commision I, SS-11, The International Archives of the Photogrammetry, Remote Sensing and Spatial Information Sciences. Vol. XXXVII. Part B1. Beijing 2008. Digital available at: http://www.isprs.org/proceedings/XXXVII/congress/1_pdf/222.pdf (last visited on 18.03.2011)

D’Angelo, P., Lehner, M., Krauss, T., Hoja, D. and Reinartz, P. (2008): “Towards automated DEM generation from high resolution stereo satellite images”, Commission IV, WG IV/9, The International Archives of the Photogrammetry, Remote Sensing and Spatial Information Sciences, Vol. XXXVII. Part B4, Beijing. Digital available at: http://www.isprs.org/proceedings/XXXVII/congress/4_pdf/199.pdf (last visited on 18.03.2011)

D’Angelo, P., Schwind, P., Krauss, T., Barner, F. and Reinartz, P. (2009): “Automated DSM based georeferencing of Cartosat-1 stereo scenes”, ISPRS Hannover Workshop 2009, High-Resolution Earth Imaging for Geospatial Information. Digital available at: http://www.ipi.uni-hannover.de/fileadmin/institut/pdf/isprs-Hannover2009/d_Angelo-165.pdf (last visited on 18.03.2011)

D’Angelo, P., Uttenthaler, A., Carl, S., Barner, F. and Reinartz, P. (2010): “Automated generation of high quality DSM based on IRS-P5 Cartosat-1 stereo data”. Digital available at: http://www.euromap.de/pdf/040_D4angelo.pdf (last visited on 18.03.2011)

Giannone, F. (2007): “A rigorous model for high resolution satellite imagery orientation”, University of Rome “La Sapienza”, Falculty of Engineering, Department of “Idraulica e Trasporti e Strade”, “Geodesia e Geomatica” Area. Digital available at: http://www.dirap.unipa.it/autec/old/premio%202007/Francesca%20Giannone.pdf (last visited on 18.03.2011)

Grodecki, J. and Dial, G. (2003): “Block adjustment of high-resolution satellite images described by rational polynomials”, Photogrammetric Engineering & Remote Sensing, Vol.69, No.1, January 2003, pp. 59-68. Digital available at: http://www.asprs.org/publications/pers/2003journal/january/2003_jan_59-68.pdf (last visited on 18.03.2011)

Hu, Y. and Tao, C. V. (2001): “Updating solutions of the rational function model using additional control points for enhanced photogrammetric processing”, Proceedings of Joint International Workshop on High Resolution Mapping from space, 19-21 September, Hannover, Germany, pp. 234-251. Digital available at: http://www.geoict.yorku.ca/past-publications/test-page/papers/past-researchers-papers/Updating%20SOlutions.pdf (last visited on 18.03.2011)

Kocaman, S., Wolff, K. and Baltsavias, E. (2008): “Geometric validation of Cartosat-1 imagery”, Proc. 21th ISPRS Congress, 3-11 July, 2008 Beijing. Digital available at: http://www.photogrammetry.ethz.ch/general/persons/AG_pub/08_Kocaman_Wolff_Beijing_validation.pdf (last visited on 18.03.2011)

Lehner, M., D’Angelo, P., Müller, R. and Reinartz, P. (2008): “Stereo evaluation of Cartosat-1 data - summary of DLR results during Cartosat-1 scientific assessment program”, Commission I, SS-11, The International Archives of the Photogrammetry, Remote Sensing and Spatial Information Sciences, Vol. XXXVII. Part B1, Beijing. Digital available at: http://www.isprs.org/proceedings/XXXVII/congress/1_pdf/220.pdf (last visited on 18.03.2011)

Lehner, M., Müller, R. and Reinartz, P. (2004): “DSM and orthoimages from QuickBird and IKONOS data using rational polynomial functions”, Commission I, WG I/5. Proceedings of “High Resolution Earth Imaging for Geospatial Information”, May 17-20, Hannover, Germany. Digital available at: http://www.ipi.uni-hannover.de/fileadmin/institut/pdf/062-lehner.pdf (last visited on 18.03.2011)

Lehner, M., Müller, R. and Reinartz, P. (2006): “Stereo evaluation of Cartosat-1 data on test site 5 – First DLR results”, Cartosat-1 Scientific Assessment Program - Commission IV. Digital available at: http://elib.dlr.de/46206/1/CSAPpaperLehner.doc (last visited on 18.03.2011)

Lehner, M., Müller, R., Reinartz, P. and Schröder, M. (2007): “Stereo evaluation of Cartosat-1 data for French and Catalonian test sites”, Cartosat-1 Scientific Assessment Program – Commission IV/WG 9. Digital available at: http://www.ipi.uni-hannover.de/fileadmin/institut/pdf/Lehner_mueller_reinartz_schroeder.pdf (last visited on 18.03.2011)

Liping, Z., Fengde, L., Wei, W. and Jian, L. (2008): “Preliminary research on position accuracy of Cartosat-1”, Commission I, SS-11, the International Archives of the Photogrammetry, Remote Sensing and Spatial Information Sciences. Vol. XXXVII. Part B1. Beijing 2008. Digital available at: http://www.isprs.org/proceedings/XXXVII/congress/1_pdf/226.pdf (last visited on 18.03.2011)

Lutes, J. (2006): “First impressions of Cartosat-1”, JACIE Workshop March 14-16, 2006. Digital available at: http://calval.cr.usgs.gov/JACIE_files/JACIE06/Files/23Lutes.pdf (last visited on 18.03.2011)

Lutes, J. (2006): “Photogrammetric processing of Cartosat-1 stereo imagery”. Digital available at: http://www.eotec.com/images/Lutes_Cartosat_JACIE2006.pdf (last visited on 18.03.2011)

Niemeier, W. (2008): “Ausgleichungsrechnung – Statistische Auswertemethoden”, 2. Auflage, de Gruyter.

Puckorius, J. T. (2008): “Indian Remote Sensing Satellites – Current & Future Missions”. Digital available at: http://www.eotec.com/images/IRS_-_Current_and_Future_-_Web.pdf (last visited on 18.03.2011)

Singh, G. (2008): “Improved Geometric Modeling of Spaceborne Pushbroom Imagery Using Modified Rational Polynomial Coefficients and the impact on DSM Generation”, Enschede, Dehradun, ITC, Indian Institute of Remote Sensing (IIRS), 2008. Digital available at: http://www.itc.nl/library/papers_2008/msc/gfm/gurpreetsingh.pdf (last visited on 18.03.2011)

Singh, S. K. et al. (2008): “Rational polynomial modelling for Cartosat-1 data”, Commission, WG I/5, The International Archives of the Photogrammetry, Remote Sensing and Spatial Information Sciences. Vol. XXXVII. Part B1. Beijing 2008. Digital available at: http://www.isprs.org/proceedings/XXXVII/congress/1_pdf/152.pdf (last visited on 18.03.2011)

Srivastava, P.K. et al. (2007): “Recent advances in Cartosat-1 data processing”, ISPRS Hannover Workshop 2007. Digital available at: http://www.ipi.uni-hannover.de/fileadmin/institut/pdf/Srivastava_etal.pdf (last visited on 18.03.2011)

Titarov, P. S. (2007): “Cartosat-1 stereo orthokit data evaluation”. Digital available at: http://www.ipi.uni-hannover.de/fileadmin/institut/pdf/Titarov.pdf (last visited on 18.03.2011)

Yilmaz, A., Ozerbil, O. T., Eker, O., Erdogan, M. and Maras, E.E. (2008): “Investigation of 3D geopositioning and DEM accuracy of Cartosat-1 stereo imagery”, Commission I, WG I/5, the International Archives of the Photogrammetry, Remote Sensing and Spatial Information Sciences. Vol. XXXVII. Part B1. Beijing 2008. Digital available at: http://www.isprs.org/proceedings/XXXVII/congress/1_pdf/138.pdf (last visited on 18.03.2011)

List of tables

List of figures